THE EFFECT OF TOPOGRAPHY-INDUCED MECHANOTRANSDUCTION ON EXPRESSION LEVELS OF FOCAL ADHESION-RELATED GENES IN NEURO-2A CELLS

A THESIS SUBMITTED TO
THE GRADUATE SCHOOL OF NATURAL AND APPLIED SCIENCES
OF
MIDDLE EAST TECHNICAL UNIVERSITY

BY

ŞEYDA CULFA

IN PARTIAL FULFILLMENT OF THE REQUIREMENTS
FOR
THE DEGREE OF MASTER OF SCIENCE
IN
BIOCHEMISTRY

AUGUST 2022

Approval of the thesis:

THE EFFECT OF TOPOGRAPHY-INDUCED MECHANOTRANSDUCTION ON EXPRESSION LEVELS OF FOCAL ADHESION-RELATED GENES IN NEURO-2A CELLS

submitted by **ŞEYDA CULFA** in partial fulfillment of the requirements for the degree of **Master of Science** in **Biochemistry, Middle East Technical University** by,

Prof. Dr. Halil Kalıpçılar
Dean, Graduate School of **Natural and Applied Sciences**

Assoc. Prof. Dr. Özgül Persil Çetinkol
Head of the Department, **Biochemistry**

Assoc. Prof. Dr. Çağdaş Devrim Son
Supervisor, **Biochemistry, METU**

Assoc. Prof. Dr. Alpan Bek
Co-Supervisor, **Physics, METU**

Examining Committee Members:

Assoc. Prof. Dr. Tülin Yanık
Biochemistry, METU

Assoc. Prof. Dr. Çağdaş Devrim Son
Biochemistry, METU

Assoc. Prof. Dr. Alpan Bek
Physics, METU

Assist. Prof. Dr. Ihor Pavlov
Physics, METU

Assist. Prof. Dr. Gamze Bora
Medical Biology, Hacettepe University

Date: 29.08.2022

I hereby declare that all information in this document has been obtained and presented in accordance with academic rules and ethical conduct. I also declare that, as required by these rules and conduct, I have fully cited and referenced all material and results that are not original to this work.

Name Last name : Şeyda Culfa

Signature :

ABSTRACT

THE EFFECT OF TOPOGRAPHY-INDUCED MECHANOTRANSDUCTION ON EXPRESSION LEVELS OF FOCAL ADHESION-RELATED GENES IN NEURO-2A CELLS

Culfa, Şeyda
Master of Science, Biochemistry
Supervisor: Assoc. Prof. Dr. Çağdaş Devrim Son
Co-Supervisor: Assoc. Prof. Dr. Alpan Bek

August 2022, 141 pages

Cells' interaction with their environment and how their responses to different mechanical cues are regulated have attracted attention for decades. These mechanical cues vary from topography to substrate stiffness. Knowing how topography-induced cell responses are regulated might give useful information about cell behaviors in health and disease states. This knowledge can be utilized to manipulate cell behaviors for different purposes. Topography-dependent cell behaviors rely on various parameters such as cell type, substrate material type, and topographical features. The Neuro-2A (N2a) cell line was used in the present study because of its availability and versatility. Two different silicon substrate types, polished or laser-fabricated, were used. Fabrication of Silicon was carried out by ultrafast infrared pulsed laser to create micro- and/or nano-topographies. Scanning Electron Microscopy (SEM) and Atomic Force Microscopy were used to characterize substrates. Cells were grown on a control substrate (plastic dish - 35 mm x 10 mm TC- treated plastic cell culture dish which is made up of polystyrene), polished silicon, and laser-fabricated substrates with different topographies for 24 hours to evaluate cell behaviors. After 24 hours, cell morphological responses were studied with confocal microscopy and SEM. Also, after 24 hours, focal-adhesion-related gene expression levels were measured with qRT-PCR and protein expression levels with Western Blot analysis. On all topographies, there was a significant increase in the majority of focal adhesion-related gene expression levels compared to control cells grown on the plastic dish. It was also observed that actin fibers were aligned with the direction of the lines of topographies, especially when two different topographies were combined on a single substrate. When the cells are differentiated, this directional alignment of actin fibers becomes more prominent.

In conclusion, substrate topography did not affect only the cells' morphological behaviors but also had a critical role in the changes at the gene and protein levels. Also, it was found that substrate topography has different effects on different cell behaviors associated with spreading and adhesion. Therefore, manipulating these behaviors at the gene and protein levels might be a promising approach for studying cell behaviors in health and disease states in future studies.

Keywords: Neuro-2A cells, focal adhesion-related genes, surface topography, silicon, imaging.

ÖZ

TOPOGRAFYAYA BAĞLI MEKANOTRANSDÜKSIYON'UN NÖRO-2A HÜCRELERİNDE FOKAL ADEZYONLA İLİŞKİLİ GENLERİN EKSPRESYON DÜZEYLERİ ÜZERİNE ETKİSİ

Culfa, Şeyda
Yüksek Lisans, Biyokimya
Tez Yöneticisi: Doç. Dr. Çağdaş Devrim Son
Ortak Tez Yöneticisi: Doç. Dr. Alpan Bek

Ağustos 2022, 141 sayfa

Hücrelerin çevreleriyle etkileşimi ve farklı mekanik sinyallere tepkilerinin nasıl düzenlendiği onlarca yıldır dikkat çekmiştir. Bu mekanik sinyaller, topografyadan matris sertliğine kadar çeşitli tiplere sahiptir. Topografinin neden olduğu hücre tepkilerinin nasıl düzenlendiği bilgisi, sağlık ve hastalık durumlarında hücre davranışları hakkında faydalı bilgiler verebilir ve bu bilgi, farklı amaçlar için hücre davranışlarının manipülasyonu için kullanılabilir. Topografyaya bağlı hücre davranışları, hücre tipi, substrat malzeme tipi ve topografik özellikler gibi farklı parametrelere dayanır. Bu çalışmada, kullanılabilirliği ve çok yönlülüğü nedeniyle Neuro-2A hücre hattı hücre modeli olarak kullanılmıştır. Cilalı veya lazerle işlenmiş olan iki farklı silikon substrat tipi kullanılmıştır. Silikon işlemesi, mikro ve/veya nanotopografiler oluşturmak için ultra hızlı kızılötesi darbeli lazer tarafından gerçekleştirilmiştir. Substratların karakterizasyonu için Taramalı Elektron Mikroskobu (SEM) ve Atomik Kuvvet Mikroskobu kullanılmıştır. Hücreler, hücre davranışlarını değerlendirmek için 24 saat boyunca farklı topografilerin bulunduğu kontrol substratı (plastik tabak), cilalı silikon ve lazerle işlenmiş substratlar üzerinde büyütülmüştür. 24 saat sonra, hücre morfolojik tepkileri, konfokal mikroskopi ve SEM ile incelenmiştir. Ayrıca 24 saat sonra fokal adezyonla ilgili gen ekspresyon seviyeleri qRT-PCR ile ve protein ekspresyon seviyeleri Western Blot analizi ile ölçülmüştür. Tüm topografyalarda, plastik tabak üzerinde büyütülen kontrol hücrelerine kıyasla fokal yapışma ile ilgili gen ekspresyon seviyelerinin çoğunda önemli bir artış vardır. Ayrıca, özellikle aynı substrat üzerinde iki farklı topografya birleştirildiğinde, hücrelerin aktin liflerinin topografya çizgileri doğrultusunda hizalandığı gözlemlenmiştir. Hücreler farklılaştığında, aktin lifleri yön hizasında daha belirgin hale geldiği gözlemlenmiştir. Sonuç olarak, substrat topografisi sadece hücrelerin morfolojik davranışlarında değil, aynı zamanda gen ve protein seviyelerindeki değişikliklerde de kritik bir role sahiptir. Ayrıca, substrat topografisinin yayılma ve yapışma ile ilişkili farklı hücre davranışları üzerinde farklı etkileri olduğu bulunmuştur. Bu nedenle, bu davranışların gen ve protein seviyelerinde manipülasyonu için, farklı hücre hatlarında sağlık ve hastalık durumlarında hücre davranışlarını incelemek için umut verici bir yaklaşım olabilir.

Anahtar Kelimeler: Neuro-2A hücreleri, fokal adhezyon genleri, yüzey topografisi, silikon, görüntüleme

To my family and my honorary grandfather Arif Aygündüz

ACKNOWLEDGMENTS

In addition to teaching me how to do scientific research, this study showed me the importance of scientific collaboration and communication between your colleagues. Throughout these years, the number of people I would like to appreciate may reach to pages; however, I would like to mention as many as possible.

First of all my deepest appreciation and gratitude go to the principal investigators I worked with.

My advisor, Assoc. Prof. Dr. Çağdaş Devrim Son, welcomed me as an MSc student in his laboratory. He taught me all the principles of confocal microscopy, and he showed me how to analyze and interpret scientific data. He was always available for my questions and answered them in a very kind and supportive way. He always encouraged me to proceed when I feel tired and lost hope. He taught me how to troubleshoot an experiment when I failed an experiment. I am grateful for that, too. I think he is the type of advisor that everybody would like to work with. I always remember him with the cheerful and inspiring conversations we had. For having Assoc. Prof. Dr. Çağdaş Devrim Son as my advisor and finding a chance to work with him, I consider myself very lucky and blessed.

My co-advisor, Assoc. Prof. Dr. Alpan Bek welcomed me to his laboratory and made laboratory equipments available to me and encouraged me to collaborate with his students. He introduced me to the area of characterization and structuring and related biology applications. He always suggested new perspectives that I may not see for my experiments and my thesis. He taught me the principles of many techniques which I did not know such as femtosecond laser, SEM, and AFM. The course I took from him is also very satisfying and informative not only in the context of physics but also in biology. I would like to thank him for not only academic support but also for psychological support, too. I think he is also the type of advisor that everybody would like to work with him. For having this chance, I consider myself very fortunate and special.

It has been a great pleasure to work with such wonderful and supportive advisors throughout my master studies. I feel extremely fortunate to work with these admirable and wonderful advisors. While I am working with them, I have the right amount of freedom to do research and pursue my goals and I always feel their support and motivation even when they are not physically with me.

One of the jury members, Assist. Prof. Dr. Ihor Pavlov who built and maintained the femtosecond laser offered his help whenever I asked and suggest new ideas for structuring. His enthusiasm for this study motivated me further thinking. And I am very grateful for this.

I would like to express my gratitude for Assoc. Prof. Dr. Tülin Yanık for being my jury member, and for offering her advice and suggestions afterward. Also, I would like to thank her for letting me use her laboratory equipments whenever I needed them.

Last but not least, I would like to thank Assoc. Prof. Dr. Gamze Bora for being my jury member and sparing her precious time to attend to my thesis defense.

I would like to express my special thanks to the Scientific and Technological Research Council of Turkey for its 2211-National Graduate Scholarship program (2210-A). Thanks to this scholarship, I cover my expenses during my master studies.

The author also would like to thank the Office of Scientific Research Projects Coordination in METU for the partial funding for this Project under the grant number Graduate Thesis Project-10692.

I would like to thank past and recent members of the SON lab. I would like to thank Sara Mingu-Akmete for teaching me the basics of laser fabrication, and cell culture experiments. Precious conservations and brainstorming with her made me open to new ideas and help me to move further with this project. I would like to express my

gratitude to Seyda Tuğçe Balkan Durhan and Enise Nalli Sezer for helping me with my experiments, sparing cells when I needed and having cheerful conservations. I would like to thank Dr. Tuğba Dursun Usal and Dr. Fatma Kucuk Baloglu for sharing their deep experience and knowledge with me and answering my all questions. I would like to thank Tolgahan Suat Sezen for sparing cells whenever I needed them, for giving me emotional support, and for having a smiling face always. He made me feel his support even from Paris. I would like to express my deepest gratitude to İrem Aydın for emotional and experimental support. She always made wonderful morning coffee. She always helped with my experiment and provide her support whenever I needed it. She took care of some lab responsibilities of mine while I am very busy. Therefore, my deepest gratitude goes to her and her boyfriend, Berker Acır who cheered up both of us whenever we feel depressed.

Moreover, I would like to express my heartfelt gratitude to the members of the Nano-Optics group in the Physics Department. I would like to thank Arian Goodarzi for helping me with laser fabrication even if it takes hours, Milad Ghasemi for wafer cutting, and Nardin Avişan for taking EDS imaging. I would like to express my gratitude to Fırat İdikut for taking SEM imaging, giving me new ideas, and brainstorming about my experiments. I would like to thank Özge Demirtaş and Nardin Avişan for helping me cleaning of my silicon samples with an ultrasonic water bath. I would like to thank Samet Özdemir from GÜNAM, Physics Department for handing me over silicon wafers.

I would like to express my sincere gratitude to Assoc. Prof. Dr. Emrullah Görkem Günbaş, Dr. Zübeyir Elmazoğlu and other members of Günbaş Lab in the Chemistry department. They allowed me to use their confocal microscopy and Dr. Zübeyir Elmazoğlu helped me to process my images.

I would like to thank some labs in the Biological Sciences Department. My first and warmhearted gratitude goes to Banerjee lab in the department. Especially, I would like to thank Çağdaş Ermiş and Esin Gülce Seza for always helping my experiments, troubleshooting my experimental failure, and providing emotional support. Both of them are like teachers to me in addition to being good friends. Especially, Esin Gülce Seza helped optimization of the qRT-PCR and Western Blot experiments and provided good ideas. Also, Çağdaş Ermiş not only helped my experiments but also helped me with writing my thesis, and with all paperwork of the thesis. He is not only my friend but also like a brother to me. I wish him and her lovely wife, Damla Şahin Ermiş, a wonderful and full of love life in Germany. I think the pages are not enough to express my gratitude for them. I would like to thank Hepşen Hazal Hüsnügil, Göksu Oral, Aydan Torun, and İsmail Güderer for giving their help and suggestions for my Western Blot experiments. I learned many things from their deep experiences and suggestions. I would like to thank Nisan Korkmaz for having a smiling face always and bringing up my mood. I would like to thank Nazlı Menemenli for helping my Western Blot experiments even if it takes hours and days and for giving cheerful conservations both in the dormitory and in the department.

I would like to thank Zeynep Eda Akyıldız helping for optimization of my experiments, giving me wonderful ideas, and making super delightful Turkish coffee for me. She also always supported me during thesis writing.

I would like to thank my best supporter and friends Elif Akış and Besna Bülbül Tatbul. Our friendship lasts from the beginning of the university and I hope it lasts forever. Elif Akış is not only a friend, but also she is a good teacher, scientist, and sister. She helped with my experiments even though she is not physically with me. She always encouraged me to pursue my dreams. She always supported me and trusted my decisions. I wish to carry her in my pocket wherever I go. I wish her and her boyfriend Berksun Ceryan a good and full of love life wherever they go. I would like to express my deepest gratitude to Besna Bülbül Tatbul for being a good friend and supporter. I wish her and her husband Fatih Tatbul a healthy and full of love life. I would like to Yasemin Ceylan for being a good friend and supporter. I always remember her with a smiling face whatever happens. She always finds a way to be happy and to make people happy around her, especially me. She always comforts me when I feel very stressed. I wish her a healthy, and full of love life for the rest of her life.

I would like to express my deepest gratitude to the members of room 101. I cannot find words to express my love and gratitude to Nida Aslanyürek, Ayşe Nur Sarı, Handegül Ünalan, and Müjgan Kelce. We always be there for each other. They are with me whenever I feel unhappy, depressed, and stressed. I remember them acting like a mother to me during the intense exam weeks. They always supported and encouraged me. The pages are not enough to express my love and gratitude to them. I wish all of them a wonderful, happy and healthy life. I hope our lives might cross again in the future.

I would like to thank my recent roommates Hilal Erdeniz, Aysu Köseoğlu, and Yeşim Alkan. Although we met recently, I feel like we know each other for years. We stand together for our dormitory problems and solved them together. I remember our late-night conservations about academia and other things and supporting each other during this journey. I wish them wonderful and happy life for the rest of their life.

I would like to thank my second family which is the ODTÜ TEV Volunteers. I know many people from this family and some of them are life-long friends. I would like to thank some members of this family who are Ahmet Fırat Arslan, Zafere Deniz Güngören, Sümeyra Kaya, Dila Bulanık, Ayşegül Arslan, Muhammed Çetin, Alparslan İstif and Veli Can Çetin for their emotional support and encouragement. They are very successful and precious people and I believe that they will be very successful in the future. I would like to single out Diyar Turğut as one of the best emotional supporters. He always took good care of me even though I did not care. He always supported me and give me his care wherever I needed it. He is not only a good friend but also like a brother to me. I hope he will be very happy and successful in life.

I would like to mention my two heroes here who are my honorary grandfather Arif Aygündüz and my honorary big brother Emrah Arslan. If someone asks me to split my thesis two and give someone, I would give half of it to my family and the other half to Emrah Arslan and Arif Aygündüz. They are my heroes and right now if I can write this thesis, that is possible thanks to them. I wish I could find more words to express my gratitude to my honorary grandfather Arif Aygündüz and my honorary big brother Emrah Arslan, but words are not enough. I consider myself blessed and very lucky to meet them and I think knowing them is like a gift that life gave to me. I wish my honorary grandfather, Arif Aygündüz, a healthy and full of love life with his lovely wife Filiz Aygündüz for the rest of their life. Moreover, I wish my honorary big brother Emrah Arslan, a healthy, and full of love life with his lovely wife for the rest of their life.

Lastly but most importantly, I would like to express my deepest gratitude to my family My mother Ayşe Culfa, my father Hüseyin Culfa, and my sisters Şura Culfa and Tuğba Culfa deserve the biggest and deepest thanks. I think I have the best family in the world. I consider myself very fortunate to have such a family. I would like to thank my mother for bringing me and my lovely sisters, Şura and Tuğba, to this world. I think without her, none of us could succeed in anything. She always encouraged me and my sisters to pursue our dreams whatever it takes and always supported our decisions. She is always with me whenever I feel stressed, depressed, or happy. My father, who is another hero for me, always supported all of us and gave us unconditional love. My sisters, Şura and Tuğba, also always supported my decisions and understand me. That is why I am dedicating my thesis to my family and I think without them, I could not succeed in anything. I wish we live a long, happy, and healthy life all together.

TABLE OF CONTENTS

CHAPTERS

APPENDICES

LIST OF TABLES

TABLES

LIST OF FIGURES

FIGURES

LIST OF ABBREVIATIONS

ABBREVIATIONS

AFM	Atomic Force Microscopy
SEM	Scanning Electron Microscopy
EDS/EDX	Energy Dispersive X-ray Spectroscopy
CZ	Czochralski Method
1D	1 Dimensional
3D	3 Dimensional
2D	2 Dimensional
LIPSS	Laser-Induced Periodic Surface Structures
MC	Microcolumn
SPP	Surface plasmon polariton
P.D.	Plastic dish
DMEM	Dulbecco’s Modified Eagle Medium
%4 PFA	4% paraformaldehyde solution
ECM	Extracellular Matrix
EGFP	Enhanced Green Fluorescent Protein
FBS	Fetal Bovine Serum
LB	Lysogeny Broth
FA	Focal Adhesion
PBS	Phosphate Buffer Saline
TBS	Tris Buffer Saline
TBS-T	Tris Buffer Saline-Tween 20
ERK	Extracellular Signal-Regulated Kinase
Au	Gold
Pd	Palladium
N2a	Neuro-2a
DMSO	Dimethyl Sulfoxide

YAP	Yes-associated protein
TAZ	**T**ranscriptional Co-**A**ctivator with PD**Z**-Binding Motif
LP	Lamellipodia
LM	Lamellar actin (LM)
FAK/PTK2	Focal Adhesion Kinase/ Protein Tyrosine Kinase 2
FLNa	Filamin A
Lmna	Lamin A/C
FN	Fibronectin
TLN1	Talin 1
TLN2	Talin 2
Src	Proto-oncogene tyrosine-protein kinase/ proto-oncogene c-Src
aGPCR	Adhesion G Protein-Coupled Receptor

CHAPTER 1

INTRODUCTION

1.1 Rationale for studying mechanotransduction

The cells are known to sense various mechanical stimuli and respond to them. This process is known as mechanotransduction. Delivery of a mechanotransduction signal requires sensing mechanical forces and biomechanical cues. This information triggers a specific intracellular signaling response when these signals are perceived. The actin cytoskeleton also plays an important role in mechanotransduction by connecting the cellular compartments to the mechano-sensing mechanism.

Extracellular Matrix (ECM) surrounding cells are composed of many different proteins, including laminins, fibronectin, and collagens which have a role in sensing and interpreting of mechanical properties of ECM. Abnormality in the cells' mechano-sensing mechanism is observed in various diseases ranging from muscular dystrophies and cardiomyopathies to cancer progression and metastasis (Jansen *et al.*, 2017).

Therefore, for successful medical implants, as well as artificial organs and regenerative medicine applications, it is critical to understand cells' response mechanism to environmental cues and implement this information to obtain the desired results. By a reductionist approach, different mechanotransduction-related cues can be studied.

In the present work, the topography-induced mechanotransduction effect in Neuro-2A cells was studied in which nano/microtopographies were created using a femtosecond laser on a silicon substrate. Silicon is widely used as a cell substrate material in the field. In Mingu’s work, the effect of topography created by a femtosecond laser was studied in Neuro-2A cells. In this study, not only topography-induced morphological changes but also gene expression level changes are studied which makes this study novel in the related field literature. With the help of this study’s results, cells can be manipulated at the gene level for different purposes, especially for the improvement of implants, tissue engineering, and artificial organ studies.

1.2 Mechanism of mechanotransduction

1.2.1 The actin cytoskeleton and mechanotransduction

One of the most sophisticated and multi-functional animal cell structures is the cytoskeleton, which has roles in various processes such as adhesion, motility, force sensing and transmission, endocytosis, cell division, intracellular transport, and adaptation of cell shape. These processes are carried out by three classical cytoskeletal filament types; actin, microtubules, and intermediate filaments (Hohmann & Dehghani, 2019). Some evidence proposes the role of microtubules and intermediate filaments in mechanosensation; however, there is no direct evidence that they are mechanosensor on their own.

These three cytoskeletal filaments are responsible for sustaining cell shape and controlling eukaryotic cells' mechanics. In addition, they can respond to external forces and maintain the integrity of intracellular compartments. Several classes of regulatory proteins control the architecture of the networks constructed by cytoskeletal proteins: filament formation is initiated by nucleation-promoting factors, filament growth is terminated by capping proteins, polymerases control filament growth, disassembly of filaments is ruled by depolymerizing factors and severing factors. External or internal mechanical forces can change the arrangement of these regulatory factors by affecting the activity of these factors. These regulatory factors differ from each other, considering their mechanical stiffness, assembly and disassembly dynamics, polarity, and molecular motors associated with them (Fletcher & Mullins, 2010).

There are two distinct states of actin available which are monomeric G-actin and filamentous F-actin. The arrangement of the actin cytoskeleton is controlled with the balance of globular G- and polymeric F-actin and with actin-associated proteins. The force generation, which is critical for movement, focal adhesion, and shape changes, is related to polarized filaments formed by the actin cytoskeleton.

Actin is the most dynamic cytoskeletal protein compared to the other two. Actin monomers called globular actin (G-actin) polymerize to form a single actin filament that is called filamentous actin (F-actin) (Hohmann & Dehghani, 2019).

It is known that with force applied to the cells, actin filaments can act as a mechanosensor. It is reported that when the cells come across a force, they form stress fibers parallel to the direction of the force. These stress fibers, composed of actin and myosin II filaments, are generated by the change in the structure of actin filaments due to mechanical force. The affinity of actin severing protein, cofilin, is reduced by the applied force, and myosin II's affinity to the actin filaments is elevated (Ohashi *et al.*, 2017).

The effects of changes in actin filament dynamics by mechanical stress are observed in the regulation of cell proliferation and gene expression, too. Downstream effectors of the Hippo pathway, which are Yes-associated protein (YAP) and WW Domain-Containing Transcription Regulator Protein 1 (WWTR1/TAZ), shuttle into the nucleus and initiate a signaling response when they sense stimuli from ECM (figure 1.1) (Martino *et al.*, 2018).

When cells are exposed to a stiff substrate or tensile force, an increase in the ratio of F-actin to G-actin and the formation of actin stress fibers are observed. As a result of these changes, nuclear translocation and activation of transcription coactivator YAP occur, and cell proliferation and differentiation-related genes' expression are elevated with the formation of a complex with the transcription factor TAED.

In contrast, when cells adhere to a soft substrate, these changes are reversed in a way that stress fiber formation is inhibited by ROCK or myosin II inhibitors, and YAP is phosphorylated by its upstream kinase, LATS, and its activity is inhibited. This mechanical force-mediated regulation of YAP is observed in organ size control and cancer malignancy in various tissues. Thus, it is vital to understand the mechanism of mechanical-force induced changes in the actin cytoskeleton dynamics, which plays a critical role in mechanical force associated with cell proliferation, differentiation, tissue homeostasis, organ size control, embryogenesis, and cancer progression (Ohashi *et al*., 2017)

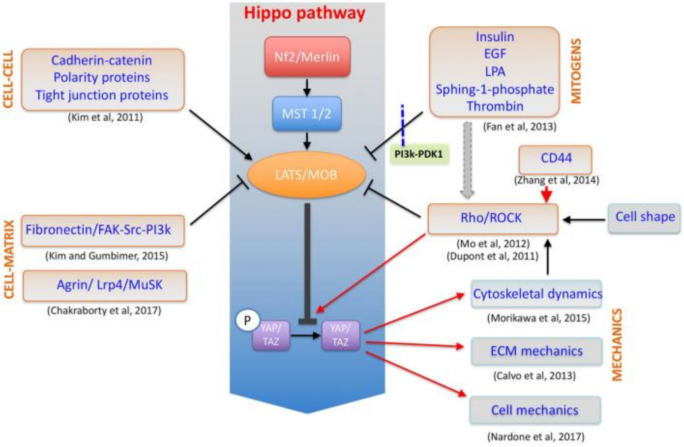

Figure 1.1: *YAP/TAZ in cellular mechanotransduction*

YAP/TAZ effectors' roles in various mechanosensing and biological pathways which plays a role in cytoskeleton dynamics, ECM structure stabilization, and cell mechanics. Adapted from Martino et al., 2018.

1.2.1.1 The Lamellipodium

The lamellipodium, structure shown below (figure 1.2), is related to cell movement, and it is formed by the polymerization of actin. For the generation of the lamellipodium, Scar/WAVE complex together with the activation of the small Rho GTPase Rac1 should activate the intrinsically inactive Arp2/3. To the existing filaments, a new actin filament is added by Arp2/3 complex (Hohmann & Dehghani, 2019)

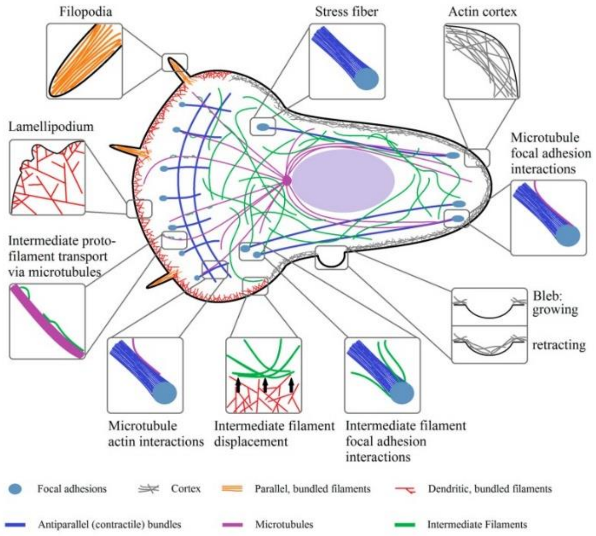

Figure 1.2: *Graphical representation of actin, microtubules, and intermediate filaments' organizational structure inside a cell and their interactions. Adapted from Hohmann & Dehghani, 2019.*

Lamellipodia's role in the directional migration of cells is well known. Lamellipodial protrusion formation is the first step of cell migration and is positively correlated with cell migration. Because it is known that cell migration is affected by mechanical signals such as substrate stiffness and mechanical forces, lamellipodia (LP) movement is also dependent on these signals. However, the mechanism of this mechanosensing process is not clear. Recent studies show that cell spreading area, magnitude, and distribution of cell spreading are affected by substrate stiffness, and as a result, cell migration is affected, too. Regulation of LP's continuous movement is balanced with two reverse processes, which are protrusion and retraction (figure 1.3). In the protrusion process, the cell membrane is pushed forward by actin polymerization, and in the retraction process, as the name implies, LP actin is pulled back by myosin motors (He & Ji, 2016).

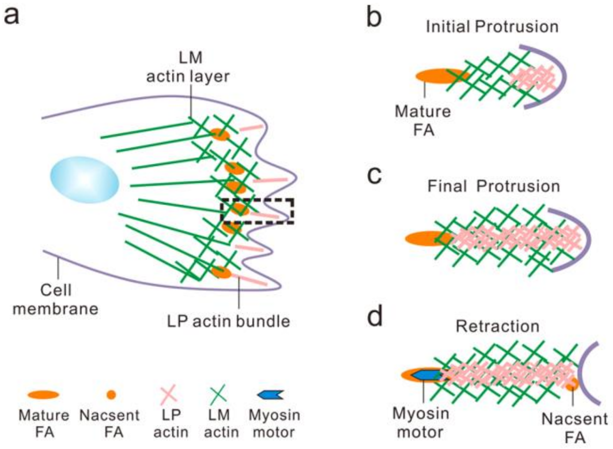

Figure 1.3: *At different stages of protrusion and retraction, lamellipodia organizational composition of a spreading cell.*

(a) Front view of a polarized cell. (b) at the beginning of protrusion: a mature FA (big orange ellipse), lamellar actin (LM) layer (green cross), short, newly developed lamellipodial actin (LP) (pink cross) (c) at the end of the protrusion, mature FA with fully developed LP actin layer. (d) final stage of the retraction in which LP actin is retracted by Myosin II (blue arrow) pulls the cell membrane backward. Adapted from He & Ji, 2016.

1.2.1.2 The Filopodia

Another structure related to cell motility is filopodia which has a role in sensory functions in neurons. They have a diameter of 100-300 nm and are composed of 12-20 actin filaments. A common mechanism for the formation of filopodia is that with the activation of Arp2/3, actin polymerization starts. Another model suggests that in adherent cells, there is no requirement for Arp2/3 activation for filopodia initiation. In addition to their role in cell movement, they have a role in cell-to-cell contacts, the transmission of cell-cell signals, and response to mechanical forces (Hohmann & Dehghani, 2019).

Filopodia's role in sensing the microenvironment, including both the ECM and properties of other cells, can be observed best in embryonic development during dorsal closure and ventral enclosure by sensing the microenvironmental properties of the cells. Filopodia signaling is best understood in axon pathfinding, also called axon guidance, where nerve cells search for its axon through various tissues to find its target, which will innervate to it (Heckman & Plummer, 2013).

1.2.1.3 The Stress Fibers

The third type of actin-associated structure that is neither present in filopodia nor in the lamellipodium is stress fibers (figure 1.2) They are built from bundles of anti-parallel actin filaments composed of myosin II or parallel filaments. Stress fibers are composed of 10-30 actin filaments that are linked to focal adhesions. Focal adhesions, like a bridge, connect the cells to the substrate. Stress fibers are one of the ways that regulate cell contractility in many animal cells. For example, stress fibers are usually thick and relatively stable in non-motile cells. However, in motile cells, they are fewer and highly dynamic. Stress fibers do not only include cross-linkers such as α-actinin, but also they include further cross-linkers such as fascin, filamin, and paladin. One hypothesis suggests that these proteins regulate cytoskeletal dynamics. Generally, stress fiber formation requires activation of the formin mDia1 and the small Rho GTPase RhoA, which activates ROCK. The formin supports actin polymerization and ROCK, which activates myosin, and induces stress fiber formation (Hohmann & Dehghani, 2019).

1.2.2 Integrins, Focal adhesions, and Mechanosensitivity

A superfamily of cell adhesion receptors, integrins, recognize extracellular matrix ligands, cell-surface ligands, and soluble ligands. They are heterodimeric transmembrane receptors containing α and β subunits. So far, with the combination of 18α and 8β subunits, 24 different subtypes of integrins have been discovered in vertebrates. Integrins are found in various organisms from mammals, chickens, and zebrafish, as well as lower eukaryotes such as sponges, the nematode *Caenorhabditis elegans, and* the fruitfly *Drosophila melanogaster.*

One of the main functions of integrins is to sense and transmit changes in the mechanical properties of the ECM. They can generate an intracellular signal upon binding an extracellular ligand, and also signals from within the cell can regulate their function. Through effects on the cytoskeleton, integrin signaling modulates various cell behaviors such as adhesion, proliferation, survival or apoptosis, shape, polarity, motility, and differentiation.

There are gene knockout studies in mice that show particular integrins have a critical role in the development, such as αV integrins are responsible for vasculogenesis, α9β1 for lymphangiogenesis, α6β4 for sustaining the integrity of the skin, and the β2 integrins for immune responses. In another study, knocking out the gene for β3 results in enhanced tumorigenesis and angiogenesis, wound healing, and increased inflammation and atherosclerosis, which proves that the gene αVβ3 inhibits these processes (Takada *et al*., 2007).

Many of the signaling functions of integrins are controlled by a cytoplasmic protein tyrosine kinase called focal adhesion kinase (FAK). Focal adhesions are the most well-known sites for tyrosine phosphorylation in cells in culture, and one of the major tyrosine-phosphorylated proteins in focal adhesions is FAK. With the clustering of integrins at the cell-matrix contact, FAK is recruited to focal adhesions, one of the intracellular anchor proteins such as talin. Talin binds to the integrin β subunit or paxillin which binds to one type of integrin α subunit. On a specific tyrosine, clustered FAK molecules cross-phosphorylate each other and form a phosphotyrosine docking site for members of the Src family of cytoplasmic tyrosine kinases. Different docking sites are created for various intracellular signaling proteins via the phosphorylation of FAK on additional tyrosines by these kinases. As a result, the signal is transmitted into the cell. In a study, to see the importance of FAK on focal adhesion behaviors of cells, FAK-deficient fibroblasts are created. In the study, adherence of FAK-deficient fibroblasts to fibronectin is observed. However, focal adhesion formation was too low; as a result, cell spreading and migration slowed down. These findings claim that, usually, FAK is responsible for the disassembly of focal adhesions, which is required for regular cell migration. This conclusion can explain why cancer cells are more mobile than healthy cells because they have an increased level of FAK (Alberts *et al*., 2002).

Focal adhesions (FAs) are plasma membrane-associated macromolecular assemblies that join to the extracellular matrix (ECM) via integrin receptors. With the help of various FA-associated proteins, they join to the actin cytoskeleton. For FAs to grow and change their composition, they have to undergo a maturation process induced by biochemical or physical signals. These changes, such as FA size, distribution, dynamics, and composition, are required to transmit specific signaling related to the cells' response to different environmental cues (Kuo, 2014).

Various proteins (180 proteins) have been reported to interact with FAs to form integrin adhesome. These are cytoskeletal proteins, adaptor proteins, and signaling proteins, such as kinases, phosphatases, phospholipases, and regulators of small GTPases. Interactions between the proteins depend on the presence of specific scaffolding motifs, and these interactions are regulated by specific signaling events such as phosphorylation (or dephosphorylation) or via regulation of small GTPases. Scaffolding proteins, which have a specific scaffolding motif, connect the actin cytoskeleton to the integrin receptors through direct or indirect interactions; however, regulator proteins regulate the connection between actin filaments and integrin receptors via their abilities to regulate FAs' activity, stability, or functionality. In general, scaffolding proteins include actin-binding proteins and adaptor proteins such as Talin, α-Actinin, Filamin A/B/C, Vinculin, VASP, and Zyxin; for regulatory proteins, Src, Ptk2 (FAK), Gnb1, and Yes1 might be given as an example (figure 1.4*)* (Kuo, 2014).

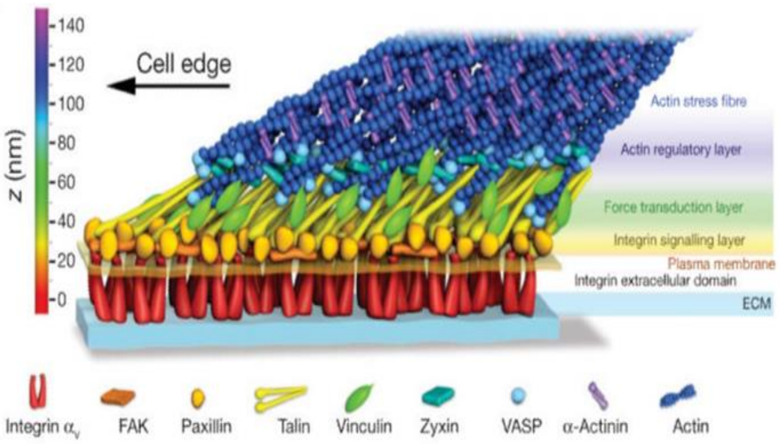

Figure 1.4: *Graphical representation of focal adhesion molecular structure. Adapted from Kanchanawong et al., 2010.*

How FAs' mechanosensitivity works are not well understood. How cells' response to different environmental cues results in changes in the dynamics of FAs is not well defined. It is known that the initial formation of FAs is regulated by integrin receptors, and then FAs go through a maturation process, after which either they stabilize or disassemble. However, how the stimuli from the environment are sensed and a signaling event is initiated is unknown. It is known that small G-proteins belonging to Rho-family modulate the assembly and dynamics of FAs. For example, by activating small GTPase RhoA, the epidermal growth factor (EGF) supports FA maturation. Also, it is shown that the triggering of G protein-coupled receptors (GPCRs), such as with thrombin, results in cell adhesion and aggregation by triggering talin binding to integrin αIIbβ3 and activating integrin-mediated signaling (Kuo, 2014). The largest cell surface protein family, GPCRs, acts as versatile sensors for various bio/chemical messages which makes them an important player in cell mechanotransduction. Therefore, they deserve to be mentioned when cell mechanotransduction is studied.

GPCRs are the largest receptor family, and they are shown to respond to various extracellular stimuli such as photons, odor, and taste. Mechanical stimulation is recently shown to activate GPCRs among the various ligands. Several GPCRs are found to be mechanosensitive. Some reported mechanosensitive GPCRs are angiotensin II type 1 receptor (AT1R), GPR68, endothelial histamine H1 receptors (H1Rs), and several adhesion GPCRs (aGPCRs).

The remarkably extended (ranging from ~300 to 6000 amino acids) extracellular region (ECR) proximal to the seven-span transmembrane (7TM) region makes aGPCRs different from the canonical GPCRs. Particularly, various cell-adhesive protein motifs involved in cellular adhesion are found in the N-terminal region of the aGPCR-ECR. Seven potential mechanosensitive adhesion GPCRs are ADGRE2/EMR2,ADGRE5/CD97,ADGRL1/Latrophilin/CIRL, ADGRV1/VLGR1, ADGRG1/GPR56, ADGRG5/GPR114, and ADGRG6/GPR126 (Lin *et al*., 2022).

One example of the mechanosensitive property of aGPCR can be found in a study in which LPHN/CIRL/ADGRL regulates sensory neurons in Drosophila via cAMP-dependent modulation of ionotropic receptors.

The available data in the literature suggests that aGPCRs engage in *cis* or *transcellular* conversation with integrins. By interacting with ECM molecules, aGPCRs involve in the arrangement of cytoskeletal architecture indirectly through G-protein, Rho, and Rac-dependent signaling pathways and directly, e.g., via PDZ proteins. Therefore, aGPCRs might have a role in the connection of ECM and cytoskeleton.

One of the most studied aGPCRs in cancer progression, GPR56, is known to couple to $G\alpha_{12/13}$/RhoA. Rho-dependent signaling is shown to play roles in control contractility, stress fiber formation, and FA reinforcement. GPR56’s localization at the leading edge of membrane filopodia and its localization with α-actinin in human glioma cells confirms its role in cell migration, FA formation, and adhesion processes (Scholz, 2018).

Evidence for GRP56’s role in cell adhesion can be found in various cancer research studies. For example, in one study, GPR56, by internalizing and degrading its ligand TG2, the ECM crosslinking enzyme, caused lower expression of fibronectin and

FAK. These results might propose a mechanism that the accumulation and crosslinking of ECM in tumors might be reversed (Yang *et al*., 2014).

Although there are common theories about the recruitment of scaffolding and regulatory proteins at FAs for mechanoresponsive signaling events, specific FAs proteins that act as force-sensitive or force-responsive proteins still need to be determined. To date, there are several microscopy and proteomics studies conducted that shows FAs components change in response to mechanical force; however, which FAs proteins act like force-sensitive molecule has not been determined yet (Kuo, 2014).

Commonly accepted information from various research groups proposes a possible mechanism(s) for mechanosensitive behavior of FAs: (i) when integrins come across with a force, they tend to cluster due to increased actomyosin recruitment and cytoskeletal assembly. This might result in an increase in receptor density and integrin signaling, and (ii) that force causes a conformational/compositional change in FAs so that new binding interactions can be created or direct modulation of enzymatic activity can be carried out (figure 1.5). Conformational changes cause the activation of tyrosine kinases, such as FAK, to modulate mechanotransduction (Goldmann, 2012).

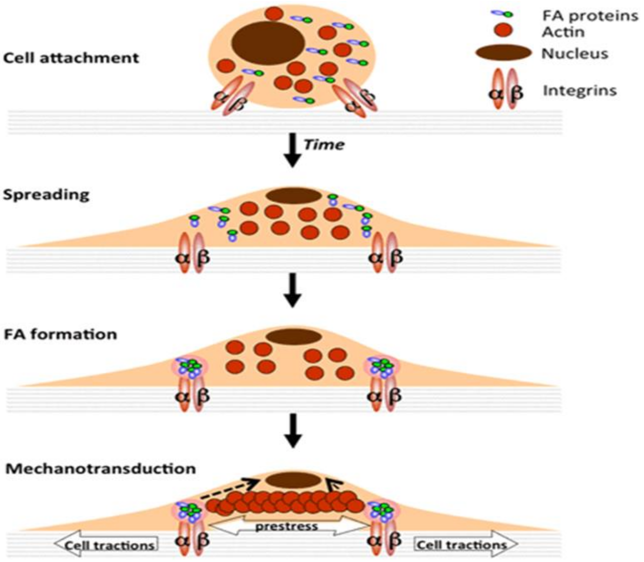

Figure 1.5: *Binding of a cell to the ECM.*

Binding of the cell to the ECM through integrins induces cell spreading and the formation of Fas. Internal pre-stress and cellular tractions are generated with the binding of the cell to the actin cytoskeleton and the signal is transmitted to the nucleus. Adapted from Goldmann, 2012.

1.2.3 Extracellular matrix and its response mechanism to different environmental cues

The extracellular matrix (ECM) is important for the function and integrity of the soft connective tissues. The ECM is established during development, sustained in health, remodeled during adaptations, and repaired in response to injury and disease. In addition, ECM has roles in various cellular functions such as growth, migration, differentiation, and even survival. In addition to the chemical composition and structural organization of ECM, mechanical forces also affect cell-ECM interactions. In order to maintain mechanical homeostasis, cells should modulate ECM mechanics by sensing and responding to environmental signals (Humphrey *et al*., 2014).

The formation of adhesions involves two cooperative processes: binding to ECM proteins and linkage to the actin cytoskeleton.

In addition to regulating FAs composition, cells respond to force by remodeling the ECM. The mechanism for this remodeling has not been clearly defined; however, matrix assembly usually is in the direction of applied force. For example, collagen and fibronectin fibrils tend to align themselves in the same direction with force (Schwartz, 2010).

Also, cells sense the rigidity of the ECM that they are on or in and adjust themselves accordingly. For example, on stiffer matrices, cells have a tendency to develop more stable FAs and more actin stress fibers which result in cell spreading; however, on softer matrices, less developed and less numerous stress fibers and focal adhesions are observed (Schwartz, 2010). This sensing mechanism, which is the softness or rigidity of the ECM, depends on actomyosin contractility, which is regulated by the RhoA/ROCK pathway: actin polymerization is triggered by the small GTPase RhoA via its effector mDia1, and actomyosin contraction is triggered via the activation of Rho-dependent kinase ROCKI/II by small GTPase RhoA (Chiquet *et al*., 2009).

In addition to rigidity and force, substrate topography is another mechanotransduction type that cells use to communicate. Neurons and neural stem cells are highly sensitive to the mechanical and topographical environment that cell-substrate interactions induce various signaling pathways for different cell functions (Stukel & Willits, 2016).

Specific mechanisms for neuronal signaling remain unknown. However, the link between mechanosensitive molecules and the cytoskeleton is clear. Cell shape, which is affected by changes in the cytoskeleton structure, results in changes in signaling events and cell behavior. Substrate topography affects the direction and length of neurite growth, a critical parameter for neuronal regeneration.

By using defined topographical features, cell shape can be manipulated. Patterned ridges and grooves are commonly used in neural research because these topographies mimic glial cells and neurons' aligned patterns *in vivo*. Usage of ridges and grooves is not only limited to neural research (Stukel & Willits, 2016). For example, in one study, human corneal epithelial cells are cultured on a silicon oxide substrate on which there are 70 nm wide ridges and 600 nm depth grooves on a 400 nm pitch (figure 1.6). According to their results, cells cultured on patterned substrate show elongation and alignment along the direction of the patterns 12 hours after cell seeding (figure 1.6A). On the contrary, cells cultured on a nonpatterned/smooth substrate show no alignment. They have primarily round shape (figure 1.6B) (Teixeira *et al*., 2003).

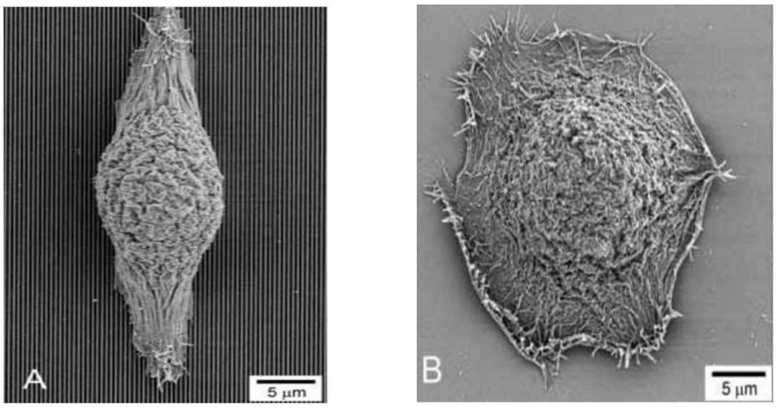

Figure 1.6: *SEM images of human corneal epithelial cells*

(A) cells seeded onto a silicon oxide substrate on which 70 nm wide ridges, on 400 nm pitch patterns. The groove depth was 600 nm. (B) Cells on a smooth silicon oxide substrate. Adapted from Teixeira et al., 2003.

1.2.4 Mechanotransduction and related signaling pathways

Earlier studies on mechanotransduction mostly focused on ECM binding domains and adhesion complex proteins which are involved in the connection of the cytoskeleton to the extracellular environment. Later, how significant the cytoskeleton is and its connection to the nucleus has been investigated. Although, how mechanical signals are translated into transcriptional changes still remains unknown. A paper by Dupont and colleagues (2011) found that two transcriptional coactivators **Y**es-**a**ssociated **p**rotein (YAP) and **t**ranscriptional co-**a**ctivator with PD**Z**-binding motif (TAZ), were found to be indispensable for transcriptional and phenotypical changes related to the biophysical signals from the extracellular environment. These two coactivators are situated at the center of at least four signaling pathways (biophysical, Hippo, TGFβ/BMP, Wnt) and have an indirect effect on several (Retinoblastoma, IGF, PI(3)K/Akt) and act as orchestrating molecules for the integration of biophysical signals from the environment into signaling pathways (figure 1.7) (Morgan *et al*., 2013).

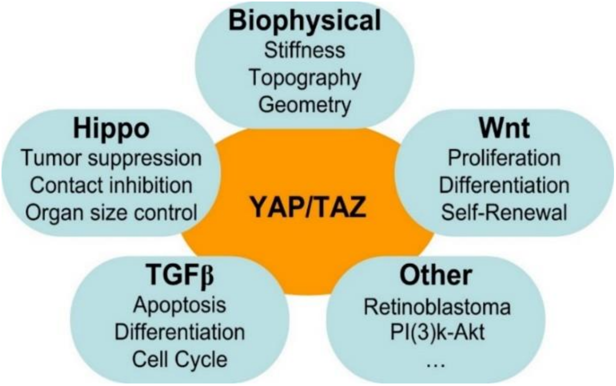

Figure 1.7: *YAP/TAZ transcriptional coactivators in different signaling pathways. Adapted from Morgan et al., 2013.*

Note: this schematic does not represent all known YAP/TAZ interactions but it is intended to clarify the major interactions in YAP/TAZ signaling.

YAP/TAZ as the main target of the Hippo pathway, has been implicated in mechanotransduction signaling. Moreover, it has different roles in TGFβ, Wnt, and other proliferation and differentiation pathways (Morgan *et al*., 2013).

Hippo (Hpo) pathway, as the main target of YAP/TAZ, was initially identified as a result of a genetic screen for cell size control in Drosophila melanogaster, and it was shown that it is a conserved pathway that controls organ size, cell fate, tissue homeostasis, and tumor progression. As a core kinase cascade, it includes Hpo/mammalian Ste20-like kinases 1/2 (MST1/2), Salvador (Sav)/SAV1, Mats/MOB kinase activator 1A/B (MOB1A/B), and Warts (Wts)/large tumor suppressor kinase 1/2 (LATS1/2). The latter one has an important phosphorylation role in preventing target gene activation by phosphorylating the transcription factor

Yorki (Yki)/Yes-associated protein (YAP)/transcriptional coactivator with PDZ-binding motif (TAZ) (Chang *et al*., 2020).

Recent findings indicate the localization of Hpo pathway components at the cellular junctions, which help to gain a better understanding of how cellular morphology, the extracellular environment, and F-actin architecture all together orchestrate to regulate the Hippo signaling pathway (figure 1.8) (Chang *et al*., 2020).

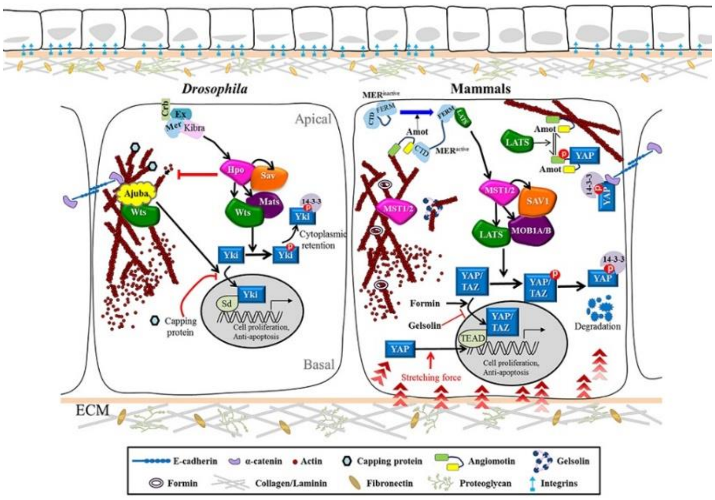

Figure 1.8: *Cytoskeletal regulation by Hippo pathway in Mammals and Drosophila. Adapted from Chang et al., 2020*

When Hippo signaling is turned off, target genes activation occurs as a result of binding of the nuclear effector Yki/YAP/TAZ to the transcription factor Sd/TEAD. Phosphorylation of Hpo/MST1/2 by upstream stimuli, Wts/LATS1/2 is activated and phosphorylates Yki/YAP/TAZ, and as a result of this, the later ones stay in the cytosol or undergo degradation. Hpo, Hippo; Sav, Salvador; Wts, Warts; Yki, Yorkie; Sd, Scalloped; LATS1/2, large tumor suppressor kinase 1/2; MST1/2, mammalian Ste20-like kinases 1/2 (Chang *et al*., 2020).

Hippo pathway involvement in the regulation of cellular morphology comes from a cell culture study in which colocalization of filamentous actin with MST1/2 and MST1/2 activation as a result of disruption of stress fibers are observed (Densham *et al*., 2009).

Moreover, in Drosophila studies, tissue outgrowth is observed when there is a mutation in the Hippo pathway. For example, F-actin accumulation and overexpression of the Yki target are observed when a mutation in capping proteins, a negative regulator of actin polymerization occurs. As a result, tissue outgrowth is observed in imaginal discs (Fernandez *et al*., 2011; Sansores-Garcia *et al*., 2011).

In the paper of Dupont and colleagues (2011), nuclear localization and transcriptional activation of YAP are prevented by soft substrates, restrictive geometry, and actinomyosin disruption. The study showed that YAP/TAZ activity is regulated by mechanical cues such as geometry and substrate stiffness via the regulation of the actinomyosin cytoskeletal system.

These results suggest the importance of the Hippo pathway in cell size control and F-actin regulation. Moreover, localization and phosphorylation of YAP/TAZ might be modulated by regulating the cytoskeleton, the mechanical cues, and Rho-signaling (Morgan *et al*., 2013).

Rho signaling is another important mechanotransduction-related pathway in which Rho-family small GTPases have a role in the modulation of remodeling of the actin cytoskeleton. There are approximately 20 members of the Rho GTPase family in the human genome including RhoA, Rac1, and Cdc42 which have roles in actin cytoskeletal remodeling. Mechanical stress activates RhoA and inhibition of its downstream effectors such as Rho-associated kinase (ROCK) or mammalian Diaphanous (mDia) influence stress fiber reorientation. Activation of Rac1 is also triggered by mechanical stimuli and the mechanotransductive related response of endothelial cells and other cell types is dependent on Rac1 activation. These findings show that Rho signaling has an important role in mechanotransductive signaling (Ohashi *et al*., 2017).

Particularly two Rho GTPase activating proteins (GAPs) attracts the attention for their role in mechanotransduction and RhoA activity which are the tumor suppressor Deleted in liver cancer 1 (DLC1) and p190RhoGAP (Burridge *et al*., 2019)

DLC1 protein particularly attracts attention because of its recruitment to focal adhesion. The mechanosensitive protein talin is its binding partner in focal adhesions. The binding of DLC1 to the R8 domain of talin leads to activation of DLC1 and a decrease in the active RhoA levels. However, when there is enough tension to stretch talin and open up the R8 domain, the inhibition of DLC1 is reversed and RhoA activity is increased. Talin and DLC1 interaction for the regulation of RhoA activity suggests the importance of mechanical tension in the regulation of RhoA activity.

Upon mechanical tension is exerted, another cause of the increased activity of RhoA is the inhibition of p190RhoGAP. This finding is discovered in studies of fibroblasts of patients with idiopathic pulmonary fibrosis (IPF). Although the underlying reasons for IPF have not been clear, a major factor for the promotion of fibrosis is the increased level of TGFβ. Also, there is much evidence suggesting a major role of RhoA in this disease, as well as other types of fibrosis. It is found that decreased activity of p190RhoGAP is observed both in fibrotic fibroblasts and in response to TGFβ. Accumulation of excess ECM, which causes increased stiffness of fibrotic tissues, is a characteristic feature of the disease. It is shown that enhanced RhoA activity is triggered by elevated stiffness. Both diminished activity of Rnd3, the activator of p190RhoGAP, and p190RhoGAP have been observed in fibroblasts when they adhere to a rigid substrate suggesting that this pathway might be responsible for the increased RhoA activity when cells are exposed to a rigid substrate. Because increased mechanical tension and rigid substrate also stimulate TGFβ activity, a positive feedback signaling, including Rnd3 and p190RhoGAP is triggered upon mechanical stimulation and rigid microenvironment (Burridge *et al.*, 2019).

Another pathway that is at the heart of mechanotransductive signaling in the cell is TGFβ signaling. Static and dynamic physical signals which are at the macro level are delivered to the micro level and as a result, the TGFβ pathway is regulated at each level.

It is known that there is a feedback loop between ECM regulation and TGFβ signaling when a cellular response to biophysical cues is regulated. ECM synthesis and remodeling, which regulates cytoskeletal tension, is modulated by TGFβ and in turn, cytoskeletal tension-dependent regulation of TGFβ can be observed at several hierarchical levels involving transcription, translation, ligand activation, and expression of downstream lineage-specific transcription factors. These transcription factors, in turn, affect the expression of TGFβ-regulated specific ECM proteins such as fibronectin, collagens, and other matrix glycoproteins. Via this feedback loop, TGFβ sustains cellular mechanical integrity continuously by responding to dynamic biophysical cues (Rys *et al*., 2016).

One type of these biophysical cues, which is topographical patterns, is highly studied in the context of mechanotransduction-induced TGFβ signaling. For example, a study by Vermuelen and colleagues (2019) reported that the upregulation in the expression of the TGFβ-responsive gene, Scxa, encoding Scleraxis in tenocytes is induced by surface topographies. Later Vermuelen and colleagues (2020) showed that microtopographies result in the elevation of expression level in tendon-specific transcription factor scleraxis (SCX) and transforming growth factor-β type II receptor (TGF-βR-II) in adipose-derived mesenchymal stem cells (MSCs). Also, they showed that for microtopographies to increase the expression of SCX, actin dynamics and the Rho/ROCK/SRF signaling pathway are a prerequisite (Vermeulen *et al*., 2020).

From the perspective of the non-canonical TGF-β signaling pathway, F-actin is activated by Rho and ROCK, and ROCK and mammalian diaphanous (mDia) are activated by RhoA. Activation of MCC regulator of Wnt signaling pathway (MCC) and LIM domain kinase (LIMK) occurs through ROCK; in turn, LIMK activates Cofilin, and F-actin is activated by mDia, MCC, and Cofilin. This regulation is an example of a cascade amplification process (figure 1.9).

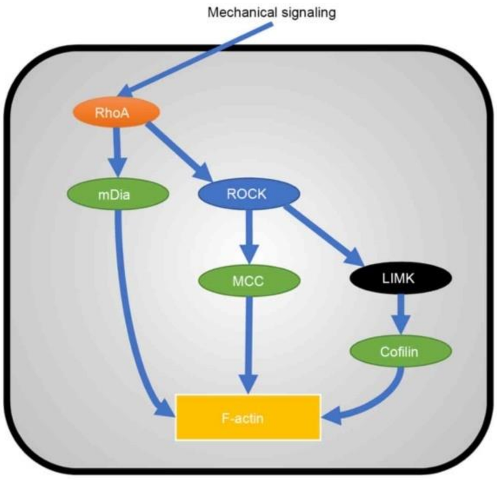

Figure 1.9: *Rho and TGF-β signaling pathway in the regulation of F-actin dynamics. Adapted from Li et al., 2021.*

In canonical TGFβ/bone morphogenetic protein (BMP), which occurs through SMADs shown to be sensitive to mechanotransductive signals. It is known that YAP/TAZ transcriptional coactivators are mechanoregulators of TGF-β-SMAD signaling. Interaction of YAP/TAZ with SMAD2/3 has a critical role in SMAD nuclear-cytoplasmic shuttling. TGF-β signaling is inhibited with the sequestering of SMAD2/3 protein in the cytosol as a result of YAP nuclear exclusion. BMP-induced transcriptional activity is augmented with the binding of YAP to the activated SMAD1 protein. Moreover, another regulation of TGF-β signaling by YAP/TAZ is to function as an endogenous repressor of SMAD7 (Li *et al*., 2021). These findings indicate the interdependency between the different cellular pathways for the regulation of cell response to biophysical cues in the environment. Different mechanical cues activate and/or inhibit various regulators of different signaling pathways as explained above. As a result of these changes in the related signaling pathways, changes in cell behavior related to cell adhesion, migration, proliferation, differentiation, and cell polarity are observed. When cell proliferation, cell fate determination, migration, and related biological processes are in question, the evolutionarily conserved Wnt pathway may be the first signaling pathway that comes to mind. Therefore, the mechanotransduction and Wnt signaling pathway relationship has been critically studied in the literature (figure 1.10).

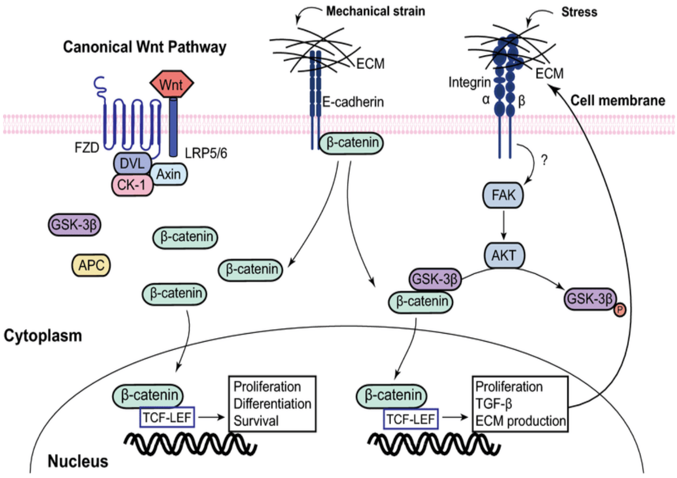

Figure 1.10: *Role of Wnt/β-catenin signaling pathway in mechanotransduction. Adapted from El Sabeh et al., 2021.*

Wnts as secreted proteins have diverse and critical regulators of development. Their binding to the Frizzled (FZ) family of receptors and members of the low-density lipoprotein receptor-related protein (LRP) family leads to the activation of different intracellular signaling to regulate various cell behaviors. Wnt signaling regulates cell polarity, actin cytoskeletal architecture, and contractile forces which makes this pathway an important target of mechanical cues. For example, it is found that strain-induced mechanotransduction in osteoblasts is controlled by Wnt co-receptor LRP5 (Wozniak & Chen, 2009).

In addition to bone remodeling, mechanotransduction-induced Wnt signaling regulation is also observed in mesenchymal stem cells (Kuo *et al*., 2015) and vessel maturation and repair in zebrafish (Li *et al*., 2014).

For example, as a mechanical cue, topography also might have a role in Wnt signaling. A study by Galli and colleagues (2010) showed that rough titanium (Ti) surfaces result in an increase in the stimulation of b-catenin/ TCF signaling and translocation of b-catenin to the nucleus. In addition to the topography-induced activity of b-catenin, topography modulates the expression of Axin 2, which is a b-catenin degradation regulator (Galli *et al*., 2010).

Another pathway affected by mechanical cues is one of the evolutionarily conserved pathways, which is the Notch signaling pathway by which many developmental processes are regulated, such as cell fate decisions, cell and tissue mechanics, ECM homeostasis, etc. It has been unraveled that Notch signaling is affected by mechanical forces in direct or indirect ways (figure 1.11) (Stassen *et al*., 2020)

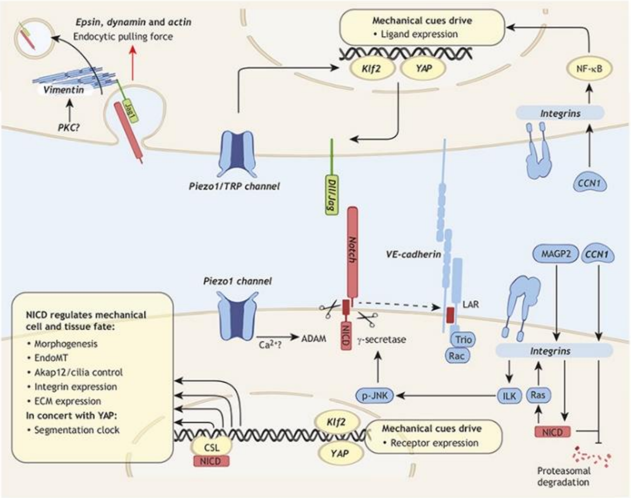

Figure 1.11: *Direct and indirect links between Notch signaling and mechanotransductive signals. Adapted from Stassen et al., 2020.*

The interaction between mechanical forces and the Notch pathway is generally indirect. Production of ligands or receptors which are mechanically regulated and the crosstalk between Notch and mechanosensors are included in this indirect relationship (figure 1.11). Although the crosstalk between YAP/TAZ and Notch in angiogenesis has been reported, the particular role of this crosstalk has still remained unknown. However, more details about the interaction of mechanical cues with Notch pathways in other tissues have been reported. For instance, during myogenesis, YAP translocation to the nucleus is triggered by contractions which result in the expression of Jag2 and subsequent Notch activation. This activation is related to the preservation of the progenitor pool required for regeneration. One of the main mechanosensor integrins also interacts with Notch both in direct and indirect ways (figure 1.11). Like a feedback loop, Notch signaling also affects integrin activation via both transcriptional and non-transcriptional mechanisms. One of the most striking examples of crosstalk between Notch and mechanotransductive cues is observed in endothelial cells during development. This crosstalk is crucial for the proper heart development in zebrafish in which transcription of *notch1b* in the endocardium is promoted by heart contraction and subsequent blood flow.

Another influence of Notch on tissue mechanics is through modulation of ECM expression in various tissue, involving cartilage, skin, and heart. For example, in the endocardium, ECM production is modulated by Notch ligand Jag1 while another Notch ligand Dll4 is responsible for cell adhesion (Stassen *et al*., 2020).

The crosstalk between Notch signaling and mechanical cues are also observed in cell fate decisions. For example, in a study by Totaro and colleagues (2017) reported that mechanosensation-dependent modulation of Notch signaling dictates a critical stem cell fate decision: to remain undifferentiated or to go through differentiation through mechanotransduction-dependent YAP/TAZ regulation. Activation of YAP/TAZ by mechanotransductive signal induces epidermal stemness via suppression of Notch signaling. On the contrary, if YAP/TAZ activation is prevented by mechanical forces, in turn, Notch signaling is activated and results in loss of stem cell characteristics (Totaro *et al*., 2017)

To conclude, the transmission of mechanical cues into biochemical signals requires extensive crosstalk between different signaling pathways whose exact mechanism has still remained unknown. Understanding mechanosensing mechanisms might be utilized for the manipulation of them for the desired outcomes in different research areas and clinics. Because when there is an aberration in any step of mechanosensation, the ultimate result is different kinds of diseases from developmental disorders to cancer. Therefore it is important to solve the puzzle behind how cells sense environmental signals and translate them into biochemical signals. What can be concluded from extensive research findings in the literature is that mechanotransduction is not just feeling or sensing the biophysical cues by the cells but also about discovering, understanding and influencing. So, it is easy to misinterpret the response of the cells to mechanical cues, without understanding how this response affects other signaling pathways in the cell. Therefore, we can say that mechanotransduction research is still in its infancy stage which requires extensive studies for clinical applications.

1.2.5 Topography-induced Mechanotransduction: Effects of topography on cell behavior

Up to date, microscale topographies that are used in the literature have aimed to observe their effects on cell adhesion and morphology. Generally, microscale grooves are one of the most common topographies to control different cell behaviors. The materials that are used for fabrication are quartz, silicon, titanium-coated silicon, hydroxyapatite (HA)-coated silicon, poly (methyl methacrylate) (PMMA), poly-L-lactic (PLA), polystyrene (PS), polycarbonate, poly(glycerol-sebacate) (PGS), olefin copolymers, and silicone/PDMS. In the literature, the majority of the cells show alignment with the grooves and cytoskeletal elements such as actin fibers and microtubules also show parallel alignment with the grooves (Nikkhah *et al.*, 2012).

For example, one of the early studies by Oakley and Brunette (1993; 1997) showed that human gingival fibroblasts aligned with the 1-30 μm wide grooves on titanium substrate. In a recent study, endothelial cells showed alignment along the grooves, and alignment increased on deeper grooves in which grooves are created with nanoimprint lithography in olefin copolymers (Oakley & Brunette, 1993; Oakley *et al.*, 1997).

Microtopographies are widely used in neuronal research to direct neurite growth and extension. Especially microgrooves at various heights (2.5-69 μm), widths (5-350 μm), and spacings (20-60 μm) are preferred for this purpose. It is observed that neurite alignment is more significant in deeper, narrower, and less spaced apart microgrooves. Coating these topographies with biomolecules such as laminin or nerve growth factor induces a higher degree of neurite extension. For example, in the work of Kang *et al.*, embryonic neurons showed more neurite extension when they are cultured on laminin-coated grooved fibers (Nikkhah *et al.*, 2012).

Nano- or micro-topographic features are also used to study the mechanotransduction effects on the self-renewal and differentiation of stem cells. For instance, mesenchymal stem cells (MSCs) show increased focal adhesion size and upregulation of osteogenic differentiation markers (e.g. osteopontin, OPN), when seeded on nanoscale-sized pits where pits order is slightly random. However, in a recent study, it is observed that self-renewal and prolonged growth as multipotent stem cells are observed in MSCs when they are seeded onto ordered nanopits. This approves the correlation with the decrease in focal adhesion size, indicating that for self-renewal, an intermediate level of cellular tension is required in contrast to adipogenic and osteogenic differentiation, in which a lower and a higher level of cellular tension is required, respectively (McMurray *et al.*, 2014).

In another study, neural stem/progenitor cells (NSPC) are cultured on a substrate with micropatterned topographies (1.5 μm terrace width, 1.5 μm groove width, 625 nm groove depth) (figure 1.12) on which there are 10 nm nanopores on the surface of the grooves, and neuronal differentiation and upregulation of focal adhesion proteins are observed compared to nonpatterned/flat substrate (Wilems *et al.*, 2019).

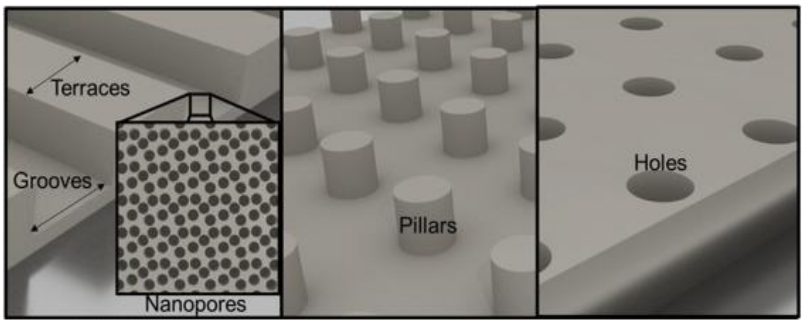

Figure 1.12: *Representational images of common micropatterned surfaces. Adapted from Wilems et al., 2019.*

There are different microtopographies in the literature that can be designed to mimic the natural topographies in the body, from cardiac tissue to neural tissue topographies (figure 1.13).

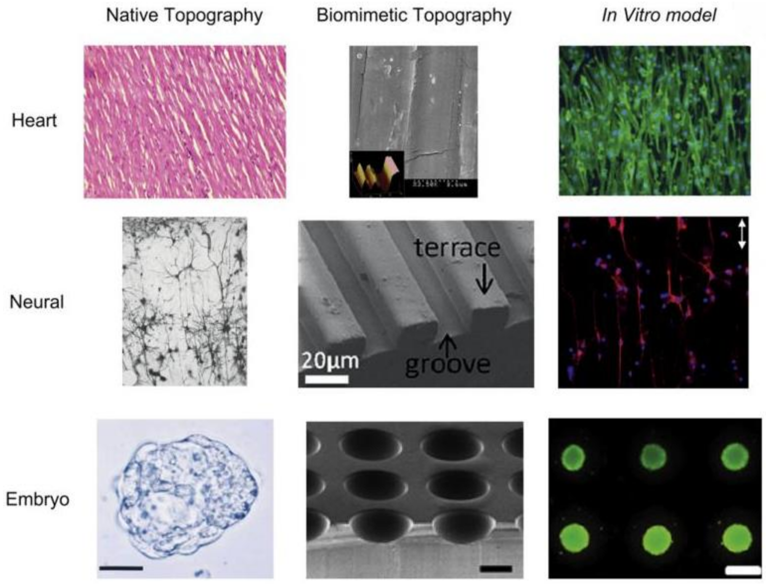

Figure 1.13: *Different fabricated microtopographies in vitro to mimic in vivo embryo, neural, and cardiac tissue structures. Adapted from Nikkhah et al., 2012.*

In addition to morphological effects such as alignment of cells, focal adhesion size changes, etc., nano- and/or microtopographies have critical roles in the neuronal program by affecting gene/protein expression levels. The extracellular matrix (ECM) of the central nervous system (CNS) is significantly different from the ECM of other organs and tissues in terms of its mechanics, structure, and composition. Although regional mechanical heterogeneity is found in the brain and spinal cord compartments, the CNS has relative softness compared to other tissues. In this regard, alterations in mechanical properties of the human brain in neurodegenerative diseases (e.g. in multiple sclerosis, amyotrophic lateral sclerosis, and Alzheimer's disease) and brain cancer is observed. Moreover, it is known that ECM organization and integrin-mediated mechanosensing have different roles in the control of neuronal cell development and functioning at all stages. (Chighizola *et al*., 2019).

In one study, human embryonic stem cells (hESCs) were cultured on the 350-nm ridge/groove pattern and cells on the flat surface, and cells without any surface or pattern were used as control. Cells that are on the nanoscale patterns show alignment in the direction of the ridge/groove patterns, and the ones on the flat surface show random alignment. They analyzed gene expression using RT-PCR. The neuronal differentiation marker NeuroD1 shows upregulation in hESCs seeded on the 350-nm ridge/groove patterns compared to flat surface control and control cells without surface. Furthermore, the endoderm gene marker GATA6 and the mesoderm marker DCN expression level decreased in the hESCs on the 350-nm ridge/groove pattern compared to flat surface control and control cells without surface (Lee *et al.*, 2010). Neuron/microenvironment relations with mechanotransductive signaling are not limited to only one type of topographical feature or one type of cell. There are different studies in the literature in which different topographical patterns in various sizes and diameters are used. For example, polyurethane acrylate (PUA) substrate on which nanoscale ridge/groove and pillar patterns are structured in which pillar gap ranges from 300 to 1500 nm (Yang *et al.*, 2013). Human neural stem cells (hNSCs) were seeded on these nanopatterns. According to qRT-PCR results, neural differentiation marker Tuj1 expression shows an inverse relation with the groove sizes. That is, Tuj1 expression is upregulated on the nanopatterned surfaces with small grooves (300 and 600 nm). Immunofluorescent staining for the astrocyte marker GFAP shows that GFAP expression is higher on the majority of the nanopatterned surfaces compared to control surfaces, and its expression decreases as the groove size increases. Also, the expression of two focal adhesion proteins, which are vinculin and FAK are measured. It is observed that both vinculin and FAK expression levels are upregulated on the majority of groove and pillar surfaces, especially on small groove and pillar sizes. Consistent with the previous findings in the literature, cells' alignment with specific nano- and/or microtopographies is a common response of the cells to the extracellular mechanical signal.

Yang *et al.* (2014) used four types of substrates: flat substrate (FS), nanopore patterned substrate (NPS), microgroove patterned substrate (MPS), and hierarchically patterned substrate (HPS) consisting of both microgroove and nanopore patterns. Human neural stem cells (hNSCs) cultured on HPS substrate show higher vinculin expression compared to the other three control groups. Also, integrin β1 and neural cell adhesion molecule (NCAM) colocalization is significantly increased in hNSCs compared to control groups. Immunocytochemical staining of neuronal markers Tuj1 and MAP2, and astrocyte marker GFAP shows that Tuj1-positive neurites, MAP2-positive cell bodies, and GFAP-positive intermediate filaments align with microgroove patterns on the MPS and HPS substrates. More mature and longer neurite outgrowth is observed in hNSCs cultured on HPS substrate compared to control groups. qRT-PCR results confirmed that Tuj1, MAP2, and GFAP expression levels were significantly upregulated in hNSCs seeded on HPS substrates compared to hNSCs grown on other control substrate groups (Yang *et al.*, 2014).

Studies about the activation of different signaling pathways by topography-induced mechanotransductive signals are also available in the literature.

In work by Vermuelen *et al.* (2020), TGF-β signaling is affected by microtopographies and results in the upregulation of differentiation markers SCX, SOX9, and α-SMA in mesenchymal stem cells (MSC), suggesting that TGF-β signaling might be positively regulated with mechanotransduction-induced signals (Vermeulen *et al.*, 2020).

In a different study, the effects of micro or/and nano topography on N-cadherin expression and β-catenin signaling activation of osteoblasts on titanium (Ti) surfaces. They compared the micro- and/or nanotopographies with naïve and N-cadherin down-regulating Mouse osteoblastic MC3T3-E1 cells. According to the results, N-cadherin expression was significantly upregulated on nanotopography resulting in decreased β-catenin signaling activity, and as a result, a decrease in osteoblast differentiation was observed. In contrast, microtopography results in a decrease in N-cadherin expression, upregulated β-catenin signaling activity, and an increase in osteoblast differentiation on all Ti surfaces. The study, for the first time, clarifies that N-cadherin/β-catenin interaction is modulated by micro/nanotopography-induced mechanotransduction (Liu *et al*., 2014).

For proper organismal development and maintenance of tissue homeostasis, all cells sense and integrate mechanical and biochemical signals from the environment. The evolutionarily conserved process, mechanotransduction involves the translation of mechanical signals into biochemical signals, which influence cell differentiation, survival, proliferation, and cell migration. If these signals are abnormal or misinterpreted by the cells, the disease state develops. In recent years, aberrations in the brain ECM architecture and mechanotransduction process are reported to contribute to various neurodegenerative diseases such as multiple sclerosis, amyotrophic lateral sclerosis, and Alzheimer's disease and neurodevelopmental disorders such as autism spectrum disorders and schizophrenia, or to brain cancers. Consistently, mechanotransductive signaling-related aberrations are not observed only in nervous system-related diseases but also in various disease states such as cardiovascular disease, fibrosis, and cancer in which cell and tissue mechanics are dysregulated (Barnes *et al*., 2017; Chighizola *et al*., 2019).

In conclusion, it is important to elucidate how the cells sense and integrate mechanical signals into biochemical signals to gain deeper insight into the different disease mechanisms. Moreover, knowledge of cells' response to various mechanical signals can be utilized in improving medical implants, regenerative medicine, and artificial organ studies.

The author would like to finish this section with a quotation from cell and developmental biologist Paul A. Weiss from his lecture in 1960.

> Life is a dynamic process. Logically, the elements of a process can be only elementary processes, and not elementary particles or any other static units. Cell life, accordingly, can never be defined in terms of a static inventory of compounds, however detailed, but only in terms of their interactions. (Fletcher & Mullins, 2010, p.11)

1.3 Substrate Fabrication Techniques

By using different fabrication techniques to control the nano- and/or microenvironment presented to a cell, scientists can mimic the topographical features that cells come across in the body. There are different techniques available to create nano- and/or microtopographies. These techniques can be grouped into two main categories: techniques that create ordered topographies and the ones that create unordered topographies. For creating ordered topographies, there are two main techniques which are Electron Beam lithography and photolithography. Polymer demixing, phase separation, and colloidal lithography are generally used to create unordered topographies. Materials that are used for fabrication are various types from quartz, silicon, and titanium to polystyrene (PS), polycarbonate, and poly(glycerol-sebacate) (PGS) (Nikkhah *et al.*, 2012; Norman & Desai, 2006).

Electron beam lithography is used to create ordered patterns by using high-energy electrons to expose an electron-sensitive resist. Although both positive and negative type resists are available, positive ones are usually preferred as negative ones cause lower feature resolution. In this technique, by controlling the beam traveling over the surface, topographical features can be created. This technique makes it possible to create surface features even with 3-5 nm dimensions (Norman & Desai, 2006).

Among the first fabrication techniques for ordered patterns is photolithography, in which a layer of a light-sensitive polymer called a photoresist is used as a spin-coat for the substrate. Then, ultraviolet light is directed to this photoresist layer. As a result, cross-linking, polymerization, or degradation is observed in the exposed material. Then, the pattern is created via different means causing a dissolution of selected areas. With this technique, two-dimensional (2D) or topography-included substrates, as well as cell-encapsulated materials, can be fabricated with different natural and synthetic polymers (Nikkhah *et al.*, 2012).

For creating unordered topographies, polymer demixing is the commonly used method in which the spontaneous phase separation of polymer blends which occurs under some conditions, is used. Although this technique is quick and inexpensive, because there is a lack of control in the fabrication of nano- and/or microtopographies, this technique is not an ideal way to create patterns to mimic the nano- and/or microscale features of the body.

Phase separation is another technique for the fabrication of unordered features. This technique does not need special equipment, and three-dimensional (3D) scaffolds can be created with fibers in the sub-micron range. A continuous fiber network can be created in five steps: polymer dissolution, phase separation and gelation, solvent extraction from the gel, freezing, and freeze drying in the water. The advantage of this technique is the easy control of pore structure and fiber diameter, which depend on the solvent and initial polymer concentration in the process. Thicker fibers and less porous networks can be obtained using high initial polymer concentration and vice versa (Norman & Desai, 2006).

In colloidal lithography, various nanostructures on planar and non-planar substrates can be created by using colloidal crystals used as masks for etching and deposition. Low-cost, high-throughput processing, large fabrication area, and various choices of materials can be counted as advantages of this technique. By playing with the microsphere diameter in the colloidal mask, feature size can be changed, and through manipulation of the crystal structure of the colloidal mask, the incidence angle of the vapor beam, and mask registry, different shapes can be obtained (Zhang & Wang, 2009).

A recent method which is ultrafast laser micro/nano-manufacturing has been started to be used commonly for micro- and nano-fabrications. As femtosecond laser is the fabrication technique used in this study, it will be discussed in detail in the next section.

1.3.1 Substrate Fabrication with Femtosecond Laser

The state-of-the-art technique, which is femtosecond (fs) laser microfabrication, has attracted attention over the past two decades because of its applicability to all materials and easy, one-step processing. While fs laser can be focused into nanometer scales (~ 10^{-9} m), it has ultrashort temporal scales (~ 10^{-15} s) and a high energy density (> 10^{14} W/cm^2). With these characteristics, femtosecond lasers can fabricate any materials with high quality and high precision.

The limitations of traditional fabrication methods are broken with the nonlinear (multiphoton, etc.) absorption of a femtosecond laser, and currently, fabrication accuracy is provided at 1/50 of the diffraction limit. Thanks to nonthermal phase transitions, zones are not affected by heat, and cracks are not observed, which improves the quality of the fabrication. Moreover, there is no special equipment required in the process, such as a mask, vacuum, or reactive gas environment (Guo *et al.*, 2020).

These advantages of femtosecond lasers paved a new way in different areas, such as in solar cell applications, or superhydrophobic surfaces created with fs can be used in anti-icing, anti-corrosion, and self-cleaning applications. In biomedical applications, cell adhesion for different cell types, drug delivery, and improvement of implants can be studied effectively (Ahmmed *et al.*, 2014).

The mechanism of laser-matter interactions is basically about the material removal (e.g., ablation) and eventually the formation of micro/nanopatterns. Femtosecond laser ablation depends on material properties, laser properties, and the machining environment. Therefore, laser-matter interactions are complex as it takes place over a short period of time. In the first step of the interaction, photons are absorbed by the electrons. For metals, linear absorption is dominant, whereas nonlinear absorption is more seen for semiconductors, dielectrics, and insulators. A Diagram of the four major steps of this interaction can be found in figure 1.14 below (Ahmmed *et al.*, 2014).

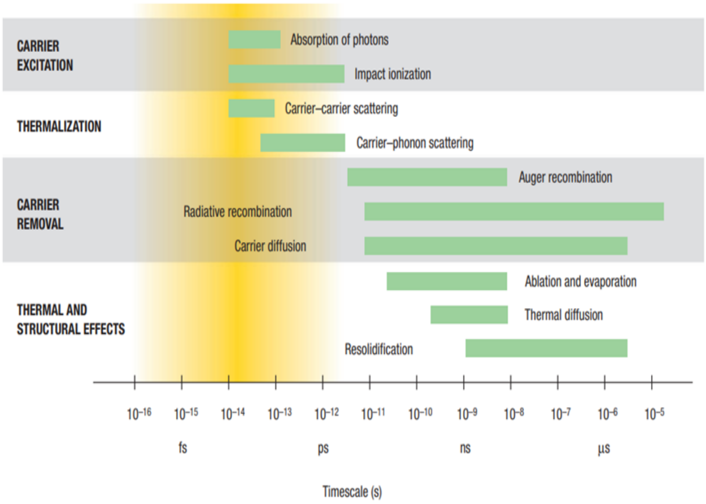

Figure 1.14: *Timescales of events in the material as a result of laser-structuring. Adapted from Sundaram, & Mazur, 2002.*

In the first step, which is carrier excitation, the carriers in the material absorb irradiation. Absorbed optical energy that is transferred to the carriers on the material is redistributed through carrier-carrier or carrier-phonon scattering in the thermalization step. In carrier-carrier scattering, there is an interaction of the carriers with one another until they reach a Fermi-Dirac distribution after some hundreds of femtoseconds. In contrast, in carrier-phonon scattering, there is an energy transfer to the lattice. It takes several picoseconds to occur for the carriers and the lattice to reach thermal equilibrium. That is, in this step, the same temperature for the carriers and the lattice is observed. When this thermal equilibrium occurs, excess carrier removal occurs. When the thermal equilibrium is reached and any excess carriers are removed, what happens is the formation of thermal and structural effects on the material (Mingu, 2020).

In general, laser-matter interaction occurs in three steps: laser energy is absorbed by free electrons, the absorbed energy is redistributed by thermal diffusion through electron-phonon coupling, and materials are ablated by evaporation or melt ejection. One of the laser ablation morphology which is used in this study is laser-induced periodic surface structure (LIPSS), also called ripples (Huynh & Semmar, 2014) will be discussed in later sections. In addition to LIPPS morphology, microcolumn, also used in this study, spike, and pillar morphologies can be obtained with femtosecond laser depending on processing parameters. An example of LIPSS and the microcolumn pattern is shown in figure 1.15 below.

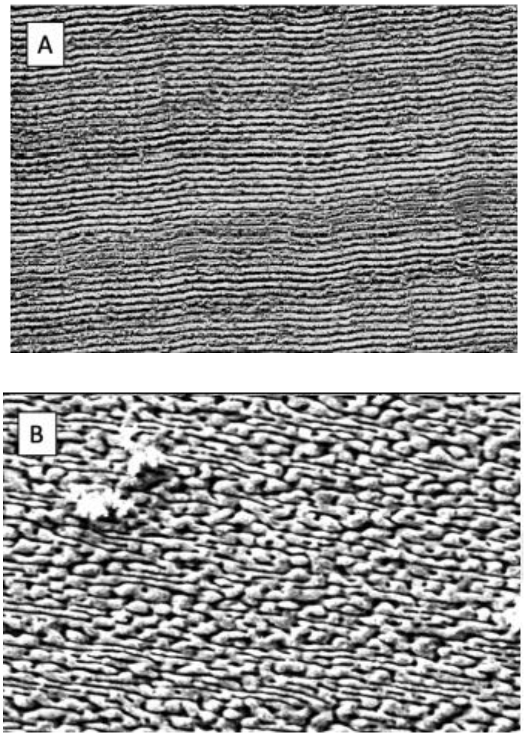

Figure 1.15: *SEM images of LIPSS (A) and microcolumn (B) pattern. All scale bars are 10 µm. Adapted from Mingu, 2020.*

In conclusion, various surface structures can be created with femtosecond laser by fine-tuning laser parameters with high quality and high precision. Thanks to these advantages, the femtosecond laser has come forward among other traditional fabrication methods.

1.3.2 Laser properties and operation

There are different types of lasers that have various parameters critical for substrate fabrication. One of these parameters is whether the light is delivered continuously (continuous wave or CW lasers) or in pulses. The pulse duration in lasers can be even as short as femtoseconds. For fabrication purposes, in pulsed lasers, pulse length and repetition rate (in pulses/second) are critical parameters. Different components are included in the lasers used for fabrication purposes, such as motorized precision stages, Galvo heads for scanning the laser beam, additional optical elements to control the beam (mirrors, collimators, focusing lenses, amplifiers, etc.), and a power meter in addition to a software for the control of stages and scanning design (Mingu, 2020).

The properties of the femtosecond laser used in this study were shown in table 1.1 below.

Table 1.1: *Properties of a femtosecond laser used in this study*

Central wavelength	1030 nm
Repetition rate	1 MHz
Pulse duration	370 fs
Maximum power	2 W
Spot size	16 µm
Scanning velocities	Up to 3000 mm/s

By using the average power value, the energy reached in a single spot in one second can be calculated mathematically. The laser uses a raster scan on the surface of the material, and a simple raster scan was schematically described in figure 1.16.

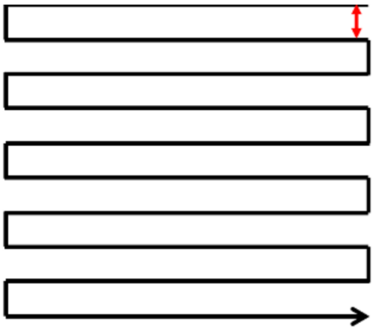

Figure 1.16: *Representational diagram of Raster scan used for laser structuring. Adapted from Mingu, 2020.*

The constant distance between each raster line is shown with a red arrow. Hatch is the name of the distance between the lines. Laser pulses delivered to a single spot are affected inversely by the laser speed. As the laser speed slows down, more pulses are sent onto a single spot. By using three different velocities, the affected area was schematically represented in figure 1.17 below (Mingu, 2020).

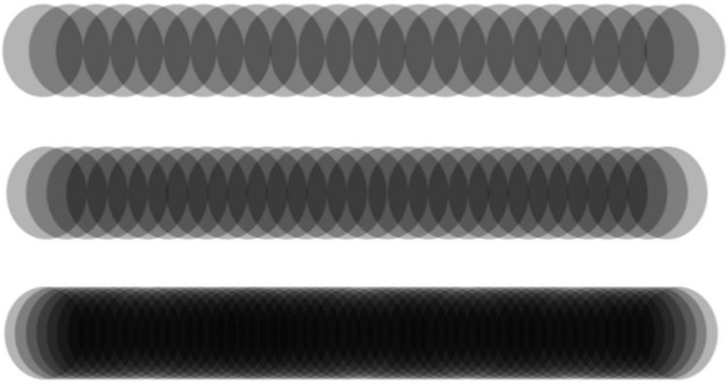

Figure 1.17: *Representational image of laser pulses with different velocities delivered to a single spot. Adapted from Mingu, 2020.*

1.3.3 Silicon and its properties

Silicon is the second most abundant element on Earth after oxygen. Silicon has an atomic number of 14 and is a semiconductor. The crystal structure of the Silicon makes it attractive for the micro- and/or nanofabrication techniques. Crystalline Silicon can be produced from its source material (sand, quartzite rock) using techniques such as Czochralski Method or Float Zone method. Phosphorus (N-doped) and Boron (P-doped) were used as silicon dopants for the fabrication of microelectronics. Wafers obtained slicing of crystalline Silicon into disks have different shapes (round or semi-squared), sizes, thickness (279 μm and 525 μm), and polishing types also differ, such as single-side polished (SSP), double-side polished (DSP), and non-polished (as-cut).

Silicon was used as a substrate because of a couple of reasons. First of all, it is easy to reach and has a low cost. Secondly, simplicity in the process of silicon fabrication with ultrafast lasers is higher compared to other traditional fabrication methods. Thirdly, any desired micro- and/or nanopatterns are easily created by adjusting laser parameters.

Although it is not commonly used in implant applications, it is widely used in some brain electrodes. Also, there are many studies in the literature in which Silicon was used as a cell culture substrate, and the effects of different silicon modifications on different cell types are reported (Mingu, 2020).

Silicon has been used in many studies in the literature, SH-SY5Y cell lines are grown on a silicon substrate with different nano- and/or microtopographies. The outgrowth of neurites was found to be higher on the fabricated substrates compared to flat/nonfabricated control substrates. However, fewer and shorter filopodia protrusions of neurites were observed on the nanotopographies than on flat and microtopograhies (Du *et al*., 2022).

Teo and colleagues used silicon as a substrate material, human mesenchymal stem cells (hMSCs) showed aligned stress fibers with the 250 nm line width nanotopographies, and also upregulation of neurogenic and myogenic differentiation markers was observed. Cellular focal adhesions were found to be significantly smaller and more elongated on nanotopographies compared to microtopographies and unstructured control (Teo *et al*., 2013).

In a different study, human aortic endothelial cells were seeded onto four different grooved silicon substrates coated with collagen for the assessment of the effect of the topography on cell adhesion, morphology, and proliferation of endothelial cells. According to the results, the number of attached cells, circularity of the cells, cell proliferation, cell spreading, number of filopodia formation, and direction of the alignment depend on the substrate topography (Fernández-Castillejo *et al*., 2017).

1.3.4 Mechanism of formation of LIPPS and Microcolumn patterns

The two mainly studied topographies, LIPPS, and microcolumn were previously described, and the mechanism of their formation, and which parameters were used for their creation are known.

The first observation of laser-induced periodic surface structuring (LIPPS), also called ripples, goes back to 1965 when LIPSS was observed on the surface of germanium and gallium arsenide by Birnbaum *et al.* (Zhang *et al*., 2022). Nonetheless, almost 50 years later, the formation of LIPSS on different materials such as metals, semiconductors, and glasses was reported (Öktem *et al*., 2013). The studies about LIPSS are continuously increasing because of its theoretical and practical implications.

The laser fluence and the number of overlapping pulses significantly affect the periodicity of the LIPSS pattern (Zhang *et al*., 2022). There are different types of LIPSS, and the classification of LIPSS based on different properties is made. For example, when it is classified according to the wavelength, there are two types which are low-spatial-frequency LIPSS (LSFL) in which periodicity is similar to the laser's wavelength; the second one is high-spatial-frequency LIPSS (HSFL) with periodicity smaller than half the laser's wavelength. LIPSS structures can be also classified based on their orientation with the polarization of the incident light (Mingu, 2020). When the structure is created perpendicular to the laser polarization, it is called "*normal* LIPSS" however, when the structure is parallel to the polarization, it is called "*anomalous* LIPSS" (Pavlov *et al*., 2017)

Generally accepted theory for the formation of LIPPS states that LIPPS ripples appear as a result of the interference of incident light with the surface plasmon polariton wave upon scattering on any surface defect such as scratches (Pavlov *et al*., 2017). Surface plasmon polaritons (SSPs) are electromagnetic fields whose propagation occurs at the interface between a metal and a dielectric. The idea that the interference of incident light with surface plasmon polaritons leads to the formation of LIPSS first introduced by Keilman and Bai (1982); on the other hand, the term LIPSS is introduced by Sipe *et al*. (1982) and the first-principle theory of its formation is developed by Sipe *et al*. (1982) (Keilman & Bai, 1982; van Driel *et al*., 1982). The term that describes the interactions of the incident light with a rough surface called an efficacy factor, η, was introduced by them, too. Although this theory is currently a widely accepted theory for the formation of LIPPS, it does not explain all types of LIPPS formation (Bonse *et al*., 2017).

The successful description of LIPSS on silicon is explained by a combination of Sipe's theory with a Drude model in which the behavior of carriers in a material system is described. In this combination theory, the importance of permittivity changes during material irradiation upon application of ultrafast laser pulses has been highlighted (Bonse *et al*., 2009).

While ablation leads to anomalous LIPSS, normal LIPSS is formed as a result of oxidation. In both instances, inhomogenous oxidation or ablation is caused when the surface waves, scattered from the surface, interfere with the incident light. For the desired LIPSS types, such as normal or anomalous LIPSS, fluence and repetition rates can be adjusted. While high fluence and low pulse number (several pulses) lead to the formation of normal LIPSS, lower fluence and higher pulse number (several thousand pulses) bring about anomalous LIPSS (Pavlov *et al*., 2017).

Various feedback mechanisms that are involved during the formation of LIPSS were reported. LIPSS formation begins with the interference effect on surface defects. While LIPSS is appearing, the altered surface topography and formed structures can act as scattering points for the next pulse (Öktem *et al*., 2013; Bonse *et al*., 2017). This feedback effect can be utilized to make large regular ripples by overlapping the irradiation spots. This feedback effect is shown in one study by Ionin and colleagues (2015). In the study, the formation of periodic, ordered ripples was observed as a result of positive sign feedback; on the contrary, negative sign feedback results in random surface roughness. It was stated that a preliminary LIPSS structure was formed after roughness was observed as a result of sign changes by the feedback function. Following more shots, feedback changes sign again, and the formation of a secondary LIPSS was observed, which is not subject to any more change (Ionin *et al.*, 2015).

LIPSS regularity is also affected by surface electromagnetic wave (SEW) propagation. The material type influence the decay length (or mean free path) of the excited SEW. For example, materials with high optical losses at the irradiation wavelength and short SEW decay lengths, such as Mo, Ti, and steel, promote the formation of regular LIPSS. However, less regular LIPSS with bifurcations and discontinuities is observed in materials with long SEW decay length because more unwanted interactions of SPP with itself or other surface irregularities occur (Gnilitskyi, 2017).

The fluences above the threshold, which causes ablation-type LIPSS at first; as the pulse number escalates, a microcolumn pattern starts to appear. After ripple formation, topographical features, which the surface acquires, alter the incidence of the laser light's angle at each point. The reflections on the different surface structures direct the light further. At the topography maxima or minima, the most absorption was observed. While the material vaporizes with escalating pulse numbers, vapor deposition is preferentially favored at the top parts of the topography and creates growing structures. The resulting structures have column-like or hill-like shape of micron-scale height, which is called microcolumn (Bonse *et al.*, 2014).

Some studies combine both LIPSS and microcolumn patterns for observation of cell behavior. For instance, in a study by Cunha *et al.* (2015), different topographies were used for human mesenchymal stem cell (hMSC) behaviors. The substrates used in the study were LIPSS, nanopillar (NP), microcolumn topography covered with LIPSS, and polished silicon. The behaviors studied were spreading, adhesion, commitment, and differentiation of hMSCs. They found that cell area and focal adhesion area were lower on laser-textured surfaces compared to polished silicon; while cell stretching was promoted by LIPSSs and microcolumn patterns, the increase in the formation of filopodia was induced by the nanopillar pattern.

Moreover, LIPSS and NP patterns were shown to enhance matrix mineralization and bone-like nodule formation compared to polished and microcolumn patterns (Cunha *et al*., 2015).

There are many different applications of femtosecond-laser structured topographies which involve different cell studies in the literature. The findings of these studies will be discussed in detail in the next section.

1.3.5 Cell behavior studies involving femtosecond laser fabrication, LIPSS, or silicon

The microenvironment in which cells interact affects various biological processes such as cell adhesion, proliferation, differentiation, migration, and apoptosis. Microfabrication techniques, such as femtosecond laser fabrication, made it possible to create topographical features at nano- and microscale, which aim to mimic the natural topographies in the body. Biomaterial bio-recognition by a cell depends on some parameters such as cell type, feature size, geometry, and physicochemical features of the substrate material (Martínez-Calderon *et al*., 2016).

In this regard, by fine-tuning some parameters such as the chemical or physical structure of a material or using a different cell type, particular control of the interaction between the cell and the material might provide new insights for the improvement of implants and prostheses, artificial organ studies, etc.

For example, in a study by Belaud and colleagues (2018), they looked at the effect of the orientation of nanometer-scale LIPSS lines and circular microgrooves with different curvature radii on the behavior of C3H10T1/2 mouse mesenchymal cells, especially on migration behavior. They found that migration is elevated on all topographies compared to a smooth sample. In addition, cells migrate inside circular grooves faster than linear ones. It was found that the orientation of the LIPSS lines (perpendicular or parallel) does not seem to affect the migration capability of the cells. In conclusion, the study did not only measure the effect of orientation of the

LIPSS lines but also microgroove curvature radius on the migration of C3H10T1/2 mouse mesenchymal stem cells (Belaud *et al*., 2018).

While it is not easy to structure polymers with laser, probably because these polymers have relatively-low glass transition temperature and melting temperature, LIPSS topography can be transferred efficiently to various polymer biomaterials. However, in a study by Yada & Terakawa (2015), LIPSS structure on a biodegradable polymer poly-L-lactic acid (PLLA) was created successfully by increasing the repetition rate of the femtosecond laser (Yada & Terakawa, 2015). As biodegradable polymers as a scaffold are a promising tool used in tissue engineering, by creating micro- and nano-topographies on biodegradable polymers, cell behaviors can be manipulated for desired purposes.

LIPSS formation on a polymer is not limited to PLLA, its formation on polystyrene was shown in a study by Wang *et al*. (2008). Rat C6 glioma cells grown on these laser-structured polystyrene films shows directional migration, and their orientation was parallel to the direction of LIPSS. This study shows that the LIPSS pattern might be a stimulus to guide the spreading and migration of cells (Wang *et al*., 2008).

Material type is another parameter that affects cell behaviors. For instance, in one study, stainless steel was fabricated by femtosecond laser to create LIPSS patterns on it and human mesenchymal stem cells (hMSCs) were grown on them. What they have found is that cells have a preference to locate themselves on nanopatterns perpendicular to the microstructures while they avoid adhering to (flat) unstructured stainless steel areas (Martínez-Calderon *et al*., 2016).

An example of the usage of LIPSS patterns for the improvement of implants in a study by Jorge-Mora *et al*. (2018) shows that LIPSS structure promotes the osteogenic properties of titanium and tantalium compared to unstructured surfaces. According to MTT and ELISA assay results, LIPSS topography increases cell metabolism and decreases inflammatory response to the material in human bone marrow mesenchymal stem cells (hBMSCs). The amount of collagen produced is higher on LIPSS topography which makes osteoblast differentiation easier. In conclusion, to increase osteoblastic response to a material, without the addition of chemical or new materials, laser fabrication of surfaces, especially periodic surfaces might be a promising and cost-effective modification (Mora *et al.*, 2018).

Because of its high specific strength, better corrosion resistance, and good biocompatibility, titanium-based materials are preferred for the improvement of implants. However, to promote compliance between the implant and the surrounding hard tissues (bones), an alloying element with a high concentration of β-stabilizer elements (β phase of titanium) should be added. The most suitable alloying elements to be added are niobium, tantalum, zirconium, and molybdenum, which do not cause any cytotoxic reaction in the cells. The aim of a study conducted by Petrović and colleagues (2019) was to show the relationships between laser-induced patterns on a titanium-zirconium multilayer thin film and their coupling effect on osteoblast cell response. They observed that mesenchymal stem cells show more cell growth and adhesion on LIPSS-structured surfaces compared to unstructured samples. Moreover, cell orientation was shown to be parallel in the direction of LIPSS lines (Petrović *et al.*, 2019).

In addition to the material type, coating of the material, feature, and geometry of the topography, cell type is another parameter that affects cell behavior when material-substrate interaction is in question.

The Brain Machine Interface area (BMI) has attracted more attention than ever last decades with the development of technology. However, these advances have been impeded because of some reasons, such as intrinsic host tissue response. To improve the functionality and biocompatibility of neuroelectrodes, different clinical studies were conducted. Moreover, it is known that the sensitivity of neurons to their physicochemical signals significantly affects neural alignment and development. In one neuroelectrode improvement study, for example, electrode surfaces were modulated with topographical signals to regulate neural cell behavior. LIPSS patterns are structured using Femto/picosecond laser on commercially available platinum-iridium (Pt/Ir) microelectrode probes. According to the results, the electrochemical properties of the electrodes are enhanced, cell alignment nurtured, and expression of multiple ion channels involved in various neuronal functions modulated on LIPSS topography. In terms of inflammatory behavior, there was no increase in pro-inflammatory response between structured surfaces and the control group according to proinflammatory cytokines, KC/ GRO, IL-6, or TNF-α, synthesis level (Kelly *et al*., 2020).

So far, studies related to topography-dependency of cell behaviors are discussed; however, material-dependent, especially the usage of silicon as a substrate for cell behavior studies, is also numerous. There are different modifications or treatments made on silicon to manipulate cell behaviors, such as oxidation of silicon in addition to the utilization of different silicon types. For instance, in one study, porous silicon (pSi) was used as a substrate with different pore diameters to observe the behaviors of human aortic endothelial cells (HAECs). The treatment of silicon with oxidation and silanization with aminopropyl triethoxysilane (APTES) were made to increase surface stability and stimulate cell adhesion and proliferation. Two different types of pore configurations were used, which are macroporous and nanoporous silicon. They found that different cellular responses are promoted depending on pore geometries in terms of cell adhesion and morphology. In the cells grown on macroporous silicon, alignment of the pseudopods of the cell along with the macropore and 2-D and 3-D migration behaviors of the cells were observed. On the contrary, filopodia branching out from the main cell body, which attaches the cell to the substrate, was observed on the nanoporous substrates. These findings might pave a way for new 3D cell culture platforms in tissue engineering and regenerative medicine applications (Formentín *et al*., 2014).

Besides the geometry and different chemical modifications, the roughness of a material is another parameter that has been investigated to measure material-dependent cell behavior. For instance, in a study by Gentile *et al*. (2010), silicon with different roughness was used as a cell substrate. In this work, four different cell lines which are A549 human lung carcinoma, human HeLa, human umbilical vein endothelial cells (HUVECs), and mouse 3T3 fibroblasts, grown on a silicon substrate with a surface roughness varying from Ra ~2 to 100 nm. According to the results, cells were more proliferated and adhered to surfaces with a moderate roughness compared to other surfaces (Gentile *et al*., 2010). This study suggests that surface roughness is another way to direct cell behaviors for desired purposes, such as the preferential proliferation of a specific cell type, which may improve the performance of implants.

More studies involving cell behavior changes related to material type, modification of the material, stiffness, and roughness of the material can be found in the literature. The conclusion from these studies is that different parameters lead to different cell responses depending on the cell type, which lets researchers create biomimetic materials for desired purposes. However, it might be obvious that while designing biomimetic materials to guide cell behaviors, it might be useful to take into consideration all parameters that affect cell behavior.

1.4 Surface Characterization Techniques

Surface characterization techniques are a powerful way to investigate the material used in the study. Recently, different analytical techniques have been developed that measure the characteristics of the material down to the nanoscale. Material characterization techniques classification can be made based on analysis of surface structure, physical, electrical, chemical properties, etc. An example of material characterization techniques includes optical microscopy, scanning electron microscopy, tunneling electron microscopy, atomic force microscopy, X-ray photoelectron spectroscopy, Fourier transform infrared spectroscopy, X-ray diffraction, 3D profilometry, scanning electron microscopy, Energy-dispersive X-ray spectroscopy and Raman spectroscopy (Upadhyay & Kumaraswamidhas, 2018). Every technique can be utilized for different characterization analyses. This list might go on further, and an explanation of all characterization techniques might take pages. Therefore, only the techniques, SEM, AFM, and EDS, used in this study will be discussed in detail in the next sections.

1.4.1 Scanning Electron Microscopy (SEM)

The first Scanning Electron Microscope was introduced by Mafred von Ardenne in 1937 to beat the disadvantages of transmission electron microscope, such as reducing chromatic aberrations problem. A beam of electrons that were focused on the raster is scanned using a high-resolution power. More studies were followed back by scientists and research institutions. Eventually, Cambridge Scientific Instrument Company developed a fully manufactured Scanning Electron Microscope, in 1965 and named it a Stereoscan. Since then, new modifications are made every day to develop its resolution capacity.

Unlike transmission electron microscope (TEM) which transmitted electrons are used, in SEM, emitted electrons are used to produce images. The working principle of SEM is based on applying kinetic energy to produce signals from the interactions of the electrons. To view crystallized elements and photons, secondary electrons and backscattered electrons, and diffracted backscattered electrons are used (figure 1.18). The ones used to produce an image are secondary and backscattered electrons. Secondary electrons (SE) from within a few nanometers of the sample surface have lower energy than backscattered electrons. Secondary electrons result from the inelastic interactions between the electron beam and the sample results in secondary electrons. Because they are very sensitive to surface structure, they give very useful information about topographical features. In contrast, the high-energy electrons which are backscattered electrons scattered out of the sample, and a small amount of energy is lost. Because they derive from deep within the sample, they are in close interaction with the sample. They stem from the elastic interactions between the beam and the sample (Kruit, 2010; Reimer, 1998). To detect the morphology and topography of the sample, secondary electrons emitted from the sample are used, while backscattered electrons are used to show contrast in the compositional properties of the sample. Optical components of SEM are shown in figure 1.19 below (Mokobi & Ritesh, 2022). Because the working principle of SEM is based on the interactions between electrons and matter, only conductive or semi-conductive samples can be imaged with SEM. If the sample is not conductive or semiconductive, it requires a coating with a conductive material such as gold (Au) is mostly preferred among others like silver (Ag), gold/palladium (Au/Pd), chromium (Cr), platinum (Pt), or iridium (Ir) (Goldstein *et al*., 1992).

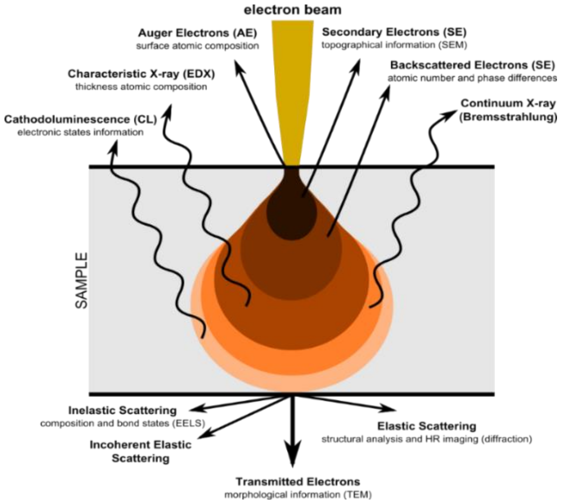

Figure 1.18: *Different types of signals produced from electron-matter interactions. Adapted from Ezzahmouly et al.,2019.*

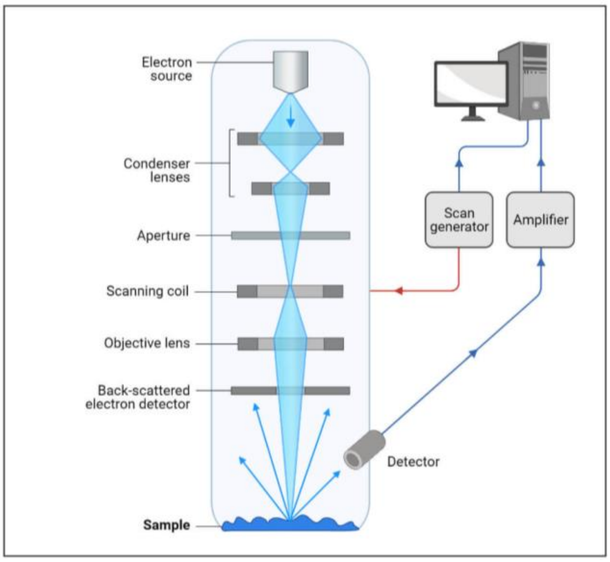

Figure 1.19: *Optical components of SEM. Adapted from Mokobi & Ritesh, 2022.*

1.4.2 Atomic Force Microscopy (AFM)

The working principle of another popular surface characterization technique which is atomic force microscopy (AFM) is based on the usage of an extremely sharp tip for surface sensing. This tip scans a surface by a raster scan line by line. There are three modes of operation in AFM, which are contact mode, non-contact mode, and tapping mode. Every operation mode has different scanning ways and advantages and disadvantages.

The interaction between the cantilever/tip assembly, called a probe, and the sample is the principle of AFM. The probe of the AFM interacts with a sample in a raster scanning mode. During AFM tip scans a surface in an up/down and side to side motion through a laser beam reflected off the cantilever. One of the AFM components, which is a position-sensitive photo-detector (PSPD), tracks this reflected laser beam and collects the vertical and lateral motion of the probe, which results in the production of the image (figure 1.20) (Oxford Instruments, 2022). There are two most important forces acting on the cantilever and tip during the process, which are Van der Waals forces and electrostatic forces. Modes of operations in AFM are classified as a function of these force interactions between tip and surface, which will be discussed below.

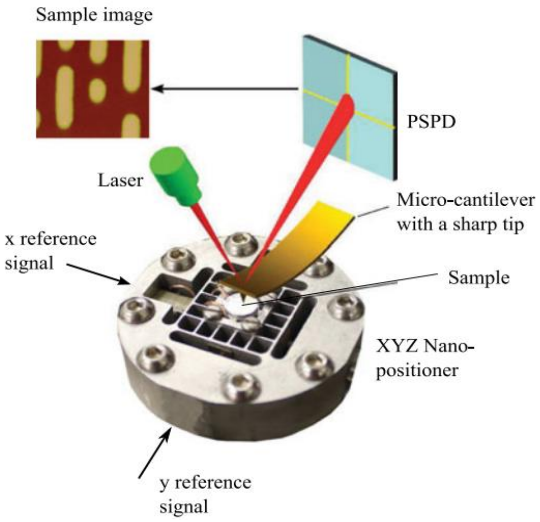

Figure 1.20: *Components of AFM. Adapted from Yong et al., 2014.*

In the contact mode of AFM, the first discovered mode, the tip is continuously in contact with the sample surface. During scanning, cantilever deflection is kept constant by a feedback mechanism. For flat and rigid surfaces such as crystals, hard polymers, and tissue, this mode is the most appropriate and provides the highest resolution. Because the tip and the sample are in contact steadily, which results in large AFM-tip sample interactions, this mode of operation is not suitable for visualization of single atoms, small molecules, or soft materials. Moreover, because the tip and the surface are always in contact, this mode can cause sample damage easily like scratch, especially on soft materials like biological samples.

To prevent this issue, a non-contact mode of operation can be preferred. In which cantilever oscillation is at a resonance frequency. When the tip is close to the surface, the oscillating probe leads to a frequency shift in the resonant frequency due to van der Waals attractive forces. As a result, both resonance frequency and oscillation amplitude produce the surface image. Since the tip is not contacting the sample surface, this mode leads to lower lateral resolution compared to the contact mode (Marrese *et al*., 2017).

For biological samples, the most proper mode is the tapping or intermittent mode, thanks to lower forces. Although the working principle is similar to the non-contact mode, this mode provides the best resolution with respect to other modes of AFM. While the tip scans over the surface, both attractive and repulsive forces are in operation. For instance, when the tip encounters a protrusion on the surface of the sample, the cantilever oscillation amplitude decreases, while the amplitude of the cantilever oscillation increases when the tip comes across a concave surface. Because the contact level is lower compared to the contact mode, the tapping mode provides higher vertical and lateral resolution. Therefore, the tapping mode is a suitable tool to gather information about surface properties, which is not possible by other AFM modes, about surface properties which makes it very attractive in the tissue engineering field (Marrese *et al*., 2017). Unlike SEM, AFM does not require conductive samples and coating therefore, there is no extra sample preparation for biological samples.

1.4.3 Energy-dispersive X-ray spectroscopy (EDS or EDX)

In Energy dispersive X-ray spectroscopy (EDS or EDX), characteristics of X-rays induced by electron beam radiation are collected to map the elemental composition of a sample. By using EDS, cellular components can be analyzed by looking at the composition of carbon, oxygen, nitrogen, phosphorus, and sulfur (Pirozzi *et al*., 2021). The X-rays are created based on the characteristics and nature of the elements in the sample. Therefore, EDS both provides semi-quantitative and semi-qualitative analysis. The basic components of EDS are composed of three parts which are an X-ray detector, a pulse processor to calculate the voltage regarding X-ray energies, and a computer system (Tekade *et al*., 2019).

EDS does not provide only chemical elements present in the sample (qualitative analysis), but also it provides an approximate elemental concentration in the sample (quantitative analysis). The intensities of the peaks indicate the concentration of the specific element in the sample. Because the unique atomic structure of each element gives unique peaks in the electromagnetic emission spectrum, thanks to both quantitative and qualitative analysis, EDS provides the chemical composition of a sample like a chemical fingerprint (Nasrollahzadeh *et al*., 2019).

1.5 Structural characterization of cells with confocal fluorescence microscopy

1.5.1 Confocal fluorescence microscopy principle

With the ability to resolve deep details within samples with high resolution and enable 3D constructions of imaged samples, confocal microscopy is a useful technique for the structural characterization of a cell. The working principle of confocal microscopy is based on the usage of fluorescence optics. In confocal microscopy, the whole sample is not illuminated at once. Instead, a defined spot on a sample is illuminated with the laser light (figure 1.21). In this way, the emission of fluorescent light originated exactly at this defined spot. Fluorescence signals coming from out-of-focus points are prevented by a pinhole, thus enabling the collection of fluorescent signals from the illuminated spot only. The numerical aperture (NA) of the objective lens, sample properties, and the wavelength of the light are additional parameters that affect resolution in light microscopy. The axial resolution in confocal microscopy is enhanced with the lower pinhole size. Although in theory, the best resolution is ~ 0.2 µm laterally and ~ 0.6 µm axially, this has not been always achieved in practice. Lateral and axial resolution equations are shown below in which resolution is nominated as R, the emission light wavelength as λ, the refractive index of the mounting medium (speed of light propagation through the material) as η, and the objective's numerical aperture as NA (Elliott, 2019).

Equation 1.1:

$$\mathrm{R}(lateral) = \frac{0.4\,\lambda}{NA}$$

Equation 1.2:

$$R(axial) = \frac{1.4\,\lambda\,\eta}{NA^2}$$

The light is focused onto a sample by an objective lens, and a second objective lens at a second pinhole focuses that light passes through it. Two pinholes have the same focus, which gave the name "confocal". A low noise photomultiplier catches any light that passes through the second pinhole and creates a signal directly proportional to the brightness of the light. The second pinhole blocks any out-of-focus signal coming from the photomultiplier. In modern confocal microscopes, the image is captured with a digital charge-coupled device (CCD) camera and visualized through a proper software system (Paddock, 2000).

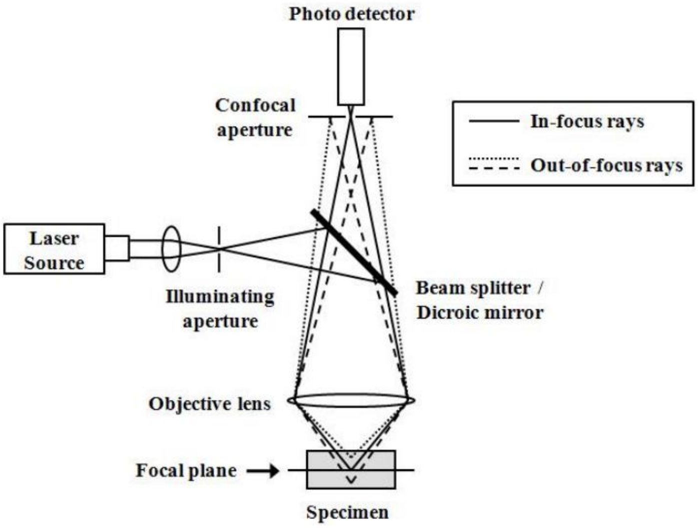

Figure 1.21: *Principle of confocal fluorescence microscopy. Adapted from Ahn et al., 2007.*

1.6 Aim of the thesis

This study aims to observe the topography-induced mechanotransduction effects on the focal adhesion gene and protein expression levels in Neuro-2a cells and the morphological effects induced by femtosecond-structured nano- and micro topographies in these cells.

Until the study of Mingu (2020), N2a cells have not been studied on silicon substrates fabricated with femtosecond lasers. In the work of Mingu, the behaviors and responses of N2a cells grown on femtosecond fabricated silicon substrates were studied. As a continuation of the previous work from our lab, this study aims to measure the effects of topography-induced mechanotransduction at the gene and protein levels in Neuro-2a cells.

CHAPTER 2

MATERIALS AND METHODS

2.1 Substrate preparation and fabrication

2.1.1 Silicon wafer, handling, and preparation for fabrication

In the study, single side polished (SSP), czochralski (CZ) growth type-produced, n-type, and thickness of 525 μm silicon wafers were used. Wafer cutting sizes were determined depending on the experiments. The silicon wafers were provided by METU GÜNAM (Center for Solar Energy Research and Applications). For cell culture experiments and AFM experiments, wafers were cut into 1 x 1cm, and for Confocal and SEM imaging wafers were cut into squares of 1.5 x 1.5 cm. Laser cutting was done in the METU Physics department with Eo Technics Supermark GF laser. The substrates were kept in a closed container until further experiments.

2.1.2 Femtosecond laser fabrication of silicon substrates

A homemade ultrafast laser was used for laser fabrication at air and room temperature. Safety rules of Class 4 lasers were followed. The central wavelength of the laser was 1030 nm with a 370 femtoseconds pulse length, 1 MHz repetition rate, and 2 W maximum power. The spot size of the focused beam was 16 μm. A schematic representation of the laser setup is shown in figure 2.1.

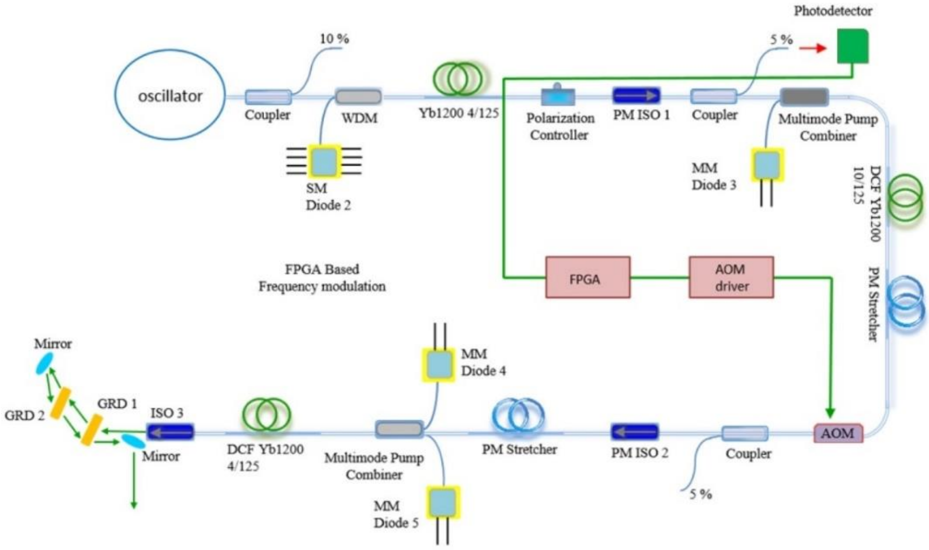

Figure 2.1: *Schematic representation of the ultra-fast laser used in this study. Adapted from Pavlov et al., 2013.*

The laser component can be summarized as a precision motion stage for stage control, a Galvo head for beam scanning, and a half-wave plate for polarization control. A picture of this setup is shown in figure 2.2. The beam, before being focused on the sample placed on the 3D stage passes through the various optical elements. For the control of polarization, the polarizer shown in figure 2.2 were used. The power meter in the figure was used for the adjustment of the power. The system was operated using ScanLab software. The advantage of the software was that it allowed the full design of structuring in a short time. The shape of the topography used in this study comprised of lines (figure 2.3) drawn, and after that dimensions were entered into the software. After that, raster scan mode was selected. The scan velocity of the laser and the hatch value were also entered into the software. For all topographies, the hatch value used was 4 µm. When all the parameters were ready, the silicon substrates were put onto the stage using tweezers, and the manual focus position of the beam was fine-tuned. When the focus is found, the structuring was carried out according to the determined parameters. For each substrate, at least five replicas were made. Images of created substrates are shown in figure 2.4 below.

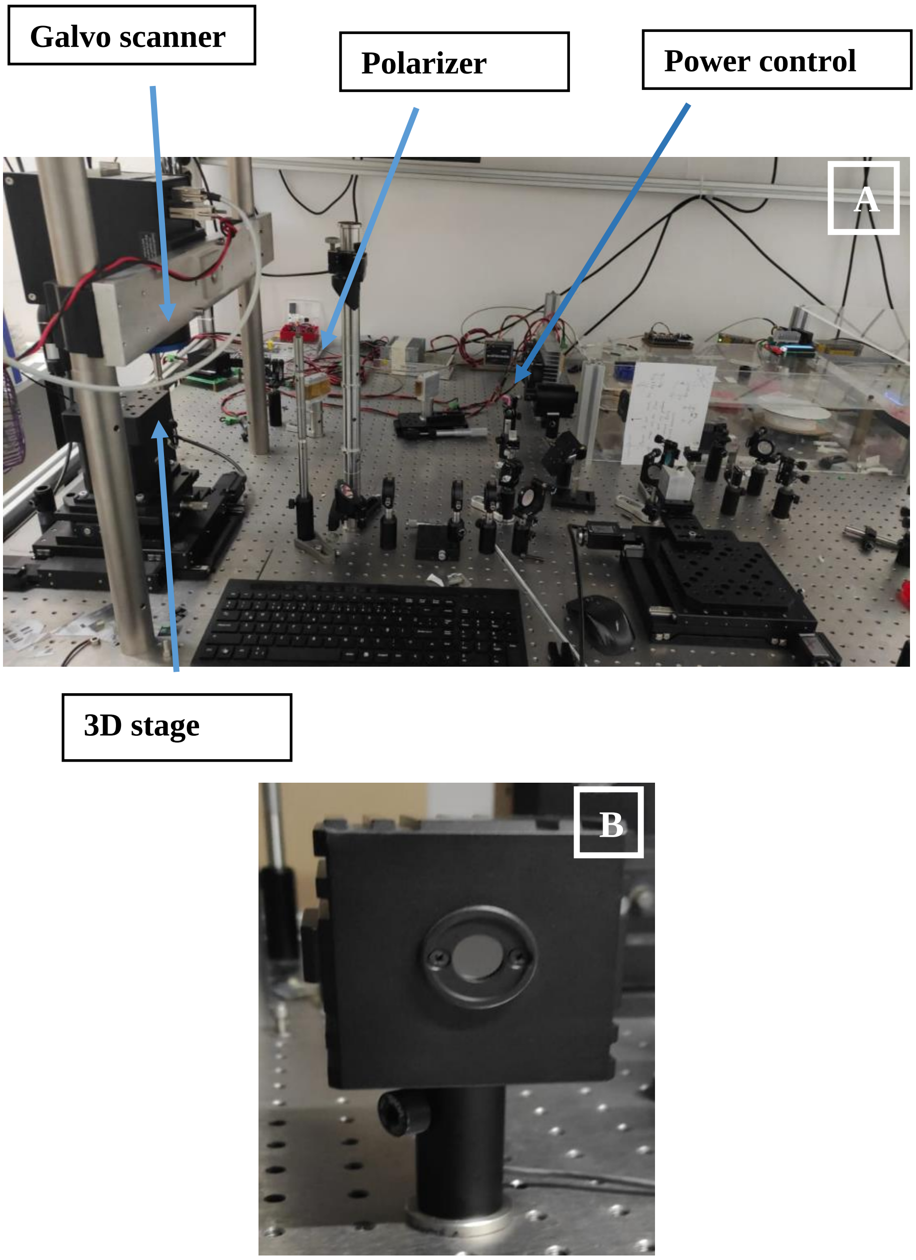

Figure 2.2: (A) *A picture of the laser and the structuring setup showing the Galvo scanner, 3D stage, polarizer, power control, and other optical elements, (B) power meter for controlling the power of the laser*

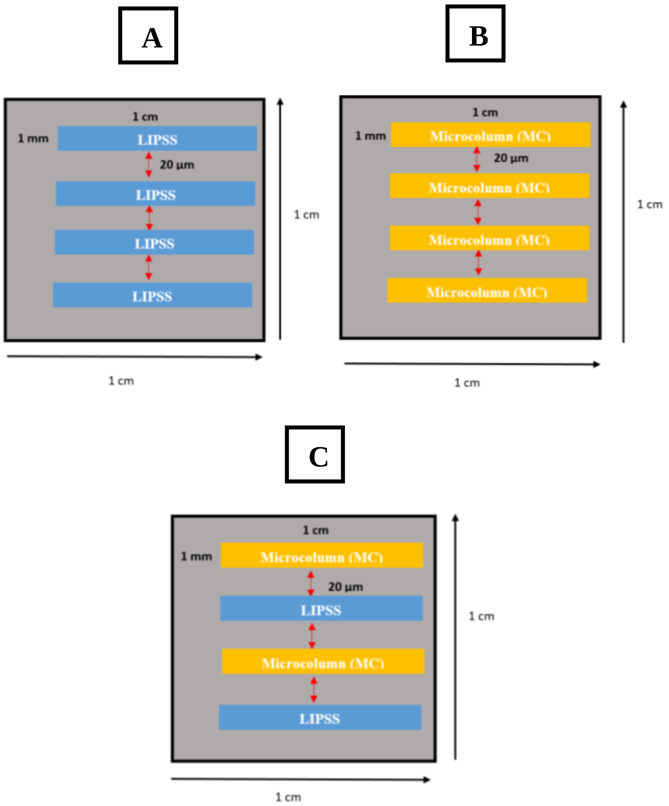

Figure 2.3: *Schematic representation of nano- and microtopographies structured by femtosecond laser on silicon substrates.*

(A) LIPSS topography; (B): Microcolumn topography; and (C): Combined topography

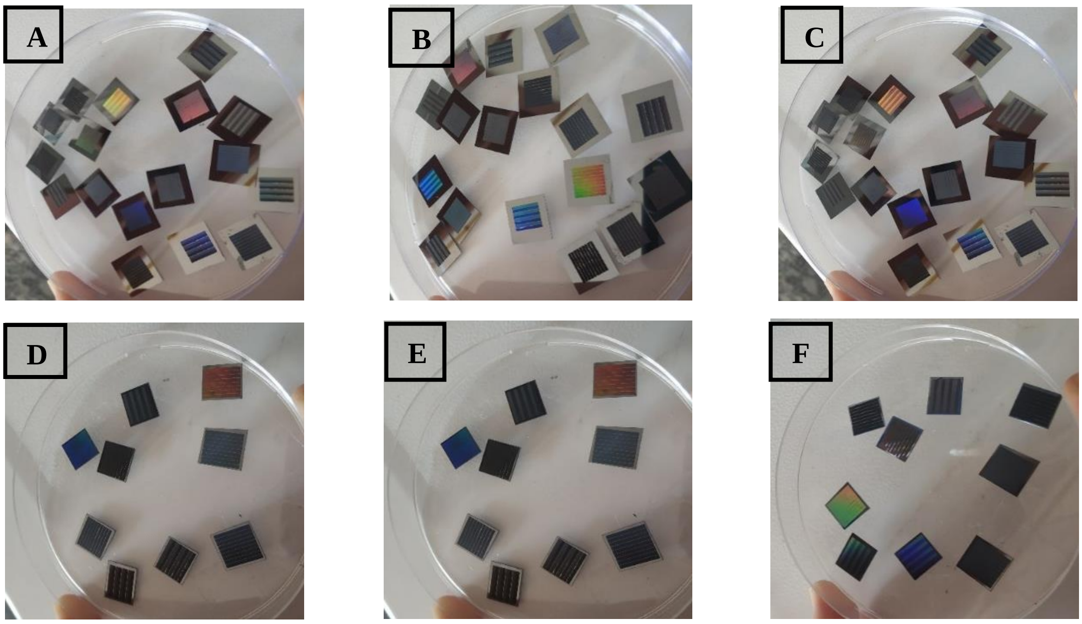

Figure 2.4: *Images of silicon substrates with different sizes and different topographies.*

A-C : 1.5 x 1.5 cm silicon substrates; D-F : 1 x 1 cm silicon substrates

2.1.3 Substrate cleaning

After laser structuring, for substrate cleaning, three different solvents, generally used in the cleaning processes, acetone, absolute ethanol, and isopropanol, were used. Each substrate was washed with every solvent for 30 minutes, and after that, they were exposed to Ultraviolet light (UV) in the laminar flow hood for 15 minutes. After that, all substrates were kept inside until further experiments. The solvent used or UV light was observed not to disrupt the substrate or the topographies on them. One of the substrate replicas was spared for substrate characterization experiments, while others were stored in closed containers in the laminar flow hood for further experiments.

2.1.4 Surface characterization

Atomic Force Microscopy experiments were carried out in METU Central laboratory. For AFM experiments, the Veeco Multimode V model of the AFM instrument was used, and the specifications of the AFM instrument as outlined below. Specifications of AFM parameters used in this study that tapping mode was used for characterization, and the size of the area analyzed is 10-1 µm.

Table 2.1: *Specifications of Veeco Multimode V model of AFM instrument located in the METU Central Laboratory*

Model	Scanning Area	Vertical Analysis Area
AS-12 ("E")	10µm x 10µm	2,5µm
AS-130 ("J")	125µm x 125µm	5,0µm

Scanning Electron Microscopy experiments were carried out both in the METU Central laboratory and in the METU Physics department. For SEM experiments, coating of substrates with a conductive material, 3 nm of gold/palladium (Au/Pd), was made in METU Central laboratory, and imaging was carried out in the METU Physics department using a Zeiss Evo HD 15 SEM instrument and in METU Central laboratory using Quanta 400F Field Emission SEM instrument.

2.2 Mammalian cell culture

2.2.1 Maintenance of Mouse Neuroblastoma Neuro2a (N2a) Cell Line

Maintenance of the neuro-2a (N2A) neuroblastoma cells, supplied from ATCC, was carried out in a T25 flask containing Dulbecco's Modified Eagle Medium (DMEM, Gibco, Cat no: 41966029) supplemented with 10% Fetal Bovine Serum (FBS, Gibco, Cat no: 10500064), and 1% Penicillin/Streptomycin (Gibco, Cat no: 15140122) as an antibiotic. The conditions of the cell culture incubator in which the flask with the cells was maintained at 37°C and 5% CO_2. For N2A cells to reach a confluency of 80%-90% requires approximately 70 hours, therefore, passage of the N2A cells was carried out twice a week. All cell culture procedures were carried out in sterile conditions in the laminar flow hood. The passage procedure of N2A cells was as follows: first, the cell medium was gently aspirated, and then pre-warmed 1X PBS was used to wash the N2A cells. Following the washing step, for the dissociation of the cells from the flask, 500 µL TrypLE (Gibco, Cat no: 12605028) was used and incubated for 5 minutes in the cell culture incubator at 37°C and 5% CO_2. When the time was up, the flask with N2A cells was taken back into the laminar flow hood, and to stop trypsinization, 8 ml new medium was added. Cells were gently mixed and collected into a 15 ml falcon tube. Then, the falcon with the cells was centrifuged at 800 rpm for 7 minutes to remove TrypLE. When the centrifuge was done, the supernatant was aspirated, and the cell pellet was resuspended in a 1 ml complete medium, and 10 µL cells from the old flask were counted using 4x4 squares hemocytometer under the light microscope (10X). After the counting, the average of the four areas was taken and calculated by multiplying by 10.000 as shown in the equation below:

Equation 2.1

$$\boldsymbol{Number\ of\ cells/mL = \frac{number\ of\ total\ counted\ N2A\ cells}{4} \times 10^4}$$

2.2.1.1 Cell growth media

Preparation of growth media of N2A was as follows: Dulbecco’s Modified Eagle Medium DMEM including high glucose with L-glutamine, 10% of the media is Fetal Bovine Serum, and 1% of the media is Penicillin/Streptomycin solution. All ingredients are mixed in a laminar flow hood and filtered with a 500 ml bottle vacuum filtration with a 0.22 µm pore size (Nest, Cat no: 343001). The prepared media was stored at +4° C.

2.3 Bacteria culture

2.3.1 The strain of Bacteria and Bacterial Growth Media

Transformation of bacteria was performed by using Escherichia coli (E.coli) XL1-Blue strain. Lysogeny Broth (LB) solution was prepared for bacterial growth culture media and sterilized by autoclaving for 20 minutes with a 120 ºC program in a Nüve OT 40L autoclave machine. For an antibiotic selection of bacteria, ampicillin (100 ug/ml) was used. For bacterial transformation, LB agar plates with bacteria cells are incubated at 37 ºC for 16 hours in the ZHWY-200B incubator by Zhicheng Instruments. After bacterial transformation, bacterial colonies are selected from LB agar plates using liquid LB solution and incubated in the ZHWY-200B by Zhicheng Instruments rotary shaker at 200 rpm for 16 hours at 37 ºC.

2.4 Cloning

2.4.1 Preparation of Competent E. coli Cells by Rubidium Chloride Method

For the preparation of competent E.coli XL1-Blue cells, streaking of cells on an antibiotic-free LB agar plate was done, and incubation was performed at 37 ºC for 16 hours. Following the incubation period, a single colony which is picked was inoculated with 2 ml antibiotic-free liquid LB media. Incubation of the growth tube was performed in a rotary shaker at 37 ºC, 200 rpm for 16 hours. Inoculation of the grown culture was carried out in antibiotic-free LB culture media, including 20 mM MgSO4 with a 1:100 (v:v) ratio. This inoculated flask was incubated in the shaker at 37 ºC, 200 rpm till its OD 600 reached 0.4-0.6 value. When the OD of the subculture reached to 0.4-0.6 at 600 nm, the subculture was divided into 50 ml falcons and centrifuged at 4000 rpm at 4 ºC for 5 minutes. Following centrifugation, the supernatant was thrown away, and the pellet was dissolved in 20 ml TFB1 solution and then 5 minutes of incubation on ice was followed. Then, the pellet which is dissolved in TFB1 solution was centrifuged at 2000 rpm 4 ºC for 5 minutes. While the supernatant was discarded, 2 ml of TFB2 solution was used to dissolve the pellet. The falcons were incubated on ice for 45 minutes. When the incubation was done, 50 µl aliquots of the cells were distributed into 1.5 ml Eppendorf tubes and quickly put into liquid nitrogen. The competent cells were stored at -80ºC. Recipes of the solutions TFB1 and TFB2 were given in Appendix C.

2.4.2 Cloning of LifeAct-EGFP constructs

Cells were transfected with fluorescent proteins to make them visible under the inverted microscope because of the opacity of the silicon substrates. The actin marker LifeAct-EGFP was used for the visualization of F-actin. This construct was prepared by Sara Mingu Akmete, our graduate student, by using standard molecular cloning techniques. From her construct, more copies of LifeAct-EGFP constructs were made with standard cloning techniques starting from the transformation of bacterial cells with LifeAct-EGFP plasmid.

Transformation of competent E.coli cells with LifeAct-EGFP construct was performed by using a heat shock method on the bench under aseptic conditions. After competent cells were taken out from the -80 ºC freezer, they were thawed on ice for 10 minutes. 5 µL LifeAct-EGFP constructs were added to the competent cells and incubated on ice for 30 minutes. Following incubation, cells were heat blocked at 42 ºC for 45 seconds, and then incubation on ice for 5 minutes was performed. When the incubation was done, to complete the volume to 1 ml, LB was added. After, cells were grown at 37 ºC for 1 hour with constant shaking. After 1 hour, the grown cells were centrifuged at 6000 rpm for 3 minutes, and 800 µL of the supernatant was discarded. In the remaining 200 µL LB, the cell pellet was resuspended, and inoculation was done on the selective agar media (with Ampicillin) using glass beads. Incubation of agar plates was carried out overnight (16 hours) at 37 ºC. Selection of single colonies from the agar plates was done the next day, and 4 mL selective liquid media (LB with Ampicillin were used for the inoculation in blood tubes. The liquid cultures in the blood tubes were grown overnight (16 hours) at 37 ºC in constant agitation. Following incubation, plasmids were isolated using GeneJet Plasmid Miniprep Kit (Thermo, Cat no: K0503) following the manufacturer’s instructions. Quantification and purity of plasmid DNAs were done using Nanodrop.

2.4.3 Transfection of cells with LifeAct-EGFP Fluorescent constructs

A turbofect transfection reagent (Thermo, Cat no: R0531) was used for the transient transfections of cells with LifeAct-EGFP constructs according to the manufacturer's instructions. Transfection of cells is carried out in 35 mm x 10 mm TC- treated plastic cell culture dishes (Corning, Cat no: 430165) which are made up of polystyrene. For each dish, 200 ul OptiMEM I (1X) (Gibco, Cat no: 31985070) was used. Into 200 ml OptiMEM, 500 ng DNA was added, and 1 ul per 500 ng DNA was added. This mixture was incubated in the laminar flow hood for 30 minutes. After incubation, cells were washed once with 1X PBS, and 800 µL OptiMEM was added to each dish. After that, 200 ul of the DNA-containing mixture was added to each plastic dish. Afterward, the dishes were incubated at 37 ºC 5% CO2 cell culture incubator for 3 hours for the entry of the plasmid. When 3 hours was done, 2 ml media was added, and cells were allowed to grow for 24 more hours.

2.4.4 Cell culturing onto silicon substrates

Previously cleaned silicon substrates were placed into 35 mm plastic bottom culture dishes (35 mm x 10 mm TC- treated plastic cell culture dish made up of polystyrene) before cell culture. The media of the cells grown for 24 hours were aspirated, and then cells were washed with pre-warmed 1X PBS. For dissociation of the cells from the dishes, 100 µL of TrypLE was added to the dishes and put back into a 37 ºC CO2 cell culture incubator for 5 minutes. When the incubation was done, trypsinization was stopped by adding 1 ml of media. Then, cells were gently collected into a 15 ml falcon. Afterward, the cells were centrifuged at 800 rpm for 7 minutes to remove TrypLE, then the supernatant was aspirated. The cell pellet was resuspended in 1 ml complete media and counted using a hemocytometer. To reach the desired number of cells for seeding, the cells were diluted in complete media. The desired number of cells, 85 x 10^3, was added onto a silicon substrate, and 2 ml media was added into 35 mm plastic bottom dishes. The cells were grown in a 37 ºC CO_2 cell culture incubator for further experiments. Schematic representations of the transfection and cell seeding onto silicon substrates experiments are shown in figure 2.5.

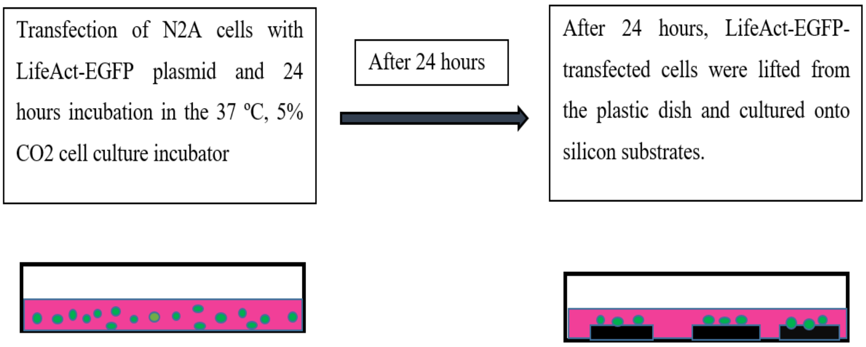

Transfection of N2A cells with LifeAct-EGFP plasmid and 24 hours incubation in the 37 ºC, 5% CO2 cell culture incubator

After 24 hours, LifeAct-EGFP-transfected cells were lifted from the plastic dish and cultured onto silicon substrates.

Figure 2.5: *Schematic representation of transfection and cell culturing onto silicon substrates.*

2.4.5 Differentiation of cells seeded onto silicon substrates and a plastic dish

To see whether cells' behavior in response to topographies when they are differentiated, cells were transferred to a differentiation medium after 24 hours of seeding onto substrates. The differentiation medium was optimized by one of our graduate students, Sara Mingu-Akmete. The components of the differentiation medium include %1 FBS medium, Retinoic acid (RA) (Chemcruz, Cat no: sc-200898), 1 M CaCl, and DMSO (Serva, Cat no: 39757.01). Per each sample, 2 ml total medium was prepared, and the ingredients of the medium were as follows: 1.9 ml %1 FBS medium, 30 ul 1 M CaCl, 20 ul DMSO, and 50 µl RA (800 µm) was mixed. Cells' media was aspirated, and a 2 ml differentiation medium was added and grown for 24 hours. After 24 hours, cells were fixed with %4 PFA and kept at +4º C for further experiments.

2.5 RNA isolation

Total RNA isolation was performed by using the GeneAll Hybrid-R^{TM} RNA isolation kit (GeneAll, Cat no: 305-101) following the manufacturer's instructions. The cells seeded on four different silicon substrates and a 35 mm plastic dish were collected after 24 hours. Approximately 2x10^{6} cells were collected for RNA isolation. All RNA samples were kept at -80º C after isolation. Shortly, cells were not washed with PBS before the addition of RiboEx^{TM}, because it may contribute to mRNA degradation. First of all, cells are lifted with 100 µl of TrypLE and collected into a falcon or an Eppendorf tube. Then, they were centrifuged at 800 rpm for 7 minutes. After the centrifuge, the supernatant was aspirated, and the pellet was resuspended in 1 ml of RiboEx^{TM}. This mixture was incubated at room temperature (RT) for 5 minutes. For 1 ml of RiboEx^{TM} , 200 µl chloroform was added to the mixture. The homogenate was shaken vigorously for 15 seconds and incubated at RT for 2 minutes. After incubation, the homogenate was centrifuged at 12.000 g, for 15 minutes at 4º C. When the homogenate was observed to separate into three phases, the upper colorless aqueous phase was transferred to a new 1.5 ml Eppendorf tube. Buffer RBI, the component of the kit, was added to the sample with the same volume of this aqueous phase and was mixed thoroughly by inverting. Up to 700 µl of this mixture was transferred into a spin column included in the kit and centrifuged at 10.000 g for 30 seconds in RT. Then, 500 µl of buffer SWI was added into the column and centrifuged at 10.000 g for 30 seconds in RT. Lastly, 500 µl of buffer RNW was added into the column and centrifuged at 10.000 g for 30 seconds in RT. To remove residual buffers, an extra centrifuge was performed at 10.000 g for 1 minute in RT. Following centrifugation, the column was transferred to a new 1.5 ml Eppendorf tube, and 50-100 µl RNase-free water was added to the column and left for incubation for 1 minute in RT. Finally, the sample was centrifuged at 10.000 g, for 1 minute at RT, and following centrifugation, the column was discarded, and then purified RNA was stored at -80º C. For RNA quantification, NanoDrop (Biochrom, UK) was used, and the ratios for the acceptable RNA sample are A260/280 ratio close to 2.0 and A260/230 ratio between 2.0 and 2.2.

2.5.1 cDNA Synthesis

Before performing cDNA synthesis, treatment of total RNA samples was carried out by using RNase-free DNase I (Thermo, Cat no: EN0521). For each cDNA synthesis, 1 µg of RNA sample was used by using RevertAid First Strand cDNA Synthesis Kit (Thermo, Cat no K1622) in a thermal cycler (Biorad T100 Thermal cycler cat no:1861096). Random hexamers were used in the cDNA synthesis reaction, and it was performed following the manufacturer’s instructions as shown in table 2.2 below. After the reaction, all synthesized cDNA samples were stored at -20 ºC.

Table 2.2: *cDNA synthesis protocol*

1. All the reagents below are added in a sterile, nuclease-free tube in the indicated order.	
RNA	1 µg
Random hexamer primer	1 µl
Nuclease-free water	to 12 µl
Total volume	12 µl
2. The mixture is vortexed and spinned-down briefly, and incubated at 65 º C for 5 minutes. Then, it is chilled on ice, spinned down, and put back on ice.	
3. Following components were added in the indicated order.	
5X Reaction buffer	4 µl
RiboLock RNase Inhibitor (20 U/µL)	1 µl
10 mM dNTP Mix	2 µl
RevertAid M-MuLV RT (200 U/µL	1 µl
Total volume	20 µl
4. The mixture was vortexed gently and spinned-down briefly.	
5. The mixture was incubated in the indicated protocol below: - at 25 º C for 5 minutes - at 42 º C for 1 hour - at 70 º C for 5 minutes	

2.5.2 qRT-PCR

To measure the expression of focal-adhesion-related genes, quantitative real-time PCR (qRT-PCR) assay was performed. The primer list and their NCBI reference sequences are given in table 2.3 and table 2.4 below, respectively. The final volume of this reaction was set to 25 in which µl 1 µl of cDNA (100 ng), and 24 µl reaction mix (0.5-1 µM of Forward and Reverse primers, 12.5 µl GoTaq qPCR Master Mix (Promega, Cat no: A6001) and dH2O to complete the final volume of the reaction). For internal control, GAPDH was used. The reactions were performed in CFX Connect Real-Time PCR Detection System (Biorad, Cat no: 1855201). The melt curve of primers was provided in Appendix B. For the expression analysis of genes, the Pfaffl method was used, which is explained in the next section. This method is based on the relative quantification of target genes and reference genes in which expression level differences are represented by physiological differences (Pfaffl, 2001).

Table 2.3: *Sequences and Tm values of primers used in this study*

Gene Name	Forward (5'-3')	Reverse (5'-3')	Tm ºC
FAK(PTK2)	ACTCACCTGGGTACTGGCAT	AGGTGACTGAGGCGAAATCC	59
FN (Fibronectin)	GGCTGAAGTCGCAAGGAAAC	CCTTCGGTGGTGCAGGAATA	62
FLNA (Filamin A)	TCAGCCAGTCGGAGATAGGT	GCCTGCATCTCTGGTGTCAA	62
LMNA (Lamin A/C)	AGTGAGAAGCGCACATTGGA	TATCGATCTCCACAAGCCGC	62
PXN (Paxillin)	TTCCAGATACGCTCACCAGC	AGTTCAGAGAGGTTGCTGCC	59
Src	TCCGACTTCGACAATGCCAA	GACATACGGTAGTGAGGCGG	64
TLN1 (Talin 1)	CCTACGAGCCGTTGGAGATG	TTCTGTGGCGGCCTGATTTA	62

TLN2 (Talin 2)	AGCTCATCTCATCCGCCAAG	TGGGCTGCACGAACAAGATT	62
VCL (Vinculin)	ATGGTGGACCTGAGGGAGAA	CCTCTGGCGAGTCTCCTTTC	59
ZYX (Zyxin)	CGAGTAGTGGCGCTGGATAA	ACTTCCGACAAAGGACGTGG	62

Table 2.4: *NCBI reference sequences of primers*

	NCBI Reference Sequence
FAK(PTK2)	NM_001358045.1, NM_001358046.1, NM_007982.2
FN (Fibronectin)	NM_010233.2, NM_001276408.1, NM_001276409.1, NM_001276410.1, NM_001276411.1
FLNA (Filamin A)	NM_010227.3, NM_001290421.1
LMNA (Lamin A/C)	NM_001002011.3, NM_019390.3, NM_001111102.2
PXN (Paxillin)	NM_133915.3, NM_011223.3
Src	NM_001025395.2, NM_009271.3
TLN1 (Talin 1)	NM_011602.5
TLN2 (Talin 2)	NM_001081242.2
VCL (Vinculin)	NM_009502.5
ZYX (Zyxin)	NM_011777.3, NM_001289617.1, NM_001289618.1, NM_001289619.1

2.5.2.1 Quantification of qRT-PCR results with the Pfaffl method

Pfaffl method is based on the relative quantification of target genes and reference genes. The ratio of the target gene is normalized to the expression of the reference gene. (Lefever S et al.,2009; Vandesompele J et al.,2022). To calculate the expression ratio between the reference gene and target gene, the following equations are used:

1. Cq value of the target gene is normalized to the reference gene for both the calibrator sample and the test sample:

Equation 2.2

$$\Delta \mathrm{Cq}(\mathrm{test}) = \mathrm{Cq}(\mathrm{target}, \mathrm{test}) - \mathrm{Cq}(\mathrm{ref}, \mathrm{test})$$
$$\Delta Cq(calibrator) = Cq(target, calibrator) - Cq(ref, calibrator)$$

2. To calculate the expression ratio between the test sample and calibrator for a target that is normalized to a reference gene above, the following equation can be used:

Equation 2.3

$$Ratio = (Etarget)\Delta Cq, target\ (calibrator - test)/(Eref)\Delta Cq, ref\ (calibrator - test)$$

In which

E_{target}	:The target gene’s amplification efficiency
E_{ref}	:The reference gene’s amplification efficiency
ΔCq, ref (calibrator - test)	:Cq of reference gene in the calibrator minus the Cq of the reference gene in the test sample
ΔCq, target (calibrator - test)	:Cq of the target gene in the calibrator minus the Cq of the target gene in the test sample

2.6 Protein Isolation & Quantification

Total protein isolation was performed by using Radioimmunoprecipitation assay buffer (RIPA) (Serva, Cat no: 39244-01) containing PMSF, and DTT as protease inhibitors and Na β-glycerophosphate pentahydrate and NaF as phosphatase inhibitors, and cOmplete Mini EDTA-free Protease Inhibitor Cocktail (Roche, Cat no: 05892791001) following the manufacturer’s instructions. In short, cells’ media was aspirated, and then cells were washed with ice-cold 1X PBS twice. Then, 1 ml cold RIPA, which contains freshly added inhibitors, was added to the cells. Cells were kept on ice for 5 minutes. After that, cells were collected into a falcon or an Eppendorf tube. Collected cells were centrifuged for 15 minutes at 14.000 g at 4 ºC. When the centrifuge was done, the supernatant was transferred to a new Eppendorf tube and kept at -80 ºC until further analysis. Protein concentration measurement was carried out with Bradford assay using Coomassie Protein Assay Reagent (Thermo, Cat no: 23200), and then for standard curve generation, bovine serum albumin (BSA) was used. For measurement of protein concentration, 5 µl of total protein and 250 µl Coomassie Protein Assay Reagent was mixed in a well of a microplate. The absorbance value was measured in a Multiskan-GO microplate reader (Thermo Fisher Scientific, USA) at 595 nm. According to the standard curve, the amount of the isolated protein was calculated. All isolated proteins were stored at -80 º after isolation and quantification.

2.7 Western Blot

Western Blot was used to measure the expression level of proteins of interest in the cells grown on the silicon substrates. Buffer compositions and chemicals used for Western Blot experiments were shown in Appendix C. For the separation of total proteins, SDS-Polyacrylamide Gel Electrophoresis (SDS-PAGE) at 100 V in 8% Acrylamide/Bis-acrylamide gels was used. Equally, 25 µg of every sample was loaded per well. As a ladder, Page Ruler Plus Prestained Protein Ladder, ranging from 10 to 250 kDa (Thermo Fisher Scientific, Cat no: 26619), was used. When the proteins were separated in the SDS-PAGE, the transfer of proteins from SDS-PAGE gel to the Polyvinylidene Fluoride (PVDF) membrane (Biorad, Cat no: 162-0177) was performed for 1.5 hours at 115 V at 4 ºC by using the wet-transfer method. Upon transfer was completed, the membrane was blocked in TBS-T containing 5% skimmed milk or Bovine Serum Albumin (BSA) (Sigma, Cat no:3608). Overnight incubation of primary antibodies was carried out at 4 ºC. When the incubation of primary antibodies, listed below in table 2.5, was done, membranes were washed with TBS-T for 10 minutes three times. Following, secondary antibody incubation was performed at room temperature for 1 hour and then washed again with TBS-T for 10 minutes three times. For imaging of membranes, Immobilon® Forte Western HRP Substrate (Millipore, Cat no: WBLUF0100) was used as the visualization reagent for 2 minutes and then imaged in a Chemi-Doc MP (Biorad, USA). As a loading control, the GAPDH antibody was used to confirm equal protein loading.

Table 2.5: *Primary and secondary antibodies used in this study*

Antibody name	**Size (kDa)**	**Cat no:**	**Origin**	**Brand**	**Dilution**	**Medium**
GAPDH	37	sc-25778	Rabbit	Santa Cruz	1:2000	%5 Skimmed milk
Zyxin	78	3553S	Rabbit	Cell signaling Technologies (CST)	1:1000	%5 BSA
Ptk2 (FAK)	125	sc-271126	Mouse	Santa Cruz	1:750	%5 Skimmed milk
Anti-mouse secondary antibody		sc-2005	Goat	Santa Cruz	1:750	%5 skimmed milk
Anti-rabbit secondary antibody		7074S	Goat	Cell signaling technologies	1:2000	%5 BSA

2.7.1 Band Intensity Quantification of Western Blot

For the quantification of Western Blots, the Image J program (NIH, Bethesda, MD, USA) was used. First of all, to encompass the first band in a row, a rectangular shape was drawn and the same rectangular shape was used to identify the following bands in the same row. After all bands were selected, band intensities were calculated with the ImageJ program and the data were recorded in an Excel sheet. After that, the average intensities of the bands were calculated and each band intensity was divided into the average band intensity in the same blot. This process is named as gel normalization. For the GAPDH as an internal control, the same procedure was followed to obtain GAPDH gel normalization. By dividing the gel normalization of each protein into the GAPDH normalization, standard normalization values were obtained (Karoglu et al., 2017)

2.8 Imaging

2.8.1 Cell fixation and Fluorescence Microscopy Imaging

For fluorescence imaging, cells were first fixed with 4% paraformaldehyde (PFA). The experiments were carried out in the dark and laminar flow hood because of the light sensitivity of PFA. In short, cells' media was aspirated, and then cells were washed with 1X PBS. Then, 1 ml fresh media and 1 ml cold 4% paraformaldehyde (PFA) were added to the cells. After 2 minutes of incubation, this solution was aspirated, and 2 ml 4% paraformaldehyde (PFA) was added to the cells in a dropwise manner and incubated at room temperature and in the dark for 15 minutes. Upon incubation was done, the solution was aspirated, and the cells were washed with 1 ml 1X PBS twice so that any remaining fixative reagent was discarded. The substrates were kept at 4ºC for further experiments. For fluorescence imaging, the substrates were put down on a coverslip (No.0) and then imaged using 10X or 63X oil objectives. A representation of the imaging setup is shown below in figure 2.8.

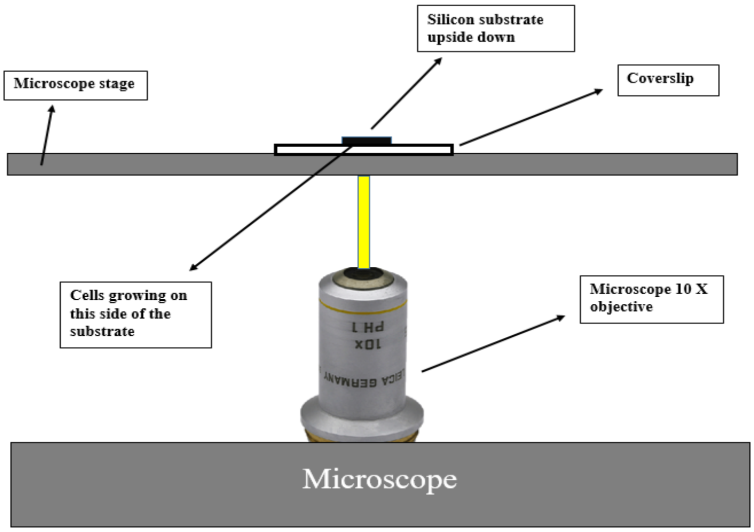

Figure 2.6: *Scheme showing the microscopy imaging set-up. In all experiments, cells were upside-down. For simplicity, only the bottom part of the microscope was shown.*

2.8.2 Atomic Force Microscopy (AFM) Imaging

AFM of Nanomagnetic Instruments brand was used for AFM imaging in which the tapping mode of operation was used, and the scanned area of samples was 50-10 µm and 10-1 µm. As this imaging technique does not require any processing, such as coating, silicon substrates were directly imaged with AFM. However, samples were cleaned in an ultrasonic water bath with acetone, isopropanol, and distilled water for 10 minutes so that any contaminants or dust, which prevent AFM tip to approach to the surface and result in false feedback and bad quality images. AFM software, Gwyddion software, was used to calculate various surface roughness Ra (Roughness Average) or RMS (Root Mean Square). In several cell studies, Ra was used as a value for surface roughness; however, in this study, both Ra and RMS were used to indicate surface roughness.

2.8.3 Energy-dispersive X-ray spectroscopy (EDS or EDX) Imaging

EDS imaging was taken with a Zeiss Evo HD15 SEM instrument. For imaging, EDAX software was used. Before EDS imaging, samples were not cleaned with any chemicals or an ultrasonic water bath. The instrument does not measure any particles or elements with a concentration below 10^5. The position of the peaks in the spectrum indicates the element, and the intensity of the peaks indicates the concentration of the elements.

2.9 Statistical analysis

For all experiments in this study, at least two or three independent biological replicates were included. At least three technical replicates were included in each biological replicate. To perform statistical analyses and generation of graphs, GraphPad Prism 8.0 Software (GraphPad Software Inc., USA). To determine statistical differences, One-way ANOVA and Two-way ANOVA were used in which a p-value of <0.05 was taken as statistically significant.

CHAPTER 3

RESULTS

3.1 Substrate fabrication and characterization

Substrate fabrication was carried out by controlling the number of shots (N) falling onto the spot by fine-tuning the scanning velocity of the beam. LIPSS structure, grating-like structures with wavelengths similar to the irradiation wavelength (called low spatial frequency LIPSS, or LSFL), was obtained with a small shot number (N<10). Feedback loops are known to be involved in LIPSS formation. Regarding ablation-type LIPSS, the formation of periodic structures results from a positive feedback loop; however, a negative feedback loop is not involved, and if more laser shots were applied to the area, the periodicity may be lost. This is how a microcolumn-like structure can form. The process is shown in figure 3.1 below (Pavlov *et al.*, 2013).

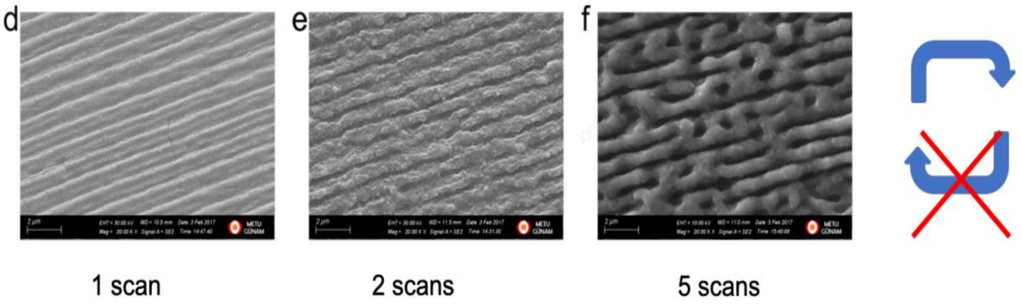

Figure 3.1: *SEM images of the formation of topography on a substrate and the gradual formation of microcolumns from LIPSS topography. Adapted from Pavlov et al, 2013.*

However, the microcolumn formation can be obtained directly by controlling the number of shots sent to an area via the scan velocity, which is used in this study as a method to create microcolumn topography. While fast scans (1.5 m/s and above) aid the formation of LIPSS, slower scans (0.1 m/s) result in the formation of microcolumn. Highly regular periodicity is characteristic of LIPPS, and in a way, it resembles a grating structure created by lithography but with smooth edges. By controlling the beam polarization, LIPSS direction can be manipulated. The LIPSS created in this study is an ablation type with direct proportion to the laser polarization. According to the theory, microcolumn or coral-like structures are formed as a result of higher fluences (Vorobyev & Guo, 2012; Vorobyev & Guo, 2009). Although there are many studies about the behavior of cells grown on LIPSS topography, there are few studies regarding microcolumn topography and cell interaction. SEM and AFM images of topographies used in this study are shown in the next sections.

3.1.1 SEM imaging

SEM images of LIPSS (figure 3.2) and microcolumn (figure 3.3) topographies used in this study can be seen below. The homogeneity and regularity of LIPSS lines can be seen in SEM images in figure 3.2. As discussed before, fast scans (1.5 m/s) result in LIPSS formation; slower scans result in microcolumn formation. In this study, for the creation of LIPSS 1.5 m/s was used, and 0.5 m/s was used for microcolumn formation.

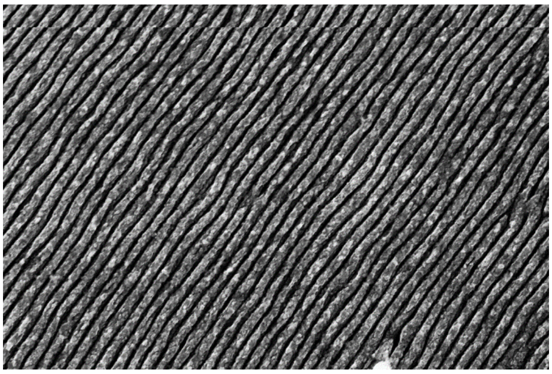

Figure 3.2: *SEM images of LIPSS topography structured on a silicon substrate. Magnification: 10000X; Scale bar is 1µm*

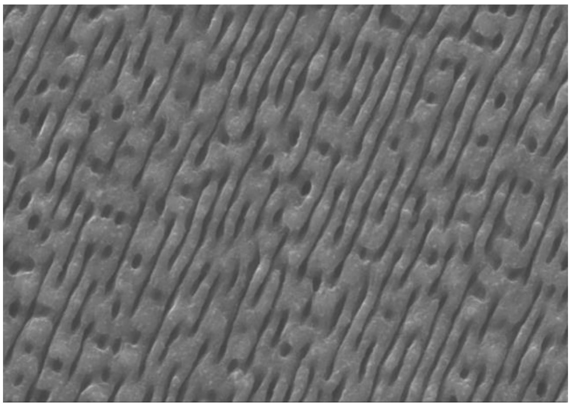

Figure 3.3: *SEM images of microcolumn topography structured on a silicon substrate. Magnification: 10000X; Scale bar is 2 μm*

Atomic force microscopy (AFM) can give further information about topography, such as surface roughness and height information. AFM images of LIPSS and microcolumn topographies and related topographical analysis are shown in the next section.

3.1.2 AFM imaging

By AFM analysis using Gwyddion software, height information, Roughness average (Ra), and curvature analysis were carried out for LIPSS (figure 3.4) and microcolumn (figure 3.5) topographies in a 10 μm area. Combined topography, including both LIPSS and microcolumn topographies together, was not measured because of the limitations of the scan area of the AFM microscopy, which scans the area up to 100 μm.

According to AFM surface roughness (Ra) results, the Ra value of LIPSS equals 69.6 nm, while the Ra value of microcolumn equals 51.7 nm. Another surface roughness parameter is the root mean square (RMS or Rq), 92.5 nm for LIPSS, and 65 nm for microcolumn topography.

Other parameters related to surface roughness, skewness (peaks vs. valleys), and kurtosis (sharpness density of peaks), were also measured. According to the literature, a positive/higher skewness is an indication of high peaks and filled valleys on the surface. At the same time, a negative/lower one indicates deep scratches (grooves) and a lack of peaks on the surface. On the other hand, a kurtosis value larger than 3 means that there are high peaks and/or low valleys on the surface, whereas a kurtosis value lower than 3 means low peaks and/or valleys are present on the surface (Liu *et al.*, 2015).

According to AFM results, LIPSS topography has a skewness value of 0.796 nm and a kurtosis value of 6.10 nm, whereas a skewness value of 0.200 nm and a kurtosis value of 3.13 nm was calculated in microcolumn topography.

Altogether, AFM analysis indicates surface roughness of LIPSS topography is higher than microcolumn topography, and LIPSS includes more peaks and filled valleys than microcolumn topography. In the literature, it is shown that moderately rough surfaces induce cell adhesion, cell growth, and cell proliferation. So, it can be concluded that there is a positive correlation between surface roughness and cell attachment (Majhy *et al.*, 2021; Zareidoost *et al.*, 2012).

Regarding the interaction of peaks and valleys with cells, it is shown that cells make the initial contact at the peaks which induces the focal adhesion complex formation at the peaks. It is assumed that these peaks and valleys might resemble the nanoroughness of ECM and make adhering to most cell types easier (Stanton, 2014).

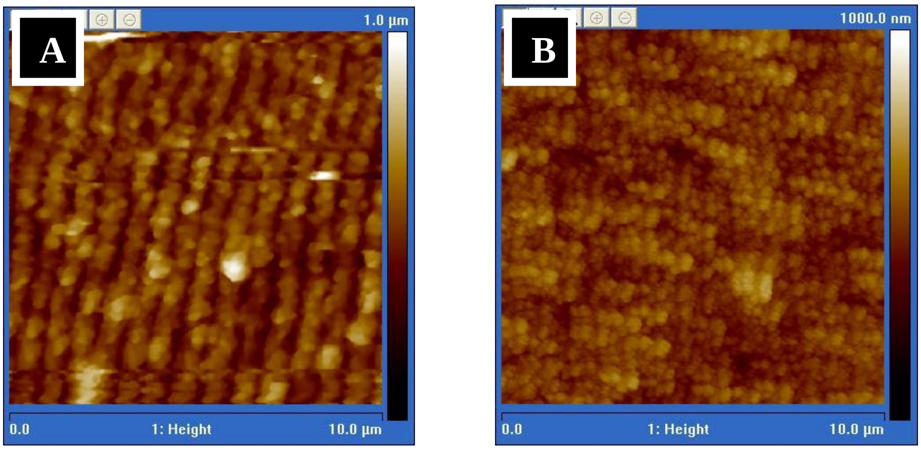

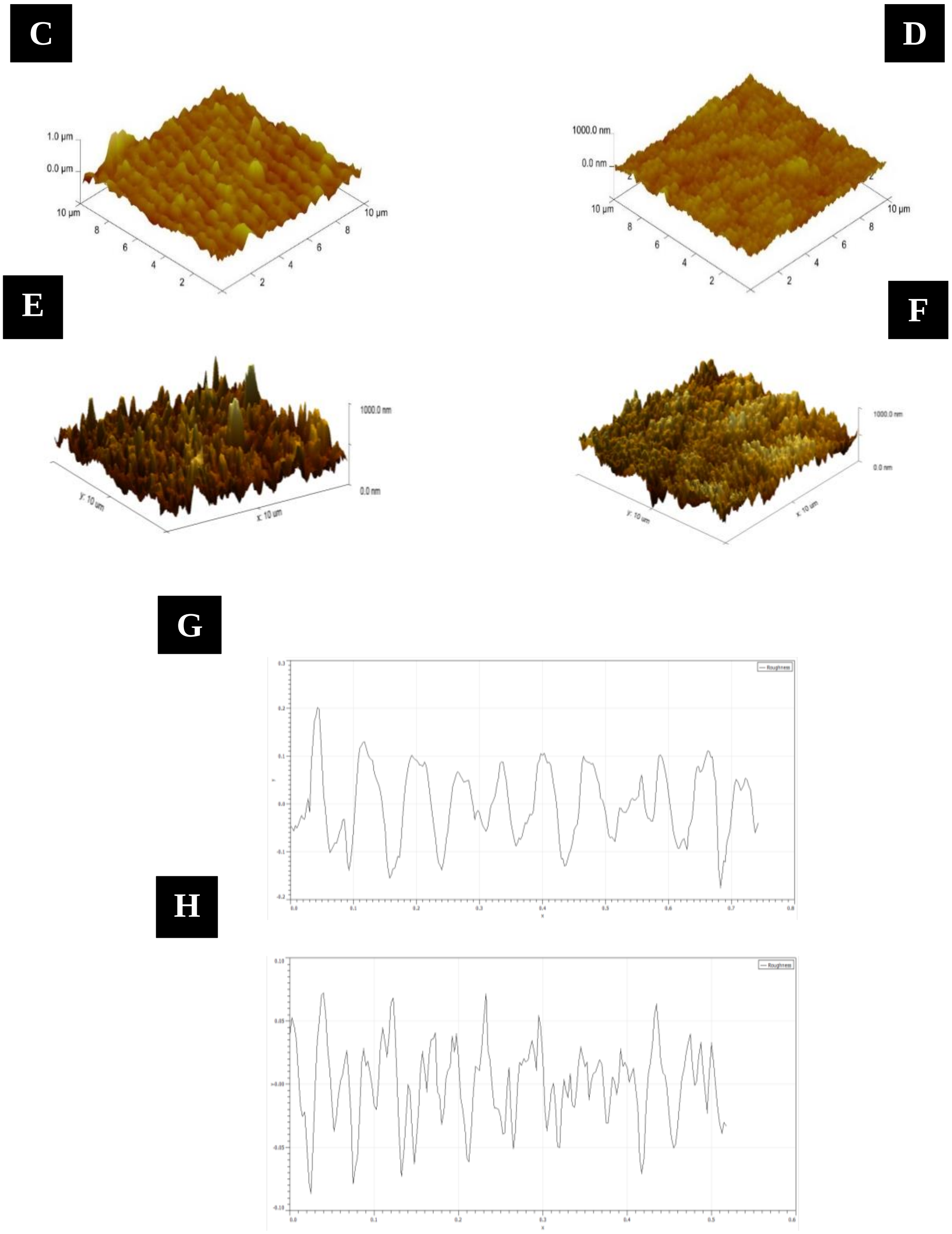

Figure 3.4: *AFM images of LIPSS and microcolumn topography.*

(A) and (B) 2D view of LIPSS and microcolumn, respectively. (C) and (D) 3D view of LIPSS and microcolumn topography, respectively; (E) and (F) coloring analysis of peaks and valleys in LIPSS and microcolumn topography in 3D view, respectively.

(G) and (H) roughness of a surface from a randomly chosen area in LIPSS and Microcolumn, respectively.

Another topographical analysis type which is height distribution in LIPSS and microcolumn topographies is shown below in figure 3.5.

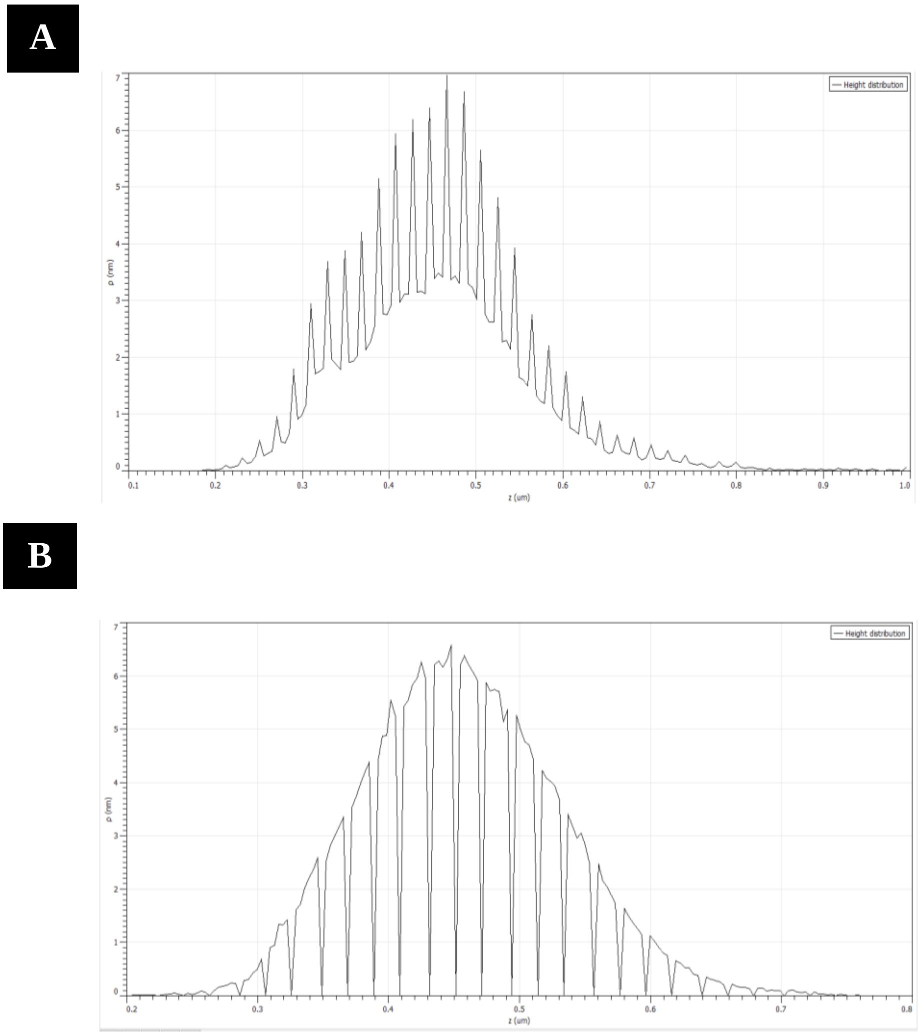

Figure 3.5: *Height distribution analysis in LIPSS (A) and microcolumn (B) topography by height distribution function P(Z).*

All AFM analysis was performed in Gwyddion software.

As AFM data indicates, LIPSS has more peaks and filled valleys compared to microcolumn topography. In addition, the surface roughness of LIPSS, both in Ra and RMS, is relatively higher than in microcolumn. These characteristics of LIPSS might resemble the nanoroughness of ECM, which triggers more cell adhesion and affect different cell behaviors, which will be discussed in the next sections.

3.1.3 EDS analysis

The next question related to surface topography and cell behavior interaction is whether changes in cell behavior purely result from topography or any chemical/elemental changes induced by femtosecond laser contribute to these changes. To answer this question, EDS analysis was carried out for silicons fabricated with the femtosecond laser and unstructured/polished silicon as a control. EDS analysis below shows that there are no elemental changes in the substrates with topographies compared to control (unstructured) silicon; however, oxidation was observed on these substrates, which is a natural cause of femtosecond laser fabrication. EDS analysis for different topographies and unstructured silicon is shown below in figure 3.6 to figure 3.9. Different areas from the silicon substrates were chosen, and EDS measurements were taken. According to EDS results, no change in elemental composition was detected. More images of EDS analysis from different selected areas are shown in Appendix A.

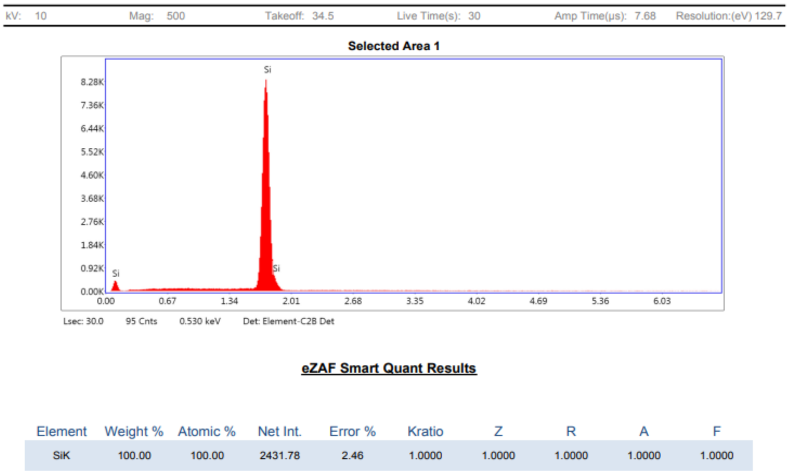
kV: 10 Mag: 500 Takeoff: 34.5 Live Time(s): 30 Amp Time(µs): 7.68 Resolution:(eV) 129.7

Selected Area 1

Lsec: 30.0 95 Cnts 0.530 keV Det: Element-C2B Det

eZAF Smart Quant Results

Element	Weight %	Atomic %	Net Int.	Error %	Kratio	Z	R	A	F
SiK	100.00	100.00	2431.78	2.46	1.0000	1.0000	1.0000	1.0000	1.0000

Figure 3.6: *EDS analysis of unstructured/polished silicon.*

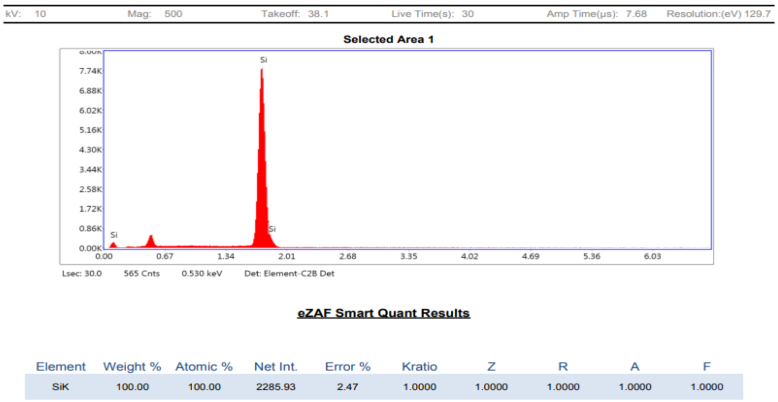

kV: 10 Mag: 500 Takeoff: 38.1 Live Time(s): 30 Amp Time(μs): 7.68 Resolution:(eV) 129.7

Lsec: 30.0 565 Cnts 0.530 keV Det: Element-C2B Det

eZAF Smart Quant Results

Element	Weight %	Atomic %	Net Int.	Error %	Kratio	Z	R	A	F
SiK	100.00	100.00	2285.93	2.47	1.0000	1.0000	1.0000	1.0000	1.0000

Figure 3.7: *EDS analysis LIPSS topography on a silicon substrate.*

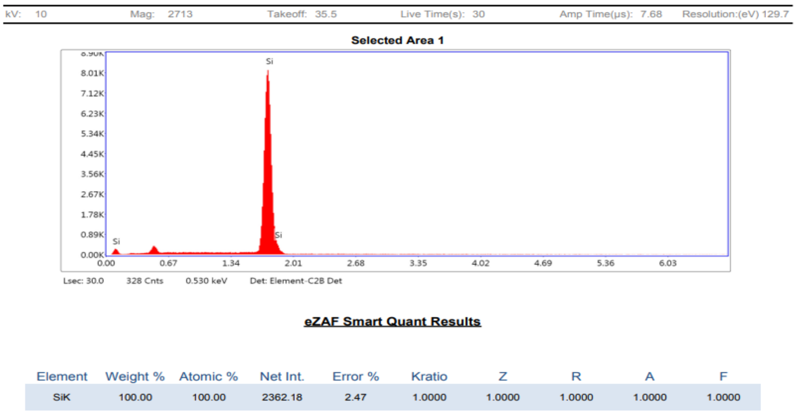

kV: 10 Mag: 2713 Takeoff: 35.5 Live Time(s): 30 Amp Time(μs): 7.68 Resolution:(eV) 129.7

Lsec: 30.0 328 Cnts 0.530 keV Det: Element-C2B Det

eZAF Smart Quant Results

Element	Weight %	Atomic %	Net Int.	Error %	Kratio	Z	R	A	F
SiK	100.00	100.00	2362.18	2.47	1.0000	1.0000	1.0000	1.0000	1.0000

Figure 3.8: *EDS analysis microcolumn topography on a silicon substrate.*

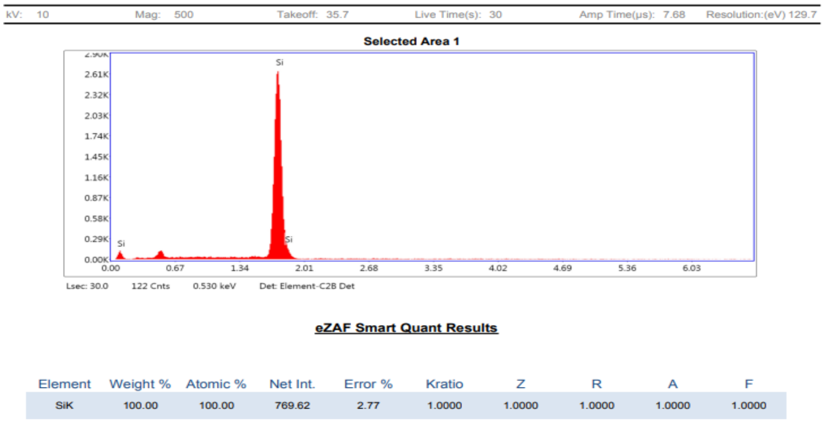

kV: 10 Mag: 500 Takeoff: 35.7 Live Time(s): 30 Amp Time(μs): 7.68 Resolution:(eV) 129.7

Lsec: 30.0 122 Cnts 0.530 keV Det: Element-C2B Det

eZAF Smart Quant Results

Element	Weight %	Atomic %	Net Int.	Error %	Kratio	Z	R	A	F
SiK	100.00	100.00	769.62	2.77	1.0000	1.0000	1.0000	1.0000	1.0000

Figure 3.9: *EDS analysis of Combined topography (LIPSS+MC) on a silicon substrate.*

So, the EDS data indicates that cell behavioral changes do not result from chemical changes induced by femtosecond laser fabrication in silicon substrates.

3.2 Cell behavior on unstructured polished silicon, and LIPSS, Microcolumn topographies

3.2.1 Cell behavioral response after 24 hours

The actin cytoskeleton of cells was imaged using confocal fluorescent microscopy after 24 hours of seeding cells onto silicon substrates. To analyze whether cell behavior will change when they are differentiated or not, cells were exposed to a differentiation medium for 24 hours. After that, they were imaged with confocal fluorescent microscopy. For observation of both cells and topography, SEM imaging was performed. Before SEM, all samples were coated with a 3 nm Gold-Palladium Pd) mixture to increase surface conductivity. For all SEM images, there is no tilt angle, all images were taken directly perpendicular to the surface.

3.2.1.1 Cell adhesion and cell alignment

To observe how cell adhesion and alignment of the actin cytoskeleton were changed in response to different topographies, cells were transfected with LifeAct-EGFP plasmid. Following transfection, cells were fixed and imaged with confocal fluorescent microscopy and SEM after 24 hours. In a different experimental setup, cells were differentiated after 24 hours and then imaged with confocal fluorescent microscopy. Leica DMI 4000 equipped with Andor DSD2 spinning disc confocal microscope was used for confocal fluorescent microscopy imaging. Confocal fluorescent microscopy and SEM images of cells seeded on different topographies were shown below.

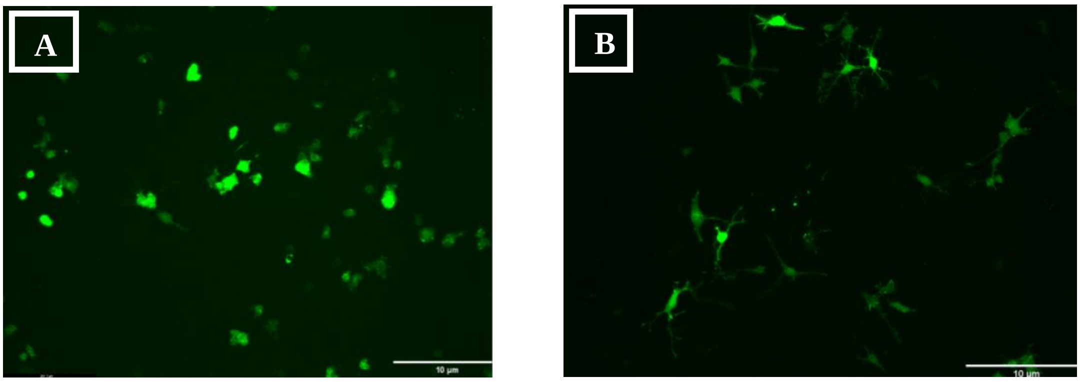

Figure 3.10: *Fluorescence microscopy of cells transfected with LifeAct-EGFP plasmid for visualization of actin. Cells were seeded onto a plastic dish.*

Cells were grown in a plastic dish before differentiation (A, 10X) and after differentiation (B, 10X). Images were taken with Leica spinning disc confocal microscope. All scale bars are 10 µm

Cells grown in a standard cell culture plastic dish before and after differentiation shows no alignment.

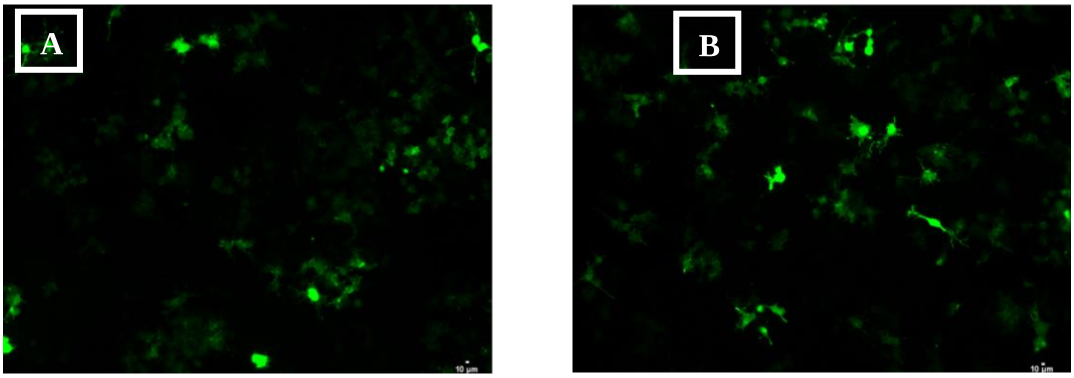

Figure 3.11: *Fluorescence microscopy of cells transfected with LifeAct-EGFP plasmid for visualization of actin. Cells are seeded onto an unstructured/polished silicon.*

Cells were grown on unstructured/polished silicon before differentiation (A, 10X) and after differentiation (B, 10X). Images were taken with Leica spinning disk confocal microscopy. All scale bars are 10 µm

In unstructured/polished silicon, cells show good spreading and develop more stress fibers compared to cells in the plastic dish. Stress fiber formation is more prominent before differentiation; however, after differentiation, cells' axons become more elongated. Although stress fiber formation and spreading of cells in unstructured/polished silicon are more obvious, no alignment of the cells' axons or stress fibers was observed in these samples.

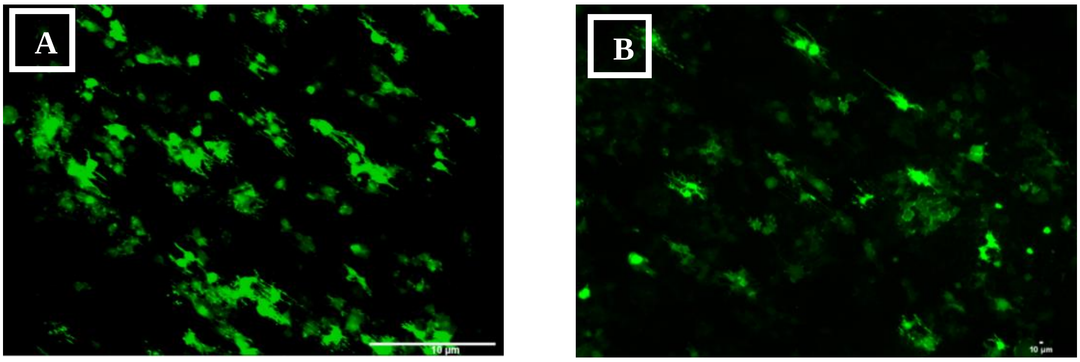

Figure 3.12: *Fluorescence microscopy of cells transfected with LifeAct-EGFP plasmid for visualization of actin. Cells were seeded onto a combined topography.*

Cells were grown on a combined topography (LIPSS+MC) on silicon substrate before differentiation (A, 10X) and after differentiation (B, 10X). Images were taken with Leica spinning disk confocal microscopy. All scale bars are 10 µm

The cell alignment which is observed in combined topography is most probably, cells aligned with the LIPSS topography, not with microcolumn. The separate confocal images of LIPSS and microcolumn topographies shown below confirm this hypothesis that in microcolumn topography, there is little or no alignment of the cells compared to LIPSS. Also, the cell adhesion in microcolumn topography is lower than in LIPSS, and combined topography.

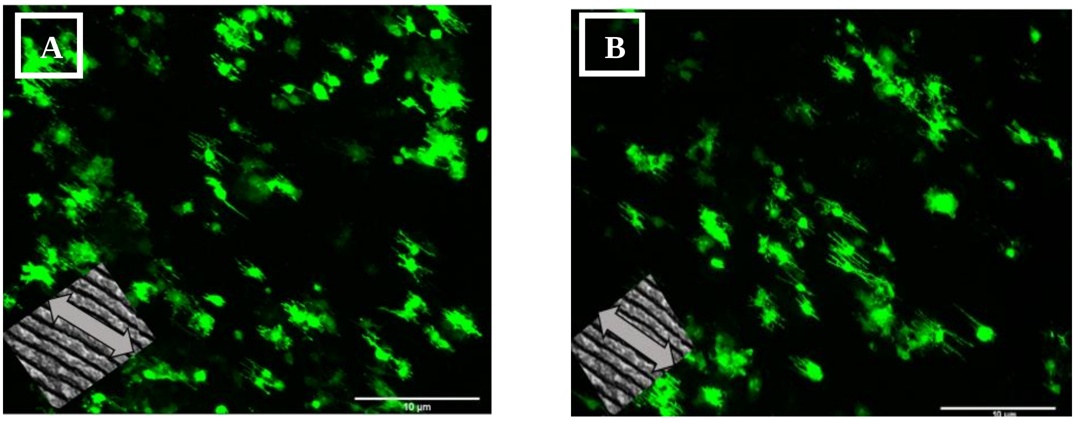

Figure 3.13: *Fluorescence microscopy of cells transfected with LifeAct-EGFP plasmid for visualization of actin. Cells are seeded onto a LIPSS topography.*

Cells were grown on LIPSS topography on silicon substrate before differentiation (A, 10X); and after differentiation (B, 10X). Images were taken with Leica spinning disk confocal microscopy. All scale bars are 10 µm

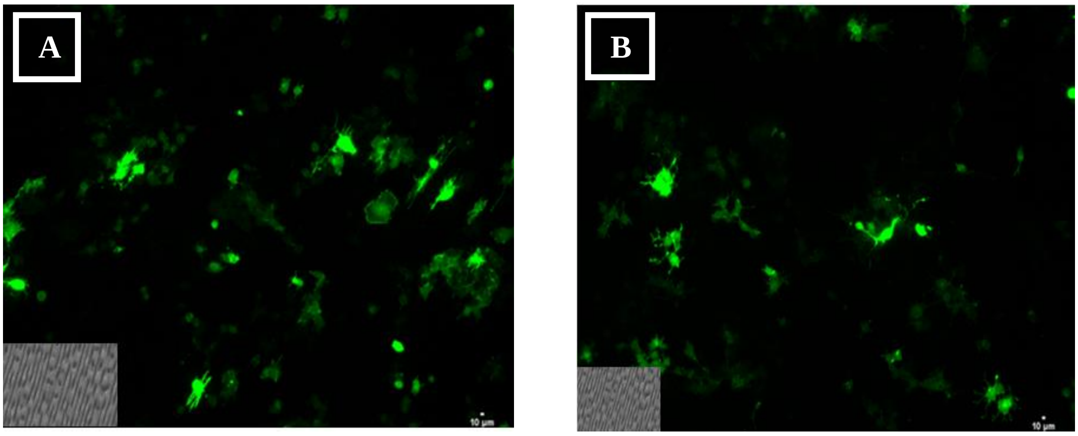

Figure 3.14: *Fluorescence microscopy of cells transfected with LifeAct-EGFP plasmid for visualization of actin. Cells are seeded onto a microcolumn topography.*

Cells were grown on microcolumn (MC) topography on silicon substrate before differentiation (A, 10X) and after differentiation (B, 10X). Images were taken with Leica spinning disk confocal microscopy. All scale bars are 10 µm.

Confocal imaging of cells on different topographies are replicas of the previous study (Mingu, 2020), and quantification of this imaging, such as cell shape, cell area, and cell circularity results, can be found in Mingu’s (2020) study. The novel part of this study comes from the results of focal adhesion-related gene and protein expression level changes in response to different topographies.

Due to limitations of the sample area size of SEM, SEM imaging was not performed for the plastic dish. Also, cell adhesion to unstructured/polished silicon was weak, indicating cells were mostly lost during the 4% PFA fixation step. The second step of sample preparation for SEM, graded alcohol dehydration of samples, made all cells lose contact with the surface. Therefore, SEM images of polished silicon could not be taken.

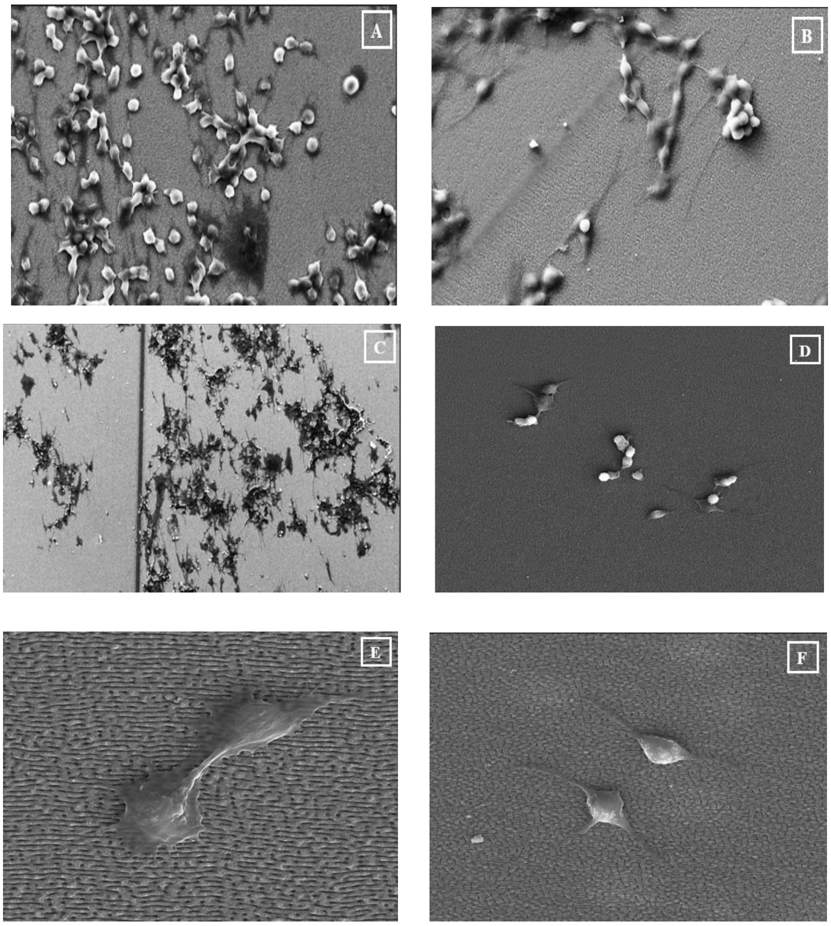

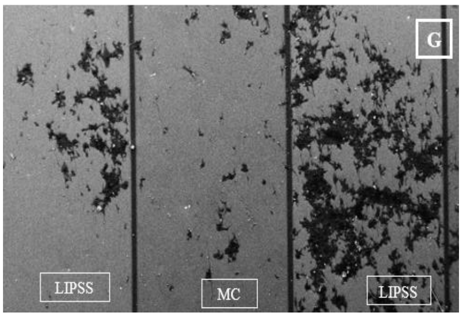

Figure 3.15: *SEM images of cells seeded on LIPSS (A-C), microcolumn (D-F), and Combined (LIPSS+MC) (G) topographies.*

Magnifications and scale bars; A: 1.000X; 10 µm; B: 1200X; 10 µm; C: 200X; 100 µm, D: 1000X; 100 µm; E: 5000X; 20 µm; F: 2500X; 40 µm; G: 100X; 100 µm.

3.2.1.2 Cell number and cell proliferation

To measure cells' viability in response to different topographies, cells were counted after 24 hours of seeding. Three replicates were used for three different topographies, unstructured silicon, and plastic dish, and their mean was calculated. According to the results, apart from the plastic dish, cells' adhesion preference on LIPSS topography is more prominent compared to other topography and unstructured silicon.

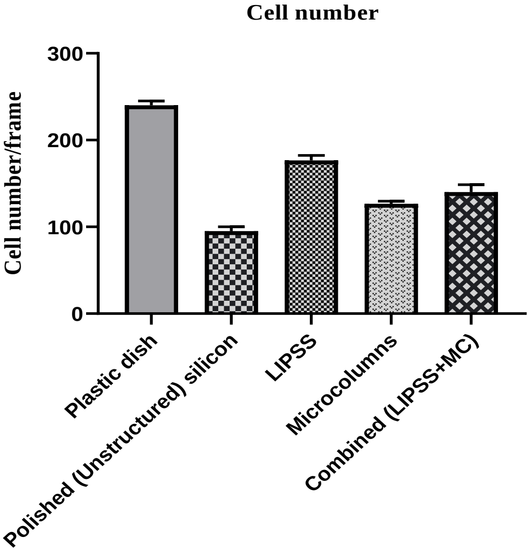

Figure 3.16: *Average cell number on a plastic dish, unstructured silicon, and three different topographies after 24 hours of cell seeding. The data shown as Mean ± SEM*

For cell counting, a hemocytometer was used. At least three replicates of each sample were used for the experiment. Cells were not in a differentiation medium. For each sample, 85x10^3 cells were seeded at the beginning. 1.5 x 1.5 cm silicon substrates were used for imaging and counting.

Another question was whether cell proliferation was affected following seeding onto silicon substrates or not. To assess this, cell number was counted for different periods (24 hr, 36 hr, 48 hr, and 72 hr) using a hemocytometer.

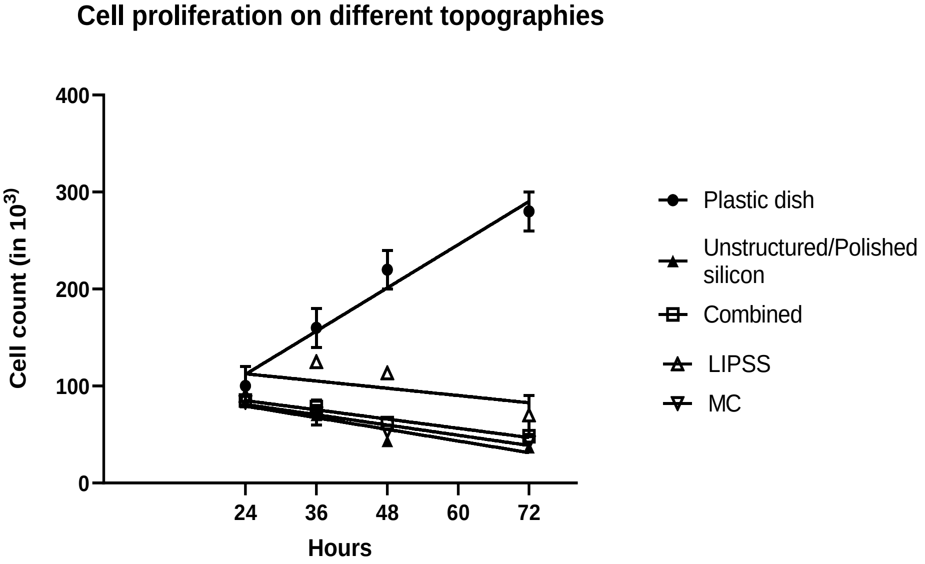

Figure 3.17: *Cell numbers after 24, 36, 48, and 72 hours on a plastic dish, unstructured silicon, and three different topographies after 24 hours of cell seeding.*

For cell counting, a hemocytometer was used. At least three replicates of each sample were used for the experiment. Cells were not in a differentiation medium. For each sample, 85x10^3 cells were seeded at the beginning. 1.5 x 1.5 cm silicon substrates were used for imaging and counting.

According to the results, cell proliferation was lower on all silicon substrates compared to the plastic dish as shown in figure 3.17. First 24 hours, on all silicon substrates, cell proliferation, although it was less, was observed. However, on LIPSS, cells seem to divide until 48 hours of seeding. However, after 48 hours, cells seem not to divide on all topographies although, on LIPSS, there is still proliferation after 48 hours but not comparable to the plastic dish. To conclude, although the proliferation of cells on LIPSS topography is not comparable to the plastic dish, it is the best substrate for the proliferation of cells among other topographies and unstructured/polished silicon.

3.3 Focal adhesion-related genes and protein changes in the cells grown on silicon substrates

3.3.1 qRT-PCR Analysis

To measure how cells' focal adhesion-related genes gave a response to different topographies, ten different focal adhesion-related genes were selected according to the literature. Before measuring the effect of topography on expression levels of focal adhesion-related genes, and the effect of unstructured silicon on the expression level of these genes, cells were cultured on plastic dish and unstructured silicon only (figure 3.18A).

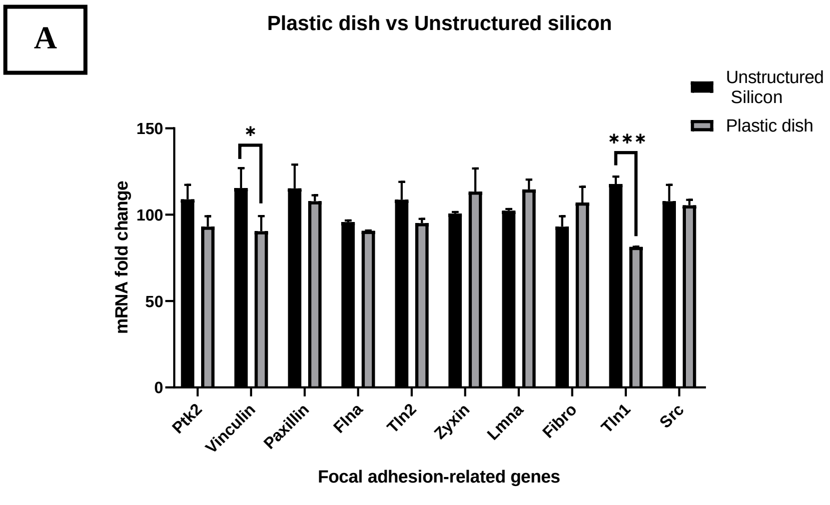

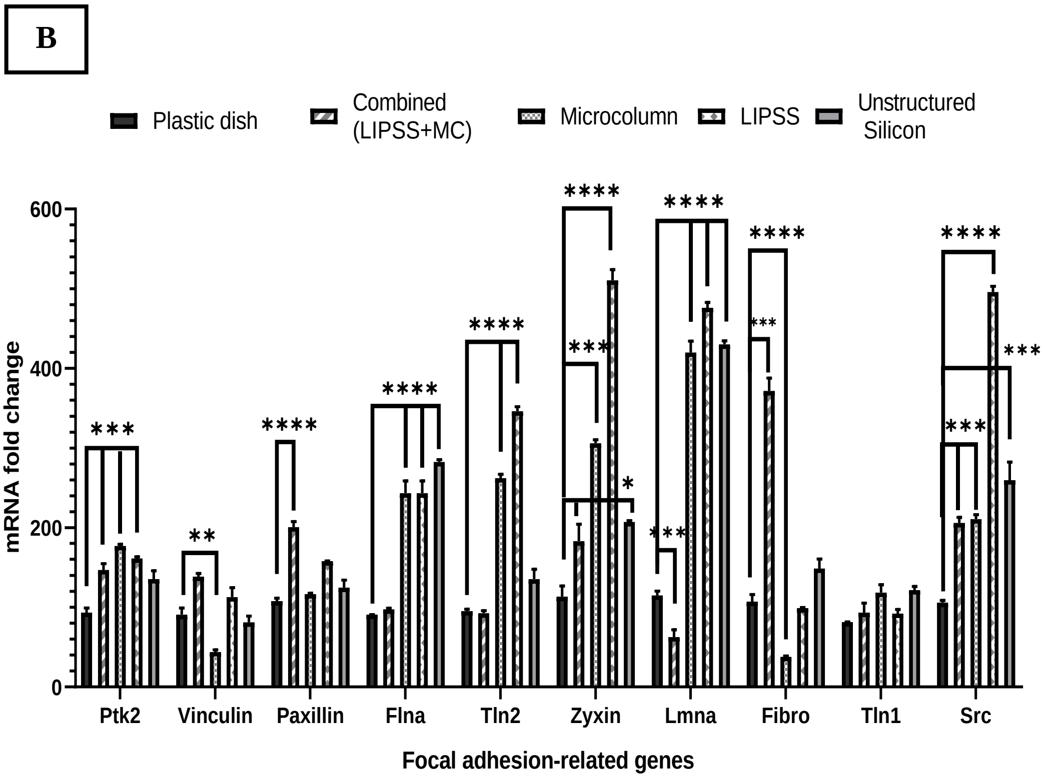

Figure 3.18: *qRT-PCR analysis of focal adhesion-related genes.*

(A) qRT-PCR analysis of focal adhesion-related genes of cells in unstructured silicon and plastic dish. (B) qRT-PCR analysis of focal adhesion-related genes of cells from four silicon substrates and a plastic dish as a control.

100 ng sample cDNA was used for each reaction with 3 internal replicates. Reactions were performed in 39 cycles. A p-value of <0.05 was taken as statistically significant. Two-way ANOVA was used for analysis. As an internal control, GAPDH was used. Fold change values were expressed as a percentage compared to the control group (plastic dish) which is taken as 100. Data were normalized to GAPDH and analyzed using the Pfaffl method. (Pfaffl, 2001).

According to qRT-PCR results in figure 3.18A, only two genes, talin1, and vinculin were significantly upregulated on unstructured silicon. The other eight genes did not give significant changes which indicate that the changes we observed in focal adhesion-related genes in figure 3.18B are the results of topography not because of the silicon as a substrate.

According to qRT-PCR results, 70% (7/10) of the focal adhesion-related genes we chose showed an increasing trend and/or significantly upregulated on all topographies and unstructured/polished silicon. The top three upregulated genes are zyxin, lamin A/C (Lmna), and src which are on all topographies, and unstructured/polished silicon, except lamin A/C, showed downregulation in combined topography. Two genes that show significant downregulation is vinculin and fibronectin which are from the microcolumn topography. However, vinculin showed an increasing trend (not significant) on LIPSS and combined topography and showed a decreasing trend (not significant) on unstructured/polished silicon. Ptk2 (FAK) gene showed significant upregulation on all three topographies and an increasing trend (not significant) on unstructured/polished silicon. Paxillin revealed significant upregulation on combined topography, and an increasing trend (not significant) on LIPSS, MC, and unstructured/polished silicon. Filamin A (Flna) exhibited significant upregulation on LIPSS, MC, and unstructured/polished silicon, although it showed an increasing trend (not significant) on combined topography. Talin 2 (Tln2) exhibited upregulation on LIPSS and MC, increasing trend (not significant) on unstructured/polished silicon; however, it shows no change in combined topography. Fibronectin (Fn) showed a decreasing trend (not significant) on LIPSS, downregulation on MC topography, upregulation on combined topography, and an increasing trend (not significant) on unstructured/polished silicon. Talin 1 (Tln1) exhibited an increasing trend (not significant) on all topographies compared to the plastic dish.

3.3.2 Western Blot

One of the most upregulated genes, Zyxin, and PTK2 (FAK) was chosen for protein analysis in Western Blot. The reason for choosing PTK2, although it is not among the most upregulated and/or downregulated genes, it is because it is the main player in the FAK-dependent mechanotransduction. Other players like talin, vinculin, and paxillin, are recruited to the focal adhesion site as a result of the recruitment of FAK to the focal adhesion site.

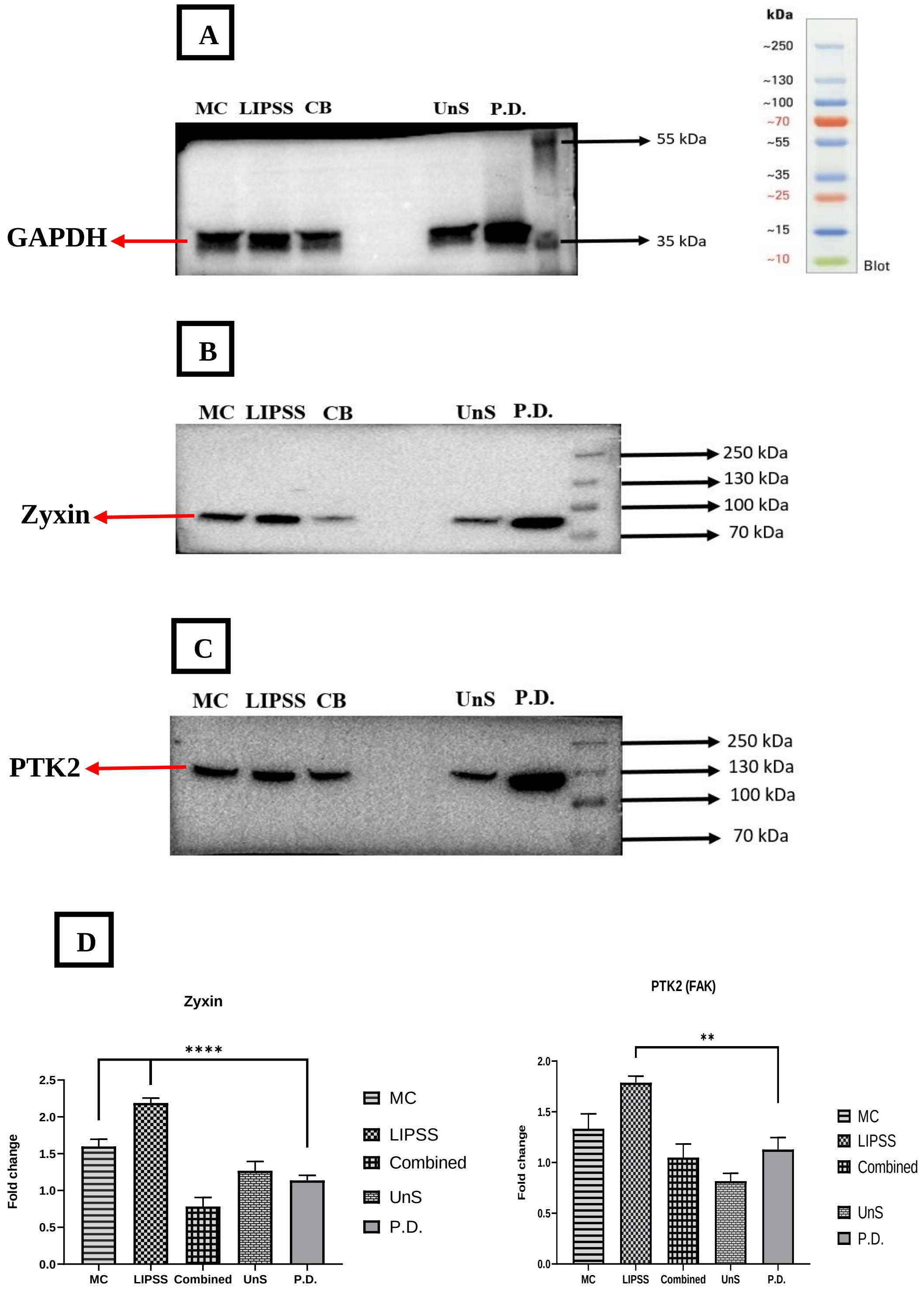

Figure 3.19: *Western Blot analysis of Zyxin and PTK2 (FAK) proteins.*

(A) Representative immunoblot showed that anti-GAPDH was detected at 37 kDa and (B) anti-Zyxin was detected at 78 kDa, and (C) anti-PTK was detected at 125 kDa from four silicon substrates and a plastic dish as a control. CB: Combined (LIPSS+MC); UnS: Unstructured silicon: P.D.: plastic dish. (D) The quantification of immunoblots (n=3, technical replicates) was normalized to GAPDH.

25 µg of total protein was loaded on to 8% Acrylamide/Bis-acrylamide gel and wet-transferred to a PVDF membrane. One-way ANOVA was used to determine to significance values. A p-value of <0.05 was taken as statistically significant. Each bar indicates the mean ± SEM.

According to Western Blot results, Zyxin protein level was significantly increased on LIPSS and microcolumn topography compared to control. The changes in unstructured silicon and combined topography are not significant, although a decreasing trend in combined and an increasing trend in unstructured silicon were observed.

The protein level of PTK2 (FAK) is only significantly increased in LIPSS topography compared to the control. On microcolumn topography, an increasing trend was observed, although it is not significant. On combined topography and unstructured silicon, the change is not significant. However, a decreasing trend is observed in these two.

CHAPTER 4

DISCUSSION

Cells' ability to grow, migrate or proliferate occurs in the 3D extracellular matrix (ECM) composed of glycosaminoglycans and fibers. Since ECM has various regulation points for the cell, its integrity and composition have a crucial role in many biological processes, such as embryonic development, cell growth, survival, proliferation, and differentiation. For all these processes to occur, the biochemical and physical characteristics of ECM should be conserved. The main components of 3D ECM include a heterogeneous network of protein fibers such as fibrillary collagen in variable orientations, density, and mechanical strength. Therefore, in the body, cells encounter different micro- and nanotopographies with variable stiffness, density, protein composition, and pore size (le Digabel *et al*., 2010). For decades, scientists have been intrigued by how extracellular signals were converted into biochemical signals and how these are used to regulate different cellular processes. 19th-century anatomist Julius Wolff approached to this puzzle by explaining the ability of cells to respond to different mechanical cues by coining the term "mechanotransduction" (Mofrad, 2009).

The transmission of mechanical cues from the environment into the nucleus is called mechanotransduction, in which regulation at the gene and protein levels contributes to modulation of the adaptive cell response. Knowledge of how mechano transduction-dependent signals are regulated in the cells is important in the context of the biomaterials field for the improvement in tissue engineering, implants, and artificial organs. Since proper mechano-signaling is crucial for cell survival, proliferation, growth, and tissue development, any aberration in the mechanotransduction pathway leads to several pathologies (McNamara *et al*., 2012). Mechanotransductive signals are various from topographical cues to substrate stiffness and/or rigidity. In this present study, by a reductionist approach, topography-dependent mechanotransduction was studied.

Fabrication of 3D cell scaffolds has attracted attention in recent years because of its applications in tissue engineering and artificial organ studies. Fabrication of well-defined precise nano- and micro-topographies to mimic the natural topographies that cell counters in the body are critical for the desired applications. Although there are various techniques to fabricate different materials, all of them have drawbacks such as high cost, not being quite precise for fabrication of nano- or micro-structures, or not being applicable to all materials. Femtosecond laser fabrication comes forward among all other techniques as it allows for the creation of desired topographies at different scales, nano-, micro, and even submicrometer scales, and provides high precision.

In this study, inspired by Mingu's work (Mingu *et al.*, 2020), nano- and micro-topographies were created by using a femtosecond laser on a silicon substrate. On these silicon substrates, Neuro-2A cells were grown, and topography-induced morphological changes were studied. Based on these morphological changes, cells' responses to different topographies at the gene and protein levels were also studied. The novelty of this study comes from the fabrication of silicon substrates with a femtosecond laser, a combination of various topographies in different dimensions, and the study of both morphological and genotypical changes induced by topographies in Neuro-2A cells. The results of this study might be a guide for future studies that might lead to implant developments, artificial organs, and tissue engineering fields.

Silicon wafers obtained from ODTÜ GÜNAM were cut into two different sizes, which are 1.5 and 1 cm, for different experiments. 1.5 cm silicon substrates were used for imaging due to their larger size area as they are more convenient for imaging. 1 cm silicon substrates were used for the rest of the experiments. Femtosecond laser fabrication parameters were inspired by Mingu's work (Mingu *et al.*, 2020) with some modifications. Different sizes of LIPSS and microcolumn lines were tried (500 µm, 1 cm, and 2 cm) with different widths (500 µm, 1 mm, and 2) with different distances between the lines (20 µm, 40 µm, and 60 µm). Substrates of 1 cm size, with 1 mm width and 20 µm distance between the lines (shown in figure 2.3) were observed to be best for cell growth, therefore these parameters were chosen for further experiments.

AFM analysis of LIPSS and microcolumn substrates showed that the surface roughness of LIPSS (Ra= 69.6 nm; RMS= 92.5 nm) is higher than microcolumn (Ra=51.7 nm; RMS=65 nm), and it has more peaks and filled valleys compared to microcolumn according to skewness (LIPSS:0.796 nm; MC:0.200 nm) and kurtosis (LIPSS: 6.10 nm; MC: 3.13 nm) values (figure 3.4). According to the literature, surface roughness can be grouped into several categories: macroscopic roughness, microscopic roughness, submicron surface roughness, and nanometer roughness which have different effects on the cells. Macroscopic roughness is the one that shows little or no effect on cell adhesion because there is enough space for cells to spread and grow on them. On the other hand, nano-roughness is assumed to resemble natural tissue morphology at best, and it is considered to be the ideal roughness for cell adhesion, growth, and maturation. For instance, a study found that increasing the roughness of the material at the nanometer scale increased cell adhesion and growth in human venous endothelial cells (Cai *et al.*, 2020). Therefore, when we compare the roughness of LIPSS and MC, although they are both at the nm scale, LIPSS is far away from resembling the micron or submicron scale than MC. This might be one reason for more cell adhesion, growth, and proliferation on LIPSS than on MC. In the literature for designing of implant surface microtopography, in the context of bone implants, different modifications are made to increase surface roughness as it is found that surface roughness has an influence on the proliferation and differentiation of osteoprecursors cells into osteoblasts and bone growth (Martinez *et al*, 2020). Therefore, a moderate level of, most favorably at the nanometer scale, surface roughness is a critical factor for cell adhesion, growth, proliferation, and differentiation.

Another feature of surface topography affecting cell behavior is the presence of peaks and filled valleys on the surface of topography. In the literature, it is shown that on the surface, focal adhesion complex formation starts at the peaks when the cells make first contact at peaks. So, these peaks and filled valleys are considered to resemble the nanoroughness of ECM and contribute to cell adhesion (Stanton, 2014). In this way, topographical features might be used as a biomimetic tool for the regulation of cell behavior for desired purposes. According to the skewness (LIPSS:0.796 nm; MC:0.200 nm) and kurtosis (LIPSS: 6.10 nm; MC: 3.13 nm) values of LIPSS and MC in this present study, LIPSS has more peaks and filled valleys than MC which might lead to more cell adhesion and growth on LIPSS. On the other hand, unstructured/polished silicon has a flat surface and little and/or no roughness, no peaks and/or valleys, and cell adhesion and growth was very low. However, on these substrates, more stress fiber formation and enlargement of the cell body were observed. In addition to the influence on cell adhesion and growth, topography might influence cell alignment and elongation. According to the literature, neurons are the only cell types that have been reported to show perpendicular guidance shown in figure 4.1. This perpendicular alignment depends on groove width and depth. Both decreasing groove width and depth have been shown to increase perpendicular alignment ((Leclech & Barakat, 2021).

Results of confocal fluorescence imaging in section 3.2.1.1 show that cell alignment and elongation with the topography and cell number and proliferation were more on LIPSS topography compared to other topographies (figure 3.15 and figure 3.16). On microcolumn topography, the alignment of cells was too little, and cell number and proliferation were second lower after the unstructured/polished silicon. On the combined topography, LIPSS+MC, more cell alignment was observed than MC, but it might be because of the availability of the LIPPS topography. Finally, there is no cell alignment on the polished silicon substrate, and cell number and proliferation were the lowest on this substrate. When the cells were differentiated, the alignment of cells became more obvious, and the axons of the cells became more elongated on LIPSS and combined topography. However, on MC, little alignment of cells before differentiation is lost totally after differentiation. On the other hand, stress fiber formation and spreading of cells seem to be less after differentiation on polished silicon, and cells' axons become more elongated. We assume that the nanoscale roughness of LIPSS results in more cell adhesion, cell growth, and proliferation compared to MC topography. Because there is not enough roughness for the cell to adhere to unpolished silicon, cell adhesion, growth and proliferation were the lowest. As combined topography includes both LIPSS and MC together, a moderate level of cell alignment, growth, and proliferation can be attributed to the presence of LIPSS. More quantification about cell morphological changes in response to different topographical features can be found in Mingu's work (2020). Directional alignment of cells with the topography and gene expression changes related to this alignment has been observed in different studies in the literature. For example, a study by Newman and colleagues (2016) reported that osteogenic and myogenic expression changes were observed in the adipose-derived stem cells (ASCs) in which cell alignment with the topography was observed. Enhancement in myogenesis was observed in cells aligned with topographies compared to flat and random topographies (Newman *et al*., 2016). The underlying mechanism of how this directional alignment of cells occurs or how cells sense physical characteristics of micro- and nano-topographies, such as depth, width, and height, has remained unknown and requires further exploration.

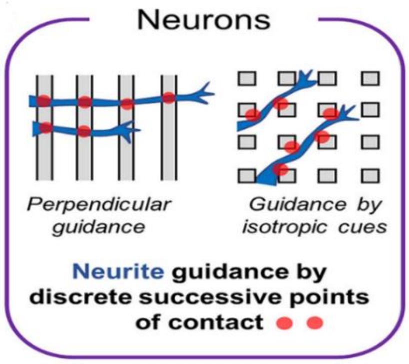

Figure 4.1: *Topography-induced cell alignment in neurons. Adapted from Leclech & Barakat, 2021*

To explore which genes might be responsible for the cell behaviors we observed in response to different topographies, we have chosen ten different focal adhesion-related genes from similar studies in the literature. Figures 4.2 and 4.3 below describe best the underlying reason for how we chose the genes for qRT-PCR analysis.

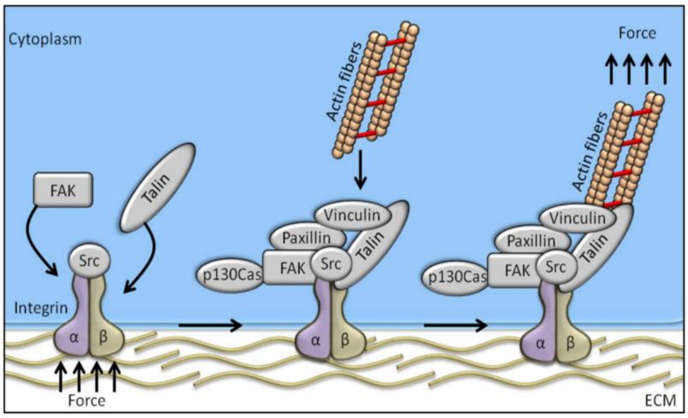

Figure 4.2: *Schematic representation of mechanotransduction pathway at the focal adhesion site.*

Through the integrin pathway, changes in ECM are sensed by the cells and as a result of integrin pathway activation, focal adhesion kinase (FAK (PTK2)) is recruited to the site. Other mechanosensing genes which are talin, vinculin, paxillin, and p130Cas are activated together and transfer the mechanical signals from integrins to the actin cytoskeleton. Adapted from Urciuoli & Peruzzi, 2020.

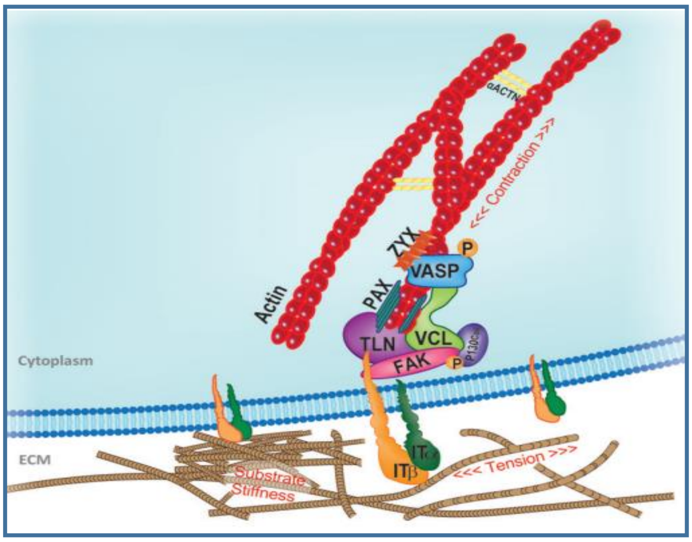

Figure 4.3: *Key mechanosensors involved in cell-ECM interaction at the focal adhesion (FA) site. Adapted from Martino et al., 2018.*

As they are in close proximity with the FA inner core, VASP, Zyxin, and actinin directly modulate the assembly and dynamics of actin. ACTN, actinin; FAK, focal adhesion kinase; IT, integrin; PAX, paxillin; TLN, talin; VASP, vasodilator-stimulated phosphoprotein; VCL, vinculin; ZYX, zyxin.

The best-known mechanosensor in the cell is the integrin family, which connects the cytoskeleton to the ECM. So, it acts as a bridge between the cellular transcriptional machinery and the external mechano-environment. Focal adhesion kinase (FAK; PTK2), which is a non-receptor tyrosine kinase localized at the focal adhesions, is the earliest and most important component of the integrin pathway to be identified. When the external stimuli are sensed by the cells, ptk2 (FAK) is the first molecule recruited to the focal adhesion site. When ptk2 (FAK) is autophosphorylated at the Tyr-397 residue, the FAK-dependent mechanotransduction signaling cascade starts. Maintaining the relationship between FAK and the cytoskeleton is crucial for living cells to sustain cellular tension homeostasis. For example, a study by Leucht and colleagues showed the importance of FAK in skeletal mechanotransduction. In the study, FAK deletion resulted in the abolishment of cellular response to mechanical stimuli, no upregulation of skeletonic genes, disorganization of collagen fibrils, and loss of mechanically-induced osteogenic response (Leucht *et al*., 2007).

The adapter protein talin act as a bridge between the cytoskeleton and membrane signals by involving in connecting the intracellular domain of β-integrin to the F-actin. There are two types of talin, talin1, which is responsible for the modulation of focal adhesion dynamics, and talin2, whose role has not been clear; however, it is assumed o function redundantly with talin1 (Qi *et al*.; 2016). Talin has several binding sites for vinculin, integrin, and actin. Vinculin binding to talin requires its activation. In turn, when vinculin binds to activated talin, this binding recruits paxillin to bind to activated vinculin. All these FAK-dependent signaling cascades start when a mechanical stimulus is sensed by the cells. It is shown that there is a positive relation between FAK activation and some mechanical stimuli such as stretching, rigid substrate, etc. (Martino *et al.*, 2018).

Another candidate gene in our study is filamin A (FLNa) which has a role in crosslinking and anchoring of actin filaments to stabilize the plasma membrane and contributes to cellular cortical rigidity and sustain mechanical stability of the cells. It is shown that recruitment of FLNa to the cell cortex was observed in response to shear stress exposure. In response to shear force, at low FLNa concentrations leads to softening of F-actin networks and vice versa. Moreover, FLNa's role in tumorigenesis has proved that it has a role in cytoskeleton rearrangement, proliferation, migration, and signal transduction in tumor cells. It has been shown that cell adhesion, motility, and migration abilities of human melanoma M2 cells have defected when they have filamin A-deficiency and show softer F-actin networks compared to other melanoma cells expressing FLNa (Bergeron-Sandoval *et al.*; 2022). FLNa's role in mechanotransduction also comes from its altering capacity of talin binding and p130Cas functions in response to strain forces (Lynch & Sheetz, 2011).

Although studies about the role of lamin A/C in mechanotransduction are not as diverse as other mechanosensor genes, the studies recently showed its importance in regulating mechanical signals. Lamins, as the structural components of the nuclear lamina, have a crucial role in the determination of nuclear shape and size. Mutations in this gene lead to various diseases such as Hutchinson-Gilford progeria syndrome, dilated cardiomyopathy, and Emery-Dreifuss muscular dystrophy. Therefore, the mechanosensation properties of this gene have started to attract attention. For instance, a study by Lammerding and colleagues showed that when the mechanical strain was applied to the lamin A/C-deficient mouse embryo fibroblasts, elevated nuclear deformation, defective mechanotransduction, and impaired viability were observed. (Lammerding *et al.*, 2004).

Another study conducted by Dutta and colleagues showed the importance of mechanosensation properties of the lamin A/C gene in skeletal muscle tissue. They used smooth and patterned surfaces to mimic muscle tissue architecture. Cells with a mutation in the lamin A/C gene showed deformed nuclei with aggregates. This makes sense when the dominant role of lamin A/C in the regulation of nuclear shape is considered. When these cells were seeded onto smooth and patterned surfaces, elongation of nuclei and softening of nuclear lamina were observed on patterned surfaces with decreased height in the cells. Moreover, impaired actin polymerization and lack of stress fibers were observed in cells grown on patterned substrates. The possible reason for that might be related to the absence of recruitment of vinculin to the cell periphery, which results in the breaking of the interaction between vinculin and F-actin. The study also showed the interaction of the lamin A/C gene with other important players of mechanotransduction, FAK, that decreased expression of FAK and integrin isoforms were detected in the cells grown on the patterned substrates which show reduced cell strength for ECM and in turn fewer cells growing on the patterned surface (Dutta *et al.*; 2022).

Last but not least, fibronectin, as cell adhesion protein and ECM protein, produced by the fibronectin (Fn) gene, was shown to be modulated mechanically. According to the current model, fibronectin binding occurs through an integrin-mediated pathway (Schwartz, 2010). It is shown that cytoskeletal tension regulates fibronectin level within cell matrix fibrils and its level is shown to be upregulated in response to substrate rigidity (Vogel, 2006). In response to tension, fibronectin fibril assembly is elevated and leads to increased integrin binding sites and receptor density. These mechanisms result in increased integrin signaling, which leads to increased binding of other mechanosensitive genes (Katsumi *et al.*, 2004).

This FAK-dependent signaling cascade and its related partners in the context of cellular mechanotransduction inspire us to choose the genes in this pathway or related genes with this pathway.

We can summarize our qRT-PCR results of these genes (figure 3.18) in response to different topographies and unstructured/polished silicon below in table 4.1. A plastic dish (TC-treated cell culture dish which is made up of polystyrene) was used as a control.

Table 4.1: *Summary of qRT-PCR results of focal adhesion-related genes of cells in response to different topographies, and unstructured/polished silicon.*

Gene name	**LIPSS**	**MC**	**Combined (LIPSS+MC)**	**Unstructured/ polished silicon**
PTK2 (FAK)	Upregulated (significant)	Upregulated (significant)	Upregulated (significant)	Increasing trend (not significant)
Vinculin	Increasing trend (not significant)	Downregulated (significant)	Increasing trend (not significant)	Decreasing trend (not significant)
Paxillin	Increasing trend (not significant)	Increasing trend (not significant)	Upregulated (significant)	Increasing trend (not significant)
Filamin A (Flna)	Upregulated (significant)	Upregulated (significant)	Increasing trend (not significant)	Upregulated (significant)
Talin 2 (Tln2)	Upregulated (significant)	Upregulated (significant)	No change	Increasing trend (not significant)
Zyxin	Upregulated (significant)	Upregulated (significant)	Upregulated (significant)	Upregulated (significant)
Lamin A/C (Lmna)	Upregulated (significant)	Upregulated (significant)	Downregulated (significant)	Upregulated (significant)
Fibronectin (FN)	Decreasing trend (not significant)	Downregulated (significant)	Upregulated (significant)	Increasing trend (not significant)
Talin 1 (Tln1)	Increasing trend (not significant)	Increasing trend (not significant)	Increasing trend (not significant)	Increasing trend (not significant)
Src	Upregulated (significant)	Upregulated (significant)	Upregulated (significant)	Upregulated (significant)

According to the results, 70 percent (7/10) of the genes we chose showed upregulation and/or increasing trends in all topographies, even on unstructured/polished silicon. The genes showing no significance were not taken into consideration, and they were taken as showing a “decreasing trend and/or increasing trend” at the mRNA level. According to our results, we hypothesized that FAK (PTK2) protein was initially recruited to the focal adhesion site when the cells were exposed to LIPSS and MC topographies which have different surface physical characteristics such as roughness, presence of peaks, etc. Although FAK recruitment or upregulation in these two topographies seems similar, vinculin expression level in these two was significantly different, which might be related to talin activation. As discussed above, talin recruitment to the focal adhesion site requires FAK activation. Upon FAK activation, talin, which has several binding sites for vinculin, integrin, and actin, is recruited to focal adhesion sites. The binding of vinculin to talin recruits another mechanosensitive gene, paxillin, to the focal adhesion site. When talin1 and talin2 expression was examined, there were no significant changes in the case of talin1; however, talin2 was upregulated in both topographies, LIPSS and MC. Although the mechanosensitive role of talin1 has been known, the role of talin2 has remained unsolved. In this study, for binding to FAK, cells might use talin2, instead of talin1. The binding site of talin2 for vinculin might not be as specific as talin1, and as a result, we see vinculin downregulation in the case of MC. However, we see nonsignificant upregulation of vinculin in LIPSS, which might be related to talin2 upregulation is more prominent in LIPSS. Paxillin recruitment to the focal adhesion site requires vinculin activation. Paxillin recruitment seems to be more in LIPSS compared to MC, although both of them are nonsignificant changes. A study conducted by Kiema and colleagues found that there is a competition between FLNa and talin for binding to integrin β tails. Talin binding to integrin β tails is an important step for integrin activation and formation of the initial integrin-cytoskeletal link (Kiema *et al.*, 2006). This competition might be an underlying reason for no detectable changes in Talin 1 and significant upregulation of FLNa in all topographies in this study. The winner of the competition for binding to integrin β tails might be FLNa and as a result, there might be no room for Talin1 to bind to integrin β tails. It is shown that FAK activation is triggered by the binding of cells to fibronectin. Effects of this interaction are also implicated in the ERK signaling pathway, which has an important role in cell growth and proliferation (Schlaepfer *et al.*, 1997). In this study, fibronectin is significantly downregulated in MC topography which might be a reason for less cell adhesion, growth, and proliferation in MC samples.

One of the most upregulated genes, zyxin, coordinates with vinculin and VASP genes to regulate actin polymerization. One of these interactions was disrupted, and actin polymerization is defected and leads to less cell adhesion and growth. More cell adhesion, growth, and proliferation on LIPSS compared to MC might be related to zyxin and vinculin upregulation in LIPSS compared to MC, although zyxin is upregulated, vinculin is downregulated significantly. As discussed above, there is a positive relation between lamin A/C and FAK expression, which might explain the upregulation of lamin A/C in LIPSS and MC as FAK was upregulated in both of them. Src-mediated phosphorylation of FAK is critical for cell adhesion. In this study, when Src levels of cells from LIPSS and MC were compared, significant upregulation was observed in both of them, although changes at the mRNA in FAK do not seem compatible with Src. This can be explained with post-translational modifications (PTMs), which FAK (PTK2) protein goes through, that might play a more crucial role in cell adhesion than expression levels.

The genes upregulated and downregulated significantly were chosen for further experiments. As discussed above, FAK (PTK2) gene was the main player in FAK-dependent mechanotransduction. Its activation recruits other players to the focal adhesion site, such as talin, vinculin, and paxillin. Therefore, although mRNA expression of FAK (PTK2) does not show much significance compared to other upregulated genes, it might show changes at the protein level so we chose it for Western Blot analysis. In addition, we chose one of the most upregulated genes for protein analysis, zyxin, which has a crucial role in the FAK-dependent mechanotransduction signaling.

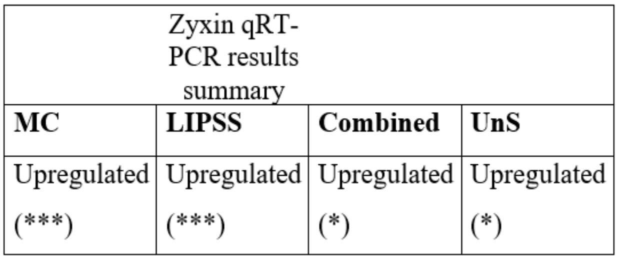

Zyxin qRT-PCR results summary			
MC	**LIPSS**	**Combined**	**UnS**
Upregulated (***)	Upregulated (***)	Upregulated (*)	Upregulated (*)

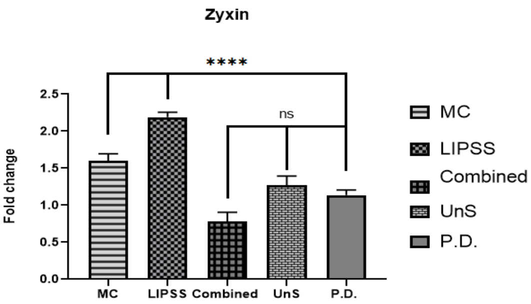

Figure 4.4: *Comparison of qRT-PCR results and densitometry analysis of Zyxin protein.*

According to Western Blot results shown in figure 3.19, both zyxin and FAK (PTK2) show a significant increase in LIPSS topography compared to the control plastic dish. Zyxin level is significantly upregulated both on microcolumn and LIPSS topography. On combined topography, a decreasing trend is observed in zyxin protein. On unstructured silicon, an increasing trend is observed in Zyxin protein. When the summary of qRT-PCR results of zyxin is compared with densitometry analysis of Western Blot bands of zyxin protein (figure 4.4), the discrepancy between mRNA expression and protein levels might be attributed to the PTMs that Zyxin goes through for the adaptive cell response in all topographies and unstructured/polished silicon. Post-translational modifications of Zyxin have never been studied in the context of mechanotransduction which requires further exploration. Another reason might be related to the changes in expression levels of the binding partner of zyxin, which are VASP and p130Cas, unfortunately, these proteins were not examined in this study. Last but not least, protein level changes were analyzed after 24 hours of cell seeding. This time duration might be enough to see mRNA changes but not enough for protein changes for all substrates.

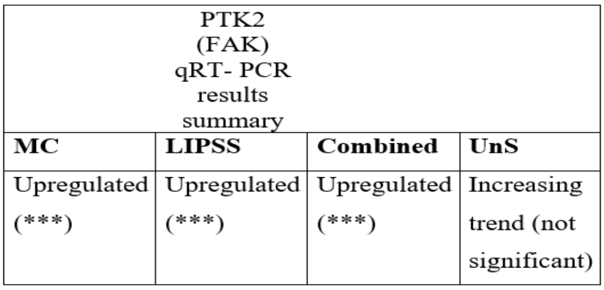

PTK2 (FAK) qRT- PCR results summary			
MC	**LIPSS**	**Combined**	**UnS**
Upregulated (***)	Upregulated (***)	Upregulated (***)	Increasing trend (not significant)

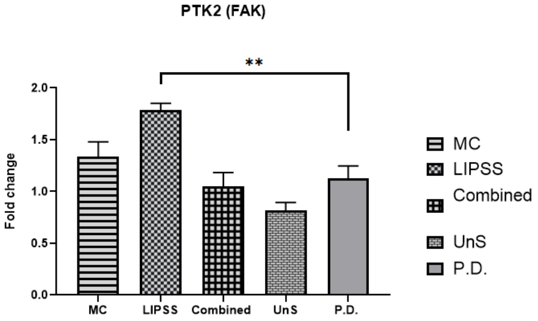

Figure 4.5: *Comparison of qRT-PCR results and densitometry analysis of PTK2 (FAK) protein.*

According to Western Blot results of FAK protein, an increased level of protein expression was observed on all three topographies except on unstructured silicon compared to the control plastic dish. However, a significant increase is observed in LIPSS. An increasing trend is observed both on microcolumn topography and unstructured silicon. Only on unstructured silicon, a decreasing trend is observed in the PTK2 protein level. When the summary of qRT-PCR results of PTK2 and densitometry analysis of Western Blot bands of PTK2 is compared (figure 4.5), the underlying reasons for the discrepancy between mRNA and protein level changes might be post-translational modifications of FAK protein whose PTMs are extensively studied in the literature. For example, autophosphorylation of FAK at tyrosine 397 (Y397) residue results in the recruitment of Src and Src-family kinases. This autophosphorylation also leads to elevated phosphorylation of other focal adhesion-related proteins such as paxillin and p130Cas. Phosphorylation-induced FAK activation does not only occurs on tyrosine but also on serine and threonine residues at multiple sites. It is reported that FAK phosphorylation at specific sites is induced by mechanical forces, and as a result of this activation, cellular physiological responses to mechanical signals are regulated (Zebda *et al*., 2012). Other than PTMs, there might be changes in the expression levels of binding partners of FAK, not only its focal adhesion-related partners or ECM protein partners, but also it might have cytoplasmic binding partners or growth factor pathway-related partners. What is suggested for zyxin might also be valid for FAK protein expression level changes we observed.

CHAPTER 5

CONCLUSIONS AND FUTURE STUDIES

Cells are constantly exposed to mechanical cues from the environment or neighboring cells. Delivery of these mechanical signals and converting them into biochemical signals, called mechanotransduction, played critical roles in various biological functions from survival, growth, and proliferation to apoptosis. Any aberration in the cells' mechanotransduction pathway leads to various diseases such as cancer. Understanding the cells’ mechanosensation machinery is important for the manipulations of cells for desired applications such as the improvement of implants. One of the non-invasive methods to elucidate the mechanotransduction pathway is to create biomimetic materials to mimic the natural nanotopographies of the extracellular matrix (ECM) of the cell. In this study, for the creation of biomimetic materials, femtosecond laser fabrication was used for the creation of nano- and micro-topographies on the silicon wafer. Silicon is known to be nontoxic to the cells. As a cell model, the Neuro2A cell line was used, and its response to different topographical patterns was assessed with different microscopic techniques and expression analysis techniques.

The study of Mingu (2020) showed that cells’ various morphological changes in response to different topographies, LIPSS and MC. Inspired by this study, we asked what genes and proteins might be responsible for these morphological changes in the cells in response to different topographies. Our primary findings have been listed below.

1. For cells to adhere to a surface, a moderate level of surface roughness is required which is shown in this study and different studies in the literature. When flat or very rough surfaces are not ideal for cell adhesion and growth. In addition to surface roughness, the presence of a moderate level of peaks on the surface of the material

is an ideal condition for cells to adhere to; however, cells do not prefer to adhere to valleys. Since cells make initial contact at the peaks, and as a result, focal adhesion complex formation begins at the peaks, which leads to the recruitment of other members of the focal adhesion complex to the site.

2. From the EDS analysis, we can conclude that morphological changes and gene and protein expression level changes observed in this study resulted from only the topographies we created using the femtosecond laser. No chemical/elemental changes were detected on the silicon surface with topographies due to fabrication.

3. In neurons, perpendicular alignment of topographical patterns has been reported. Although our confocal imaging results are not compatible with the findings, there is a parallel alignment of cells on LIPSS topography. Studies showing a parallel alignment of cells with the topography are also available in the literature which we also observed in this study.

3. Gene expression analysis by qRT-PCR showed upregulation of most of the focal adhesion-related genes we selected on all topographies and on the unstructured/polished silicon compared to the control plastic dish.

4. Western Blot analysis of two proteins, Zyxin and FAK, showed a significant increase in LIPSS compared to the control plastic dish. Also, when comparing each silicon substrate with each other, we can conclude that LIPSS topography is the ideal topography for cells to adhere, grow, and proliferate compared to others if the mRNA and protein expression levels are taken into consideration. Our results confirmed that cell growth, adhesion, and proliferation are the highest on LIPSS compared to other substrates even after 48 hours.

Several unanswered questions could be addressed in future studies:

1. In terms of substrate fabrication, surface roughness might be increased or decreased deliberately to observe how the response of the cells changes. In addition, peaks and valleys might be created on the surface, and their height and widths might be manipulated for observation of cell response to these changes.

2. As mentioned in the introduction section, most of the focal adhesion-related and ECM genes have important roles in different signaling pathways, and they have binding partners in these signaling pathways. The role of a pathway in mechanotransduction might be investigated. Furthermore, different binding partners of focal adhesion-related genes and ECM genes might be investigated, and their mRNA and protein expression level changes in response to different topographies may be further explored.

3. For screening of different genes, an RNA-seq experiment may be conducted, and Gene Set Enrichment Analysis (GSEA) might give more concrete results about the expression level changes.

4. For protein level changes, different post-translational modifications of the genes might be investigated in response to topographical changes.

5. When mechanical cues are sensed by the cells, some members of the focal adhesion complex are recruited together. To find out which of them recruited together to the focal adhesion site in the cells in response to topographical cues, a CO-IP or BioID experiment might be conducted for candidate genes.

6. Last but not least, mRNA and protein level changes may be measured at different time intervals such as 36, 48, and 72 hours. In this study, after 24 hours of cell seeding, mRNA and protein level changes are measured. However, protein level changes might take time as cells are exposed to different topographical cues.

REFERENCES

A. A. Ionin, S. I. Kudryashov, S. V. Makarov, A. A. Rudenko, L. V. Seleznev, D. V. Sinitsyn, and V. I. Emelyanov, “Nonlinear optical dynamics during femtosecond laser nanostructuring of a silicon surface,” Laser Physics Letters, vol. 12, no. 2, 2015.

AFM principle - how does an atomic force microscope work? Oxford Instruments. (n.d.). Retrieved August 1, 2022, from https://afm.oxinst.com/outreach/how-does-an-afm-microscope-work

Ahmmed, K., Grambow, C., & Kietzig, A.-M. (2014). Fabrication of micro/nano structures on metals by femtosecond laser micromachining. Micromachines, 5(4), 1219–1253. https://doi.org/10.3390/mi5041219

Ahn, M. K., Kim, T., Yoo, H. K., Song, I. C., & Gweon, D. G. (2007). Simultaneous imaging of confocal fluorescence and Raman spectrum. *Confocal, Multiphoton, and Nonlinear Microscopic Imaging III*. https://doi.org/10.1364/ecbo.2007.6630_36

Alberts, B. M., Johnson, A., & Lewis, J. (2002). Integrins. In Molecular biology of the cell (4th ed., pp. 1210–1212). essay, Garland Science.

Barnes, J. M., Przybyla, L., & Weaver, V. M. (2017). Tissue mechanics regulate brain development, homeostasis and disease. *Journal of Cell Science*, *130*(1), 71–82. https://doi.org/10.1242/jcs.191742

Belaud, V., Petithory, T., Ponche, A., Mauclair, C., Donnet, C., Pieuchot, L., Benayoun, S., & Anselme, K. (2018). Influence of multiscale and curved structures on the migration of Stem Cells. *Biointerphases*, *13*(6). https://doi.org/10.1116/1.5042747

Bergeron-Sandoval, L. P., Cai, A., Clouvel, A., Hitti, C., & Ehrlicher, A. (2022). GTPase-dependent Mechanointegration of shear-mediated cell contractility through dynamic binding of FLNA and FilGAP. *Frontiers in Physics*, *10*. https://doi.org/10.3389/fphy.2022.890865

Bonse, S. Baudach, J. Kruger, W. Kautek, and M. Lenzner, “Femtosecond laser ablation of silicon–modification thresholds and morphology,” Applied Physics A, vol. 74, no. 1, pp. 19–25, 2014.

Bonse, S. Baudach, J. Kruger, W. Kautek, and M. Lenzner, “Femtosecond laser ablation of silicon–modification thresholds and morphology,” Applied Physics A, vol. 74, no. 1, pp. 19–25, 2014.

Burridge, K., Monaghan-Benson, E., & Graham, D. M. (2019). Mechanotransduction: From the cell surface to the nucleus via rhoa. *Philosophical Transactions of the Royal Society B: Biological Sciences*, *374*(1779), 20180229. https://doi.org/10.1098/rstb.2018.0229

Cai, S., Wu, C., Yang, W., Liang, W., Yu, H., & Liu, L. (2020). Recent advance in surface modification for regulating cell adhesion and behaviors. *Nanotechnology Reviews*, *9*(1), 971–989. https://doi.org/10.1515/ntrev-2020-0076

Chang, Y.-C., Wu, J.-W., Wang, C.-W., & Jang, A. C.-C. (2020). Hippo signaling-mediated mechanotransduction in cell movement and cancer metastasis. *Frontiers in Molecular Biosciences*, *6*. https://doi.org/10.3389/fmolb.2019.00157

Chighizola, M., Dini, T., Lenardi, C., Milani, P., Podestà, A., & Schulte, C. (2019). Mechanotransduction in neuronal cell development and functioning. Biophysical Reviews, 11(5), 701–720. https://doi.org/10.1007/s12551-019-00587-2

Chiquet, M., Gelman, L., Lutz, R., & Maier, S. (2009). From mechanotransduction to extracellular matrix gene expression in fibroblasts. Biochimica Et Biophysica Acta (BBA) - Molecular Cell Research, 1793(5), 911–920. https://doi.org/10.1016/j.bbamcr.2009.01.012

Cunha, A., Zouani, O. F., Plawinski, L., Botelho do Rego, A. M., Almeida, A., Vilar, R., & Durrieu, M.-C. (2015). Human mesenchymal stem cell behavior on femtosecond laser-textured ti-6al-4v surfaces. *Nanomedicine*, *10*(5), 725–739. https://doi.org/10.2217/nnm.15.19

Densham, R. M., O'Neill, E., Munro, J., Konig, I., Anderson, K., Kolch, W., *et al.* (2009). MST kinases monitor actin cytoskeletal integrity and signal via c-Jun N-terminal kinase stress-activated kinase to regulate p21Waf1/Cip1 stability. Mol. Cell. Biol. 29, 6380–6390. doi: 10.1128/MCB.00116-09

Du, L., Wang, J., Chen, W., Zhu, P., Tian, Y., Kong, S., & Wu, C. (2022). Comparative investigation of neuronal development on nano- and micro-topographic continuous silicon substrates. Materials Letters, 316, 132017. https://doi.org/10.1016/j.matlet.2022.132017

Dupont, S., Morsut, L., Aragona, M., Enzo, E., Giulitti, S., Cordenonsi, M., Zanconato, F., Le Digabel, J., Forcato, M., Bicciato, S., Elvassore, N., & Piccolo, S. (2011). Role of yap/taz in mechanotransduction. *Nature*, *474*(7350), 179–183. https://doi.org/10.1038/nature10137

Dutta, S., Muraganadan, T., & Vasudevan, M. (2022). Evaluation of lamin A/C mechanotransduction under different surface topography in LMNA related muscular dystrophy. https://doi.org/10.1101/2022.01.03.474777

El Sabeh, M., Saha, S. K., Afrin, S., Islam, M. S., & Borahay, M. A. (2021). Wnt/β-catenin signaling pathway in uterine leiomyoma: Role in tumor biology and targeting opportunities. *Molecular and Cellular Biochemistry*, *476*(9), 3513–3536. https://doi.org/10.1007/s11010-021-04174-6

Elliott, A. D. (2019). Confocal Microscopy: Principles and modern practices. *Current Protocols in Cytometry*, *92*(1). https://doi.org/10.1002/cpcy.68

Ezzahmouly, M., Elmoutaouakkil, A., Ed-Dhahraouy, M., Khallok, H., Elouahli, A., Mazurier, A., ElAlbani, A., & Hatim, Z. (2019). Micro-computed tomographic and SEM study of porous bioceramics using an adaptive method based on the mathematical morphological operations. *Heliyon*, *5*(12). https://doi.org/10.1016/j.heliyon.2019.e02557

Fernandez, B. G., Gaspar, P., Bras-Pereira, C., Jezowska, B., Rebelo, S. R., and Janody, F. (2011). Actin-capping protein and the Hippo pathway regulate F-actin and tissue growth in Drosophila. Development 138, 2337–2346. doi: 10.1242/dev.063545

Fernández-Castillejo, S., Formentín, P., Catalán, Ú., Pallarès, J., Marsal, L. F., & Solà, R. (2017). Silicon microgrooves for contact guidance of human aortic endothelial cells. Beilstein Journal of Nanotechnology, 8, 675–681. https://doi.org/10.3762/bjnano.8.72

Fletcher, D. A., & Mullins, R. D. (2010). Cell Mechanics and the cytoskeleton. *Nature*, *463*(7280), 485–492. https://doi.org/10.1038/nature08908

Formentín, P., Alba, M., Catalán, Ú., Fernández-Castillejo, S., Pallarès, J., Solà, R., & Marsal, L. F. (2014). Effects of macro- versus nanoporous silicon substrates on human aortic endothelial cell behavior. *Nanoscale Research Letters*, *9*(1). https://doi.org/10.1186/1556-276x-9-421

Galli, C., Passeri, G., Ravanetti, F., Elezi, E., Pedrazzoni, M., & Macaluso, G. M. (2010). Rough surface topography enhances the activation of Wnt/β-catenin signaling in mesenchymal cells. *Journal of Biomedical Materials Research Part A*, *95A*(3), 682–690. https://doi.org/10.1002/jbm.a.32887

Gentile, F., Tirinato, L., Battista, E., Causa, F., Liberale, C., di Fabrizio, E. M., & Decuzzi, P. (2010). Cells preferentially grow on rough substrates. *Biomaterials*,*31*(28),7205–7212. https://doi.org/10.1016/j.biomaterials.2010.06.016

Goldmann, W. H. (2012). Mechanotransduction and focal adhesions. Cell Biology International, 36(7), 649–652. https://doi.org/10.1042/cbi20120184

Goldstein, J.I. *et al.* (1992). Coating and Conductivity Techniques for SEM and Microanalysis. In: Scanning Electron Microscopy and X-Ray Microanalysis. Springer, Boston, MA. https://doi.org/10.1007/978-1-4613-0491-3_13

Guo, B., Sun, J., Hua, Y., Zhan, N., Jia, J., & Chu, K. (2020). Femtosecond laser micro/nano-manufacturing: Theories, measurements, methods, and applications. Nanomanufacturing and Metrology, 3(1), 26–67. https://doi.org/10.1007/s41871-020-00056-5

He, S., & Ji, B. (2016). Mechanics of cell mechanosensing in protrusion and retraction of lamellipodium. *ACS Biomaterials Science & Engineering*, *3*(11), 2943–2953. https://doi.org/10.1021/acsbiomaterials.6b00539

Heckman, C. A., & Plummer, H. K. (2013). Filopodia as sensors. *Cellular Signalling*, *25*(11), 2298–2311. https://doi.org/10.1016/j.cellsig.2013.07.006

Hohmann, & Dehghani. (2019). The cytoskeleton—a complex interacting meshwork. *Cells*, *8*(4), 362. https://doi.org/10.3390/cells8040362

Humphrey, J. D., Dufresne, E. R., & Schwartz, M. A. (2014). Mechanotransduction and extracellular matrix homeostasis. Nature Reviews Molecular Cell Biology, 15(12), 802–812. https://doi.org/10.1038/nrm3896

Huynh, T. T., & Semmar, N. (2014). Dependence of ablation threshold and LIPSS formation on copper thin films by accumulative UV picosecond laser shots. *Applied Physics A*, *116*(3), 1429–1435. https://doi.org/10.1007/s00339-014-8255-0

I. Gnilitskyi, T. J. Y. Derrien, Y. Levy, N. M. Bulgakova, T. Mocek, and L. Orazi, “High-speed manufacturing of highly regular femtosecond laser-induced periodic surface structures: physical origin of regularity,” Scientific Reports, vol. 7, no. 1, p. 8485, 2017.

I. Pavlov, O. Yavuz, G. Makey, O. Toke, and O. Ilday, “Switching between normal and anomalous Laser Induced Periodic Surface Structures,” 2017.

J. Bonse, A. Rosenfeld, and J. Krüger, “On the role of surface plasmon polaritons in the formation of laser-induced periodic surface structures upon irradiation of silicon by femtosecond-laser pulses,” Journal of Applied Physics, vol. 106, no. 10, 2009.

J. Bonse, S. Hohm, S. V. Kirner, A. Rosenfeld, and J. Kruger, “Laser-Induced Periodic Surface Structures— A Scientific Evergreen,” IEEE Journal of Selected Topics in Quantum Electronics, vol. 23, no. 3, 2017.

Jansen, K. A., Atherton, P., & Ballestrem, C. (2017). Mechanotransduction at the cell-matrix interface. *Seminars in Cell & Developmental Biology*, *71*, 75–83. https://doi.org/10.1016/j.semcdb.2017.07.027

Jorge-Mora, A., Imaz, N., Garcia-Lecina, E., O'Connor, G. M., Gómez-Vaamonde, R., Alonso-Pérez, A., Franco-Trepat, E., García-Santiago, C., Pino-Minguez, J., & Nieto, D. (2018). In vitro response of bone marrow mesenchymal stem cells (hbmscs) on laser-induced periodic surface structures for hard tissue replacement: Comparison between tantalum and Titanium. *Optics and Lasers in Engineering*, *111*, 34–41. https://doi.org/10.1016/j.optlaseng.2018.07.008

Kanchanawong, P., Shtengel, G., Pasapera, A. M., Ramko, E. B., Davidson, M. W., Hess, H. F., & Waterman, C. M. (2010). Nanoscale Architecture of integrin-based cell adhesions. Nature, 468(7323), 580–584. https://doi.org/10.1038/nature09621

Karoglu, E. T., Halim, D. O., Erkaya, B., Altaytas, F., Arslan-Ergul, A., Konu, O., & Adams, M. M. (2017). Aging alters the molecular dynamics of synapses in a sexually dimorphic pattern in zebrafish (Danio rerio). Neurobiology of Aging, 54, 10–21

Katsumi, A., Orr, A. W., Tzima, E., & Schwartz, M. A. (2004). Integrins in Mechanotransduction. *Journal of Biological Chemistry*, *279*(13), 12001–12004. https://doi.org/10.1074/jbc.r300038200

Keilmann and Y. H. Bai, "Periodic surface structures frozen into CO2 lasermelted quartz," Applied Physics A, vol. 29, no. 1, pp. 9–18, 1982

Kelly, A., Farid, N., Krukiewicz, K., Belisle, N., Groarke, J., Waters, E. M., Trotier, A., Laffir, F., Kilcoyne, M., O'Connor, G. M., & Biggs, M. J. (2020). Laser-induced periodic surface structure enhances neuroelectrode charge transfer capabilities and modulates astrocyte function. *ACS Biomaterials Science & Engineering*,*6*(3),1449–1461. https://doi.org/10.1021/acsbiomaterials.9b01321

Kiema, T., Lad, Y., Jiang, P., Oxley, C. L., Baldassarre, M., Wegener, K. L., Campbell, I. D., Ylänne, J., & Calderwood, D. A. (2006). The molecular basis of filamin binding to integrins and competition with Talin. *Molecular Cell*, *21*(3), 337–347. https://doi.org/10.1016/j.molcel.2006.01.011

Kruit, P. (2010). *Introduction to charged Particle Optics: Ap 3401*. TU Delft.

Kuo, J.-C. (2014). Focal adhesions function as a mechanosensor. Progress in Molecular Biology and Translational Science, 55–73. https://doi.org/10.1016/b978-0-12-394624-9.00003-8

Kuo, Y.-C., Chang, T.-H., Hsu, W.-T., Zhou, J., Lee, H.-H., Hui-Chun Ho, J., Chien, S., & Kuang-Sheng, O. (2015). Oscillatory shear stress mediates directional reorganization of actin cytoskeleton and alters differentiation propensity of mesenchymal stem cells. *Stem Cells*, *33*(2), 429–442. https://doi.org/10.1002/stem.1860

Lammerding, J., Schulze, P. C., Takahashi, T., Kozlov, S., Sullivan, T., Kamm, R. D., Stewart, C. L., & Lee, R. T. (2004). Lamin A/C deficiency causes defective nuclear mechanics and Mechanotransduction. *Journal of Clinical Investigation*, *113*(3), 370–378. https://doi.org/10.1172/jci200419670

le Digabel, J., Ghibaudo, M., Trichet, L., Richert, A., & Ladoux, B. (2010). Microfabricated substrates as a tool to study cell mechanotransduction. *Medical & Biological Engineering & Computing*, *48*(10), 965–976. https://doi.org/10.1007/s11517-010-0619-9

Leclech, C., & Barakat, A. I. (2021). Is there a universal mechanism of cell alignment in response to substrate topography? *Cytoskeleton*, *78*(6), 284–292. https://doi.org/10.1002/cm.21661

Lee, M. R., Kwon, K. W., Jung, H., Kim, H. N., Suh, K. Y., Kim, K., & Kim, K.-S. (2010). Direct differentiation of human embryonic stem cells into selective neurons on nanoscale ridge/groove pattern arrays. Biomaterials, 31(15), 4360–4366. https://doi.org/10.1016/j.biomaterials.2010.02.012

Lefever S et al. (2009). RDML: Structured language and reporting guidelines for real-time quantitative PCR data. Nucleic Acids Res 37, 2065–2069.

Leucht, P., Kim, J.-B., Currey, J. A., Brunski, J., & Helms, J. A. (2007). Fak-mediated mechanotransduction in skeletal regeneration. *PLoS ONE*, *2*(4). https://doi.org/10.1371/journal.pone.0000390

Li, R., Beebe, T., Jen, N., Yu, F., Takabe, W., Harrison, M., Cao, H., Lee, J., Yang, H., Han, P., Wang, K., Shimizu, H., Chen, J., Lien, C.-L., Chi, N. C., & Hsiai, T. K. (2014). Shear stress–activated Wnt-angiopoietin-2 signaling recapitulates vascular repair in zebrafish embryos. *Arteriosclerosis, Thrombosis, and Vascular Biology*, *34*(10), 2268–2275. https://doi.org/10.1161/atvbaha.114.303345

Li, Y., Wang, J., & Zhong, W. (2021). Regulation and mechanism of yap/taz in the mechanical microenvironment of Stem Cells (review). *Molecular Medicine Reports*, *24*(1). https://doi.org/10.3892/mmr.2021.12145

Lin, H.-H., Ng, K.-F., Chen, T.-C., & Tseng, W.-Y. (2022). Ligands and beyond: Mechanosensitive adhesion gpcrs. *Pharmaceuticals*, *15*(2), 219. https://doi.org/10.3390/ph15020219

Liu, L., Li, X., & Nonaka, K. (2015). Light depolarization in off-specular reflection on submicro rough metal surfaces with imperfectly random roughness. *Review of Scientific Instruments*, *86*(2), 023107. https://doi.org/10.1063/1.4908172

Liu, Q., Wang, W., Zhang, L., Zhao, L., Song, W., Duan, X., & Zhang, Y. (2014). Involvement of N-cadherin/β-catenin interaction in the micro/nanotopography induced indirect mechanotransduction. Biomaterials,35(24),6206–6218. https://doi.org/10.1016/j.biomaterials.2014.04.068

Lynch, C. D., & Sheetz, M. P. (2011). Cellular mechanotransduction: Filamin a strains to regulate motility. *Current Biology*, *21*(22). https://doi.org/10.1016/j.cub.2011.10.020

M. van Driel, J. E. Sipe, and J. F. Young, “Laser-Induced Periodic Surface Structure on Solids: A Universal Phenomenon,” Physical Review Letters, vol. 49, no. 26, pp. 1955–1958, 1982.

Majhy, B., Priyadarshini, P., & Sen, A. K. (2021). Effect of surface energy and roughness on cell adhesion and growth – facile surface modification for enhanced cell culture. *RSC Advances*, *11*(25), 15467–15476. https://doi.org/10.1039/d1ra02402g

Marrese, M., Guarino, V., & Ambrosio, L. (2017). Atomic Force Microscopy: A powerful tool to address scaffold design in tissue engineering. *Journal of Functional Biomaterials*, *8*(1), 7. https://doi.org/10.3390/jfb8010007

Martinez, M. A., Balderrama, Í. de, Karam, P. S., de Oliveira, R. C., de Oliveira, F. A., Grandini, C. R., Vicente, F. B., Stavropoulos, A., Zangrando, M. S., & Sant’Ana, A. C. (2020). Surface roughness of titanium disks influences the adhesion, proliferation and differentiation of osteogenic properties derived from human. *International Journal of Implant Dentistry*, *6*(1). https://doi.org/10.1186/s40729-020-00243-5

Martínez-Calderon, M., Manso-Silván, M., Rodríguez, A., Gómez-Aranzadi, M., García-Ruiz, J. P., Olaizola, S. M., & Martín-Palma, R. J. (2016). Surface micro- and nano-texturing of stainless steel by femtosecond laser for the control of cell migration. *Scientific Reports*, *6*(1). https://doi.org/10.1038/srep36296

Martínez-Calderon, M., Manso-Silván, M., Rodríguez, A., Gómez-Aranzadi, M., García-Ruiz, J. P., Olaizola, S. M., & Martín-Palma, R. J. (2016). Surface micro- and nano-texturing of stainless steel by femtosecond laser for the control of cell migration. *Scientific Reports*, *6*(1). https://doi.org/10.1038/srep36296

Martino, F., Perestrelo, A. R., Vinarský, V., Pagliari, S., & Forte, G. (2018). Cellular mechanotransduction: From tension to function. *Frontiers in Physiology*, *9*. https://doi.org/10.3389/fphys.2018.00824

McMurray, R. J., Dalby, M. J., & Tsimbouri, P. M. (2014). Using biomaterials to study stem cell mechanotransduction, growth and differentiation. Journal of Tissue Engineering and Regenerative Medicine, 9(5), 528–539. https://doi.org/10.1002/term.1957

McNamara, L. E., Burchmore, R., Riehle, M. O., Herzyk, P., Biggs, M. J. P., Wilkinson, C. D. W., Curtis, A. S. G., & Dalby, M. J. (2012). The role of microtopography in cellular mechanotransduction. *Biomaterials*, *33*(10), 2835–2847. https://doi.org/10.1016/j.biomaterials.2011.11.047

Mingu, S. (2020). Behavior Of Neuro-2A Cells On Femtosecond Laser Structured Silicon Substrates (thesis). Ankara.

Mingu, S., Pavlov, I., Son, Ç., & Bek, A. (2020). The behaviour of neuro-2a cells on silicon substrates with various topographies generated by femtosecond laser micromachining. *Proceedings of the 13th International Joint Conference on Biomedical Engineering Systems and Technologies*. https://doi.org/10.5220/0009160001920199

Mofrad. (2009). *Cellular mechanotransduction: Diverse perspectives from molecules to tissues*. Cambridge University Press.

Mokobi, F., & Ritesh. (2022, May 26). *Scanning electron microscope (SEM)-definition, principle, parts, images*. Microbe Notes. Retrieved July 31, 2022, from Kruit, P. (2010). Introduction to charged Particle Optics: Ap 3401. TU Delft.

Morgan, J. T., Murphy, C. J., & Russell, P. (2013). What do mechanotransduction, Hippo, Wnt, and TGFB have in common? YAP and TAZ as key orchestrating molecules in ocular health and disease. *Experimental Eye Research*, *115*, 1–12. https://doi.org/10.1016/j.exer.2013.06.012

Nasrollahzadeh, M. N., Atarod, M., Sajjadi, M., Sajadi, M. S., & Issaabadi, Z. (2019). Plant-Mediated Green Synthesis of Nanostructures: Mechanisms, Characterization, and Applications. In *An introduction to green nanotechnology* (Vol. 28, p. 261). essay, Academic Press.

Newman, P., Galenano-Niño, J., Graney, P. *et al.* Relationship between nanotopographical alignment and stem cell fate with live imaging and shape analysis. *Sci Rep* **6,** 37909 (2016). https://doi.org/10.1038/srep37909

Nikkhah, M., Edalat, F., Manoucheri, S., & Khademhosseini, A. (2012). Engineering microscale topographies to control the cell–substrate interface. Biomaterials, 33(21), 5230–5246. https://doi.org/10.1016/j.biomaterials.2012.03.079

Norman, J. J., & Desai, T. A. (2006). Methods for fabrication of nanoscale topography for tissue engineering scaffolds. Annals of Biomedical Engineering, 34(1), 89–101. https://doi.org/10.1007/s10439-005-9005-4

Oakley C, Brunette DM. The sequence of alignment of microtubules, focal contacts and actinfilaments in fibroblasts spreading on smooth and grooved titanium substrata. J Cell Sci. 1993; 106:343–54. [PubMed: 8270636]

Oakley C, Jaeger NAF, Brunette DM. Sensitivity of fibroblasts and their cytoskeletons to substratum topographies: topographic guidance and topographic compensation by micromachined grooves of different dimensions. Exp Cell Res. 1997; 234:413–24. [PubMed: 9260912]

Ohashi, K., Fujiwara, S., & Mizuno, K. (2017). Roles of the cytoskeleton, cell adhesion and Rho signalling in mechanosensing and mechanotransduction. *Journal of Biochemistry*. https://doi.org/10.1093/jb/mvw082

Ohashi, K., Fujiwara, S., & Mizuno, K. (2017). Roles of the cytoskeleton, cell adhesion and Rho signalling in mechanosensing and mechanotransduction. *Journal of Biochemistry*. https://doi.org/10.1093/jb/mvw082

Ohashi, K., Fujiwara, S., & Mizuno, K. (2017). Roles of the cytoskeleton, cell adhesion and Rho signalling in mechanosensing and mechanotransduction. *Journal of Biochemistry*. https://doi.org/10.1093/jb/mvw082

Öktem, B., Pavlov, I., Ilday, S., Kalaycıoğlu, H., Rybak, A., Yavaş, S., Erdoğan, M., & Ilday, F. Ö. (2013). Nonlinear laser lithography for indefinitely large-area nanostructuring with femtosecond pulses. *Nature Photonics*, *7*(11), 897–901. https://doi.org/10.1038/nphoton.2013.272

Paddock, S. W. (2000). Principles and practices of laser scanning confocal microscopy. *Molecular Biotechnology*, *16*(2), 127–150. https://doi.org/10.1385/mb:16:2:127

Petrović, S., Peruško, D., Skoulas, E., Kovač, J., Mitrić, M., Potočnik, J., Rakočević, Z., & Stratakis, E. (2019). Laser-assisted surface texturing of ti/zr multilayers for Mesenchymal Stem Cell response. *Coatings*, *9*(12), 854. https://doi.org/10.3390/coatings9120854

Pfaffl, M. W. (2001). A new mathematical model for relative quantification in realtime RT-PCR. Nucleic Acids Research, 29(9), e45. https://doi.org/10.1093/nar/29.9.e45

Pirozzi, N. M., Kuipers, J., & Giepmans, B. N. G. (2021). Sample preparation for energy dispersive X-ray imaging of biological tissues. *Methods in Cell Biology*, 89–114. https://doi.org/10.1016/bs.mcb.2020.10.023

Qi, L., Jafari, N., Li, X., Chen, Z., Li, L., Hytönen, V. P., Goult, B. T., Zhan, C.-G., & Huang, C. (2016). Talin2-mediated traction force drives matrix degradation and cell invasion. *Journal of Cell Science*, *129*(19), 3661–3674. https://doi.org/10.1242/jcs.185959

Reimer, L. (1998). *Scanning electron microscopy: Physics of image formation and microanalysis*. Springer.

Rys, J. P., Monteiro, D. A., & Alliston, T. (2016). Mechanobiology of TGFB signaling in the Skeleton. *Matrix Biology*, *52-54*, 413–425. https://doi.org/10.1016/j.matbio.2016.02.002

Sansores-Garcia, L., Bossuyt, W., Wada, K., Yonemura, S., Tao, C., Sasaki, H., *et al.* (2011). Modulating F-actin organization induces organ growth by affecting the Hippo pathway. EMBO J. 30, 2325–2335. doi: 10.1038/emboj.2011.157

Schlaepfer, D. D., Broome, M. A., & Hunter, T. (1997). Fibronectin-stimulated signaling from a focal adhesion kinase-c-SRC complex: Involvement of the grb2, p130cas, and NCK adaptor proteins. *Molecular and Cellular Biology*, *17*(3), 1702–1713. https://doi.org/10.1128/mcb.17.3.1702

Scholz, N. (2018). Cancer cell mechanics: Adhesion G protein-coupled receptors in action? *Frontiers in Oncology*, *8*. https://doi.org/10.3389/fonc.2018.00059

Schwartz, M. A. (2010). Integrins and extracellular matrix in Mechanotransduction. Cold Spring Harbor Perspectives in Biology, 2(12). https://doi.org/10.1101/cshperspect.a005066

Schwartz, M. A. (2010). Integrins and extracellular matrix in Mechanotransduction. *Cold Spring Harbor Perspectives in Biology*, *2*(12). https://doi.org/10.1101/cshperspect.a005066

Stanton, M. M. (2014). *Regulation of cell behavior at the cell-surface interface* (dissertation). Worcester Polytechnic Institute, Worcester, MA.

Stassen, O. M., Ristori, T., & Sahlgren, C. M. (2020). Notch in mechanotransduction – from molecular mechanosensitivity to tissue mechanostasis. *Journal of Cell Science*, *133*(24). https://doi.org/10.1242/jcs.250738

Stukel, J. M., & Willits, R. K. (2016). Mechanotransduction of neural cells through cell–substrate interactions. Tissue Engineering Part B: Reviews, 22(3), 173–182. https://doi.org/10.1089/ten.teb.2015.0380

Sundaram, S. K., & Mazur, E. (2002). Inducing and probing non-thermal transitions in semiconductors using femtosecond laser pulses. Nature Materials, 1(4), 217–224. https://doi.org/10.1038/nmat767

Takada, Y., Ye, X., & Simon, S. (2007). The integrins. Genome Biology, 8(5), 215. https://doi.org/10.1186/gb-2007-8-5-215

Teixeira, A. I., Abrams, G. A., Bertics, P. J., Murphy, C. J., & Nealey, P. F. (2003). Epithelial contact guidance on well-defined micro- and nanostructured substrates. Journal of Cell Science, 116(10), 1881–1892. https://doi.org/10.1242/jcs.00383

Tekade, R. K., Raval, N., Maheshwari, R., Kalyane, D., Youngren-Ortiz, S. R., Chougule, M. B., & Tekade, R. K. (2019). Importance of Physicochemical Characterization of Nanoparticles in Pharmaceutical Product Development. In *Basic Fundamentals of Drug Delivery* (p. 379). essay, Academic Press.

Teo, B. K., Wong, S. T., Lim, C. K., Kung, T. Y., Yap, C. H., Ramagopal, Y., Romer, L. H., & Yim, E. K. (2013). Nanotopography modulates mechanotransduction of stem cells and induces differentiation through focal adhesion kinase. ACS Nano, 7(6), 4785–4798. https://doi.org/10.1021/nn304966z

Totaro, A., Castellan, M., Battilana, G., Zanconato, F., Azzolin, L., Giulitti, S., Cordenonsi, M., & Piccolo, S. (2017). Yap/taz link cell mechanics to notch signalling to control epidermal stem cell fate. *Nature Communications*, *8*(1). https://doi.org/10.1038/ncomms15206

Upadhyay, R. K., & Kumaraswamidhas, L. A. (2018). Bearing failure issues and corrective measures through Surface Engineering. *Handbook of Materials Failure Analysis*, 209–233. https://doi.org/10.1016/b978-0-08-101928-3.00011-2

Urciuoli, E., & Peruzzi, B. (2020). Involvement of the FAK network in pathologies related to altered mechanotransduction. *International Journal of Molecular Sciences*, *21*(24), 9426. https://doi.org/10.3390/ijms21249426

Vandesompele J et al. (2002). Accurate normalization of real-time quantitative RT-PCR data by geometric averaging of multiple internal control genes. Genome Biol 3, research0034.1

Vermeulen, S., Roumans, N., Honig, F., Carlier, A., Hebels, D. G. A. J., Eren, A. D., Dijke, P. ten, Vasilevich, A., & de Boer, J. (2020). Mechanotransduction is a context-dependent activator of TGF-β signaling in mesenchymal stem cells. Biomaterials,259, 120331. https://doi.org/10.1016/j.biomaterials.2020.120331

Vermeulen, S., Roumans, N., Honig, F., Carlier, A., Hebels, D. G. A. J., Eren, A. D, Dijke, P. ten, Vasilevich, A., & de Boer, J. (2020). Surface topography is a context-dependent activator of TGF-β signaling in mesenchymal stem cells. https://doi.org/10.1101/2020.01.13.903195

Vogel, V. (2006). Mechanotransduction involving multimodular proteins: Converting force into biochemical signals. *Annual Review of Biophysics and BiomolecularStructure*,*35*(1),459–488. https://doi.org/10.1146/annurev.biophys.35.040405.102013

Vorobyev, A. Y., & Guo, C. (2009). Femtosecond laser surface structuring of biocompatible metals. *SPIE Proceedings*. https://doi.org/10.1117/12.809593

Vorobyev, A. Y., & Guo, C. (2012). Direct femtosecond laser surface nano/microstructuring and its applications. *Laser & Photonics Reviews*, *7*(3), 385–407. https://doi.org/10.1002/lpor.201200017

Wang, X., Ohlin, C. A., Lu, Q., & Hu, J. (2008). Cell directional migration and oriented division on three-dimensional laser-induced periodic surface structures on polystyrene. *Biomaterials*, *29*(13), 2049–2059. https://doi.org/10.1016/j.biomaterials.2007.12.047

Wilems, T., Vardhan, S., Wu, S., & Sakiyama-Elbert, S. (2019). The influence of microenvironment and extracellular matrix molecules in driving neural stem cell fate within biomaterials. Brain Research Bulletin, 148, 25–33. https://doi.org/10.1016/j.brainresbull.2019.03.004

Wozniak, M. A., & Chen, C. S. (2009). Mechanotransduction in development: A growing role for contractility. *Nature Reviews Molecular Cell Biology*, *10*(1), 34–43. https://doi.org/10.1038/nrm2592

Yada, S., & Terakawa, M. (2015). Femtosecond laser induced periodic surface structure on poly-L-lactic acid. *Optics Express*, *23*(5), 5694. https://doi.org/10.1364/oe.23.005694

Yang, K., Jung, H., Lee, H.-R., Lee, J. S., Kim, S. R., Song, K. Y., Cheong, E., Bang, J., Im, S. G., & Cho, S.-W. (2014). Multiscale, hierarchically patterned topography for directing human neural stem cells into functional neurons. ACS Nano, 8(8), 7809–7822. https://doi.org/10.1021/nn501182f

Yang, K., Jung, K., Ko, E., Kim, J., Park, K. I., Kim, J., & Cho, S.-W. (2013). Nanotopographical manipulation of focal adhesion formation for enhanced differentiation of human neural stem cells. ACS Applied Materials & Interfaces, 5(21), 10529–10540. https://doi.org/10.1021/am402156f

Yang, L., Friedland, S., Corson, N., & Xu, L. (2014). GPR56 inhibits melanoma growth by internalizing and degrading its ligand TG2. *Cancer Research*, *74*(4), 1022–1031. https://doi.org/10.1158/0008-5472.can-13-1268

Yong, Y. K., Bazaei, A., & Moheimani, S. O. (2014). Video-rate lissajous-scan atomic force microscopy. *IEEE Transactions on Nanotechnology*, *13*(1), 85–93. Marrese, M., Guarino, V., & Ambrosio, L. (2017). Atomic Force Microscopy: A powerful tool to address scaffold design in tissue engineering. Journal of Functional Biomaterials, 8(1), 7. https://doi.org/10.3390/jfb8010007

Zareidoost, A., Yousefpour, M., Ghaseme, B., & Amanzadeh, A. (2012). The relationship of surface roughness and cell response of chemical surface modification of Titanium. *Journal of Materials Science: Materials in Medicine*, *23*(6), 1479–1488. https://doi.org/10.1007/s10856-012-4611-9

Zebda, N., Dubrovskyi, O., & Birukov, K. G. (2012). Focal adhesion kinase regulation of mechanotransduction and its impact on endothelial cell functions. *MicrovascularResearch*,*83*(1),71–81. https://doi.org/10.1016/j.mvr.2011.06.007

Zhang YC, Jiang QL, Long MQ, Han RZ, Cao KQ, *et al.* Femtosecond laser-induced periodic structures: mechanisms, techniques, and applications. Opto-Electron Sci 1, 220005 (2022).

Zhang, G., & Wang, D. (2009). Colloidal lithography-the art of nanochemical patterning. Chemistry - An Asian Journal, 4(2), 236–245. https://doi.org/10.1002/asia.200800298

APPENDICES

A. EDS analysis of different topographies and unstructured/polished silicon

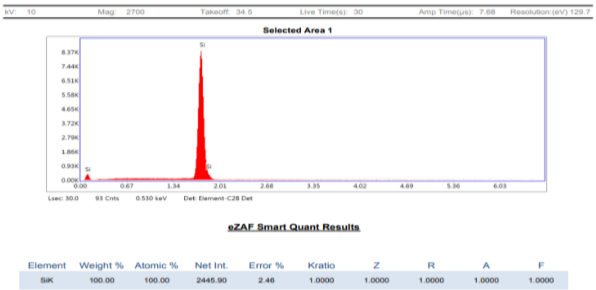

kV: 10 Mag: 2700 Takeoff: 34.5 Live Time(s): 30 Amp Time(µs): 7.68 Resolution:(eV) 129.7

Selected Area 1

Lsec: 30.0 93 Cnts 0.530 keV Det: Element-C2B Det

eZAF Smart Quant Results

Element	Weight %	Atomic %	Net Int.	Error %	Kratio	Z	R	A	F
SiK	100.00	100.00	2445.90	2.46	1.0000	1.0000	1.0000	1.0000	1.0000

Figure A. 1: *EDS analysis of unstructured/polished silicon from a different selected area*

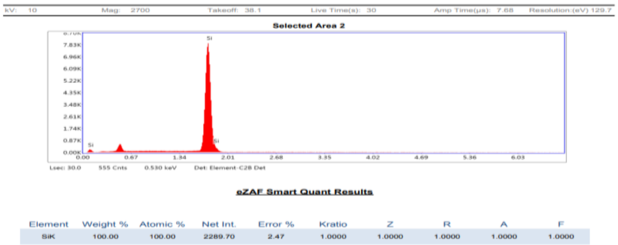

kV: 10 Mag: 2700 Takeoff: 38.1 Live Time(s): 30 Amp Time(µs): 7.68 Resolution:(eV) 129.7

Selected Area 2

Lsec: 30.0 555 Cnts 0.530 keV Det: Element-C2B Det

eZAF Smart Quant Results

Element	Weight %	Atomic %	Net Int.	Error %	Kratio	Z	R	A	F
SiK	100.00	100.00	2289.70	2.47	1.0000	1.0000	1.0000	1.0000	1.0000

Figure A. 2: *EDS analysis of LIPSS topography from a different selected area of the topography*

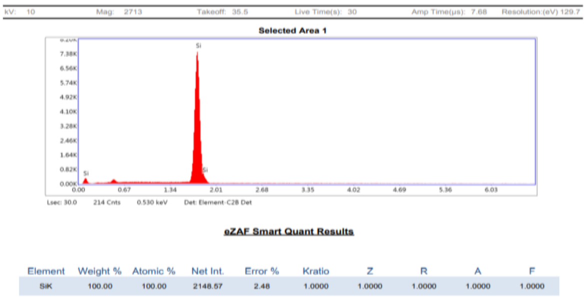

kV: 10 Mag: 2713 Takeoff: 35.5 Live Time(s): 30 Amp Time(µs): 7.68 Resolution:(eV) 129.7

Selected Area 1

Lsec: 30.0 214 Cnts 0.530 keV Det: Element-C2B Det

eZAF Smart Quant Results

Element	Weight %	Atomic %	Net Int.	Error %	Kratio	Z	R	A	F
SiK	100.00	100.00	2148.57	2.48	1.0000	1.0000	1.0000	1.0000	1.0000

Figure A. 3: *EDS analysis of microcolumn topography from a different selected area of the topography*

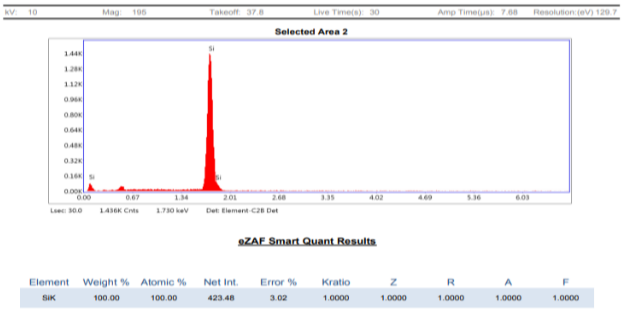

kV: 10 Mag: 195 Takeoff: 37.8 Live Time(s): 30 Amp Time(µs): 7.68 Resolution:(eV) 129.7

Selected Area 2

Lsec: 30.0 1.436K Cnts 1.730 keV Det: Element-C2B Det

eZAF Smart Quant Results

Element	Weight %	Atomic %	Net Int.	Error %	Kratio	Z	R	A	F
SiK	100.00	100.00	423.48	3.02	1.0000	1.0000	1.0000	1.0000	1.0000

Figure A. 4: *EDS analysis of Combined (LIPSS+MC) topography from a different selected area of the topography*

B. Melt curves of primers used in qRT-PCR and quantification with the Pfaffl method

Figure B.1: *qRT-PCR results and analysis of GAPDH between the control group (plastic dish) and silicon substrates*

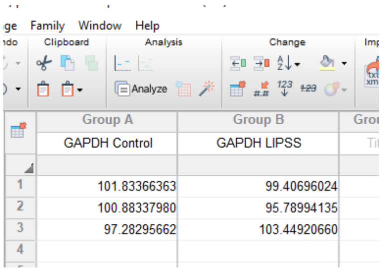

	Group A	Group B	Grou
	GAPDH Control	GAPDH LIPSS	Ti
1	101.83366363	99.40696024	
2	100.88337980	95.78994135	
3	97.28295662	103.44920660	
4			

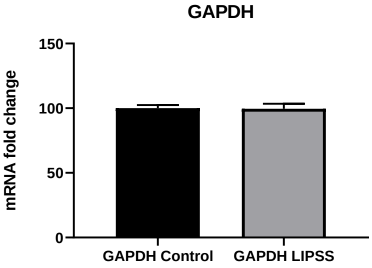

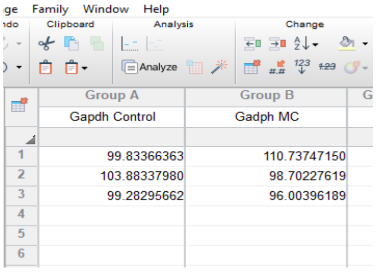

	Group A	Group B	G
	Gapdh Control	Gadph MC	
1	99.83366363	110.73747150	
2	103.88337980	98.70227619	
3	99.28295662	96.00396189	
4			
5			
6			

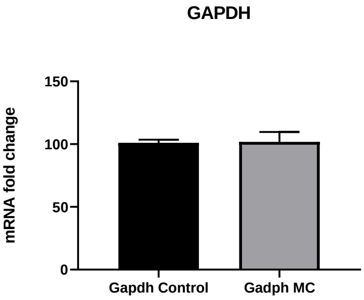

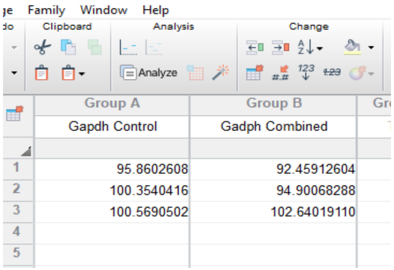

	Group A	Group B
	Gapdh Control	Gadph Combined
1	95.8602608	92.45912604
2	100.3540416	94.90068288
3	100.5690502	102.64019110
4		
5		

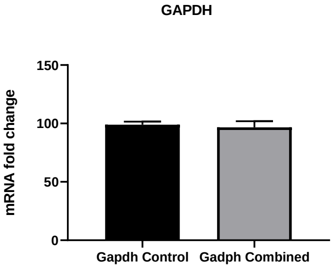

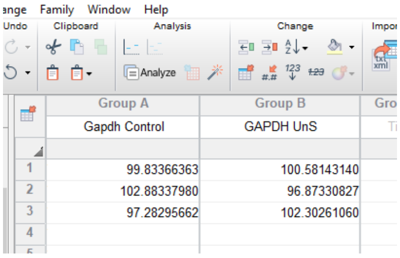

	Group A	Group B
	Gapdh Control	GAPDH UnS
1	99.83366363	100.58143140
2	102.88337980	96.87330827
3	97.28295662	102.30261060
4		

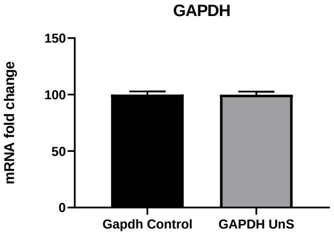

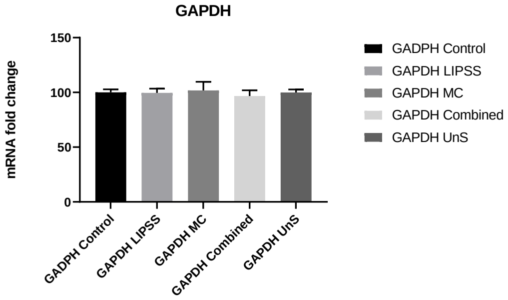

Figure B.2: *Melt curves of primers used in qRT-PCR*

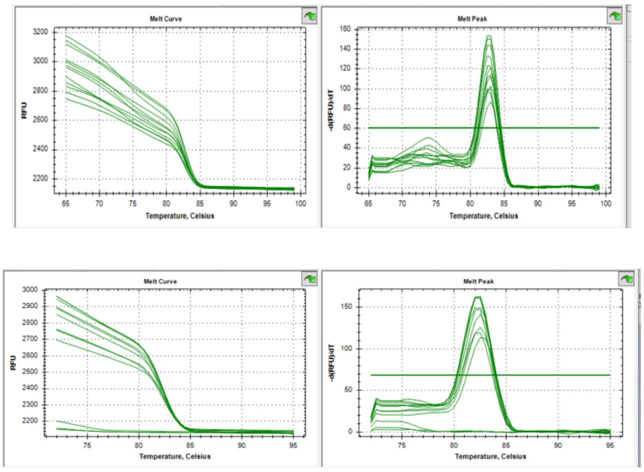

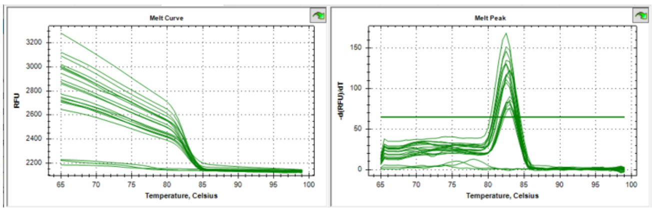

C. Composition of media and buffers used in bacterial cell culture

Table C. 1: *Composition of Lysogeny Broth (LB) Media*

Tryptone	10 g/L
NaCI	5 g/L
Yeast Extract	5 g/L

Ingredients were dissolved in distilled H2O. For LB agar plate preparation, 20 g/L was added. The pH of the solution was adjusted to 7.0.

Table C. 2: *Composition of TFBI buffer*

TFBI		
	250 mL	
30 mM potassium acetate	0.74	g
10 mM CaCI2	1.25 mL	mL of 2 M
50 mM MnCI2	2.47	g
100 mM RbCI	3.023	g
%15 glycerol	37.5	mL of % 99

Overall volume was completed to 250 mL by using distilled H2O and pH was adjusted to 5.8. The solution was filtered with a 0.45mm filter.

Table C. 3: *Composition of TFBII buffer*

TFBII	
	100 mL

10 mM MOPS or PIPES	0.335	g
75 mM CaCI2	3.75 mL	mL of 2 M
10 mM RbCI	0.12	g
%15 glycerol	15	mL of % 99

Overall volume was completed to 100mL by using distilled H2O and pH was adjusted to 6.5. The solution was filtered with a 0.45mm filter.

Table C. 4: *Phosphate buffer saline (PBS), 10X stock solution; (1L)*

NaCI	80 g
KCI	2 g
Na_2HPO_4	14.4 g
KH_2PO_4	2.4 g
TOTAL	**1 L**

The ingredients were dissolved in 800 mL of distilled water. Then pH of the solution was adjusted to 7.4 with HCI. Following, the total volume was brought to 1 L, and the solution was sterilized with autoclaving.

D. Composition of buffers and chemicals used in Western Blotting

Table D. 1: *Composition of 6X loading dye*

12 ml dH2O+ 6g SDS	12 ml SDS
2-Mercaptoethanol	15 ml
Glycerol	15 ml
Bromophenol blue	500 ul from %2
TRIS	3.75 ml
dH2O	3.75 ml

Table D. 2: *Running buffer, 10X stock solution, (1L)*

Glycine (192 mM)	144 g
Tris base (25 mM)	30.2 g
SDS (0.1%)	10 g
	Dissolve in 800 ml dH20 and complete to 1 L

Table D. 3: *Blotting (Transfer buffer), 10X stock solution, (1L)*

Tris base	30.3 g
Glycine	144 g
	Dissolve in 800 ml dH20 and complete to 1 L

Table D. 4: *Separating gel mix (%8)*

dH2O	2.7 ml
30 % Acry/Bisacryl (37.5:1)	1.76 ml
1.5 M, pH 8.8 Tris-HCI	1.7 ml
10% APS	67 ul
TEMED	6.7 ul

Table D. 5: *Stacking gel mix (%4)*

dH2O	2.1 ml
30 % Acry/Bisacryl (37.5:1)	433 ul
0.5 M, pH 6.8 Tris-HCI	833 ul
10 % APS	33.3 ul
TEMED	3.33 ul

Table D. 6: *Tris-buffered saline (TBS), 20X stock solution, (1L)*

Tris base (0.4 M)	48.4 g
NaCI	160 g
	Dissolve in 800 ml dH2O and complete to 1 L

Table D. 7: *Recipe of 1X TBS-T, (1L)*

10 % Tween-20 solution	10 ml
20X TBS	50 ml
dH2O	940 ml

Table D. 8: *Mild stripping buffer*

Glycine	15 g
SDS	1 g
Tween-20	10 ml

the pH of the buffer was adjusted to 2.2 in 1L of dH2O.